UNIVERSITEIT GENT

FACULTEIT WETENSCHAPPEN

A RELATIVISTIC EIKONAL DESCRIPTION OF NUCLEON PROPAGATION THROUGH NUCLEI

Bart Van Overmeire

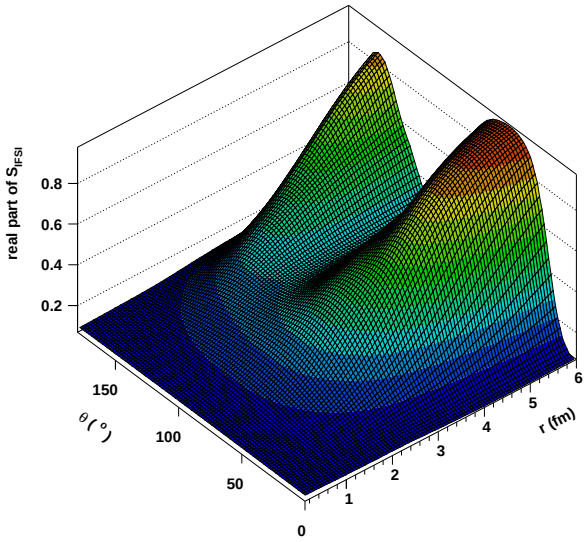

Promotor: Prof. dr. Jan Ryckebusch

Proefschrift ingediend tot het behalen van de academische graad van
Doctor in de Wetenschappen: Natuurkunde

Universiteit Gent
Faculteit Wetenschappen
Vakgroep Subatomaire en Stralingsfysica
Academiejaar 2006-2007

Voor Barbara en Jules

Contents

Chapter 1

Introduction

Ever since the discovery of the atomic nucleus by Rutherford in the early 20th century, nuclei and their constituent particles have been the subject of a great deal of scientific research. The interest in nuclear physics stems from the fact that the nucleus is a unique form of matter, consisting of many protons and neutrons in close proximity. As such, the nucleus provides a microscopic laboratory to study different forces of nature: the strong, electromagnetic, and weak interaction. Moreover, nuclear matter accounts for more than 99.9% of the mass in the visible universe. Consequently, nuclear physics plays a crucial role in the understanding of our world, from the infinitesimal to the astronomical. Finally, there are many practical applications of nuclear physics, in energy production, medical diagnosis and treatments, to name a few.

A powerful tool to extract information about nuclear structure and the properties of bound nucleons is the scattering of leptonic or hadronic probes from nuclei. The advantages of using leptons as probes arise from the fact that they interact weakly with the nucleus. This enables the leptons to probe the entire nuclear volume without significantly disturbing the target object. It also means that the electroweak interaction can be treated perturbatively. Leptonic scattering, however, has the disadvantage that the cross sections are much smaller than those for purely hadronic reactions. Thus, hadronic scattering has a large "discovery" potential, whereas leptonic reactions are used for precision experiments. Hadronic scattering is more challenging theoretically because of the strong interaction with nuclear matter. Moreover, hadronic probes mostly sample the nuclear surface.

Quasielastic Scattering and the $A(p, pN)$ Reaction

The main focus of this work will be on exclusive proton-nucleus scattering in the quasielastic region. In the scattering spectrum of a hadronic probe from the nucleus, the quasielastic region appears as a wide peak at $\omega \approx Q^2/2M_N$, with $(\omega, \vec{q})$ the energy and momentum transfer, $Q^2 = |\vec{q}|^2 - \omega^2$, and M_N the nucleon mass. One expects that in this region, the probe induces the knockout of a single nucleon. In exclusive measurements, the ejectile and the knocked-out nucleon are detected in coincidence and, hence, more detailed information about the reaction mechanism is obtained than in inclusive experiments.

To first order, quasielastic scattering can be understood as scattering from the bound nucleons, i.e., the interaction with the target nucleus is assumed to occur through the individual nucleons. This is the so-called impulse approximation (IA). Hence, a quasielastic $A(p, pN)$ reaction can be described as follows: The energy ω and momentum $\vec{q}$ transferred by the impinging proton to the nucleus are predominantly absorbed by a single bound nucleon, which is subsequently knocked out of the target nucleus. Thus, the struck nucleon is assumed to coincide with the ejected one. Since the ejectile absorbs the major fraction of the transferred energy, the residual $A - 1$ nucleus is left in its ground state or in a low-lying excited state.

Over the last five decades, quasielastic nucleon-knockout reactions have been extensively investigated. For a review of the research into proton-induced single-nucleon emission off nuclear targets, the reader is referred to Refs. [1–3]. The basic idea behind the $A(p, pN)$ models is the IA. This relatively simple reaction mechanism of one "hard" nucleon-nucleon collision is, however, obscured by the "soft" initial- and final-state interactions (IFSI) of the incident and two outgoing nucleons with the nuclear medium. A sketch of the $A(p, 2p)$ reaction is given in Fig. 1.1. Any model for $A(p, 2p)$ and $A(p, pn)$ reactions needs to address at least three issues:

- The hard scattering that leads to the ejection of the struck nucleon.
- The structure of the target and residual nucleus.
- The distorting mechanisms of the soft small-angle IFSI.

With regard to the treatment of the hard NN scattering part, essentially two methods exist. In the so-called cross-section factorized approximation [1, 4], the

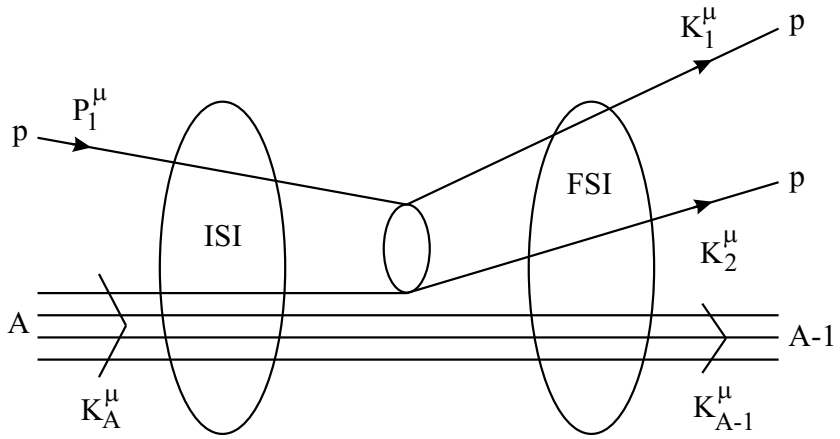

Figure 1.1 Schematic representation of the $A(p, 2p)$ reaction. The incoming proton undergoes "soft" initial-state interactions with the target before knocking out a bound proton through the primary high-momentum-transfer pp scattering. Both the scattered and the ejected proton suffer final-state interactions while leaving the nucleus. The scattered and the ejected proton are detected in coincidence, while the residual nucleus remains unobserved.

nucleon-nucleon scattering cross section enters as a multiplicative factor in the differential $A(p, pN)$ cross section. Some results of exclusive $A(p, 2p)$ measurements interpreted with this cross-section factorized form can be found in Refs. [5–10]. Inclusion of a spin dependence in the description of the IFSI, however, breaks this factorization scheme. In that situation, an alternative technique can be used: the amplitude factorized form of the cross section [11]. In this approach, the two-body NN interaction can be approximated by the interpolation of phase shifts [12, 13] from free elastic NN scattering. Various phenomenological forms to fit the amplitudes have been proposed. Traditionally, the nucleon-nucleon scattering matrix has been parametrized in terms of five Lorentz invariants [14–23], a method usually dubbed as the IA1 model or the SPVAT (scalar, pseudoscalar, vector, axial vector, tensor) form of the NN scattering matrix. Cross-section calculations adopting these five-term representations have been reported in Refs [24–32] and provide reasonable predictions of $A(p, pN)$ observables. However, such a five-term relativistic parametrization of the NN scattering matrix is inherently ambiguous [33]. Tjon and Wallace [34] have shown that a complete expansion of the NN scattering matrix (commonly called the IA2 model) contains 44 independent invariant

amplitudes. To date, the sole calculations adopting this general Lorentz invariant representation have ignored all IFSI mechanisms [35].

For the description of the target and residual nucleus, an independent-particle model (IPM) picture is customarily considered. Then, the initial- and final-state $(A+1)$-nucleon wave functions are Slater determinants composed of single-particle wave functions. These latter are solutions to a one-body Schrödinger or Dirac equation. In our approach, the relativistic bound-state single-particle wave functions are calculated in the Hartree approximation of the $\sigma-\omega$ model [36–38]. To take the IFSI into account, the wave functions of the impinging, scattered, and ejected nucleon are obtained in distorted-wave theory.

The IFSI effects are typically computed in the distorted-wave impulse approximation (DWIA) framework [3, 4, 11, 39]. In a DWIA approach, the scattering wave functions of the incoming and two outgoing nucleons are generated by solving the Schrödinger or Dirac equation with complex optical potentials. Parametrizations for these optical potentials are usually not gained from basic grounds, but are obtained by fitting elastic nucleon-nucleus scattering data. Several sets of optical-potential parameters [9, 40–46] have been used in the description of quasifree proton scattering off nuclei. In the past, both nonrelativistic and relativistic DWIA versions [5, 6, 8–10, 24–32, 47–51] have proven successful in predicting $A(p,pN)$ cross sections over a wide energy range (76–600 MeV) and for a whole scope of target nuclei. The comparison of $A(\vec{p},2p)$ analyzing power calculations with data, on the other hand, clearly demonstrated the superiority of the relativistic descriptions of the spin observables [32, 52, 53]. Even with the Dirac equation, however, predicting the spin observables for exclusive proton-knockout reactions remains problematic [32, 52, 53].

Most calculations for the exclusive $A(p,pN)$ process addressed incident proton kinetic energies of a few hundred MeV. In this work, we aim at developing a formalism that extends to scattering in the GeV energy regime. As a matter of fact, the majority of DWIA frameworks rely on partial-wave expansions of the exact solution to the scattering problem, an approach which becomes increasingly cumbersome at higher energies. In this energy range, the eikonal approximation (EA) [54, 55], which belongs to the class of high-energy semiclassical methods, offers a valid alternative for describing the IFSI. Nonrelativistic eikonal studies of

the $A(p,2p)$ reaction used in combination with optical potentials can be found in Refs. [1,5,7].

In this work, we present a relativistic formulation of the eikonal approximation. Hereby, we extend a model developed by our research group, which was initially designed for the description of exclusive electron-nucleus scattering processes [56–59], to deal with the IFSI in quasielastic proton-nucleus scattering. Our eikonal framework can accomodate both optical potentials and a multiple-scattering extension, Glauber theory. As such, the theoretical model can be formally applied in a wide energy range.

Outline

The outline of this work is as follows.

- In Chapter 2, a relativistic and cross-section factorized framework for computing quasielastic $A(p,pN)$ observables at intermediate and high energies is presented. First, a factorized expression for the differential $A(p,pN)$ cross section is derived. The remainder of this chapter is devoted to the various eikonal methods to deal with the IFSI. Both an optical-potential and a Glauber model are addressed. The optical-potential philosophy, which starts from a nucleon-nucleus picture, is particularly useful at lower nucleon energies. The Glauber method has nucleon-nucleon scattering as a starting basis and is more natural at higher energies. This versatility in describing the IFSI will allow us to describe $A(p,pN)$ reactions in a wide energy range. The Glauber calculations are very demanding as far as computing power is concerned since they involve multi-dimensional integrals over the positions of all spectator nucleons. In order to reduce computer time, an approximated version of our Glauber framework is introduced. Its validity will be investigated in Chapter 4. Finally, a second-order correction to the eikonal prescription is devised. This will enable us to probe the low-energy validity limit of the eikonal approach (see Chapter 5).

- Chapter 3 starts with a detailed study of the properties of the IFSI factor in $A(p,pN)$ reactions, a function wherein the entire effect of the IFSI is contained. Next, in order to visualize which parts of the target nucleus are probed by

the $A(p,pN)$ reaction, the radial and polar-angle contributions to the cross sections are investigated. The results show that $A(p,pN)$ scattering events mainly take place at the nuclear surface. Further, our cross-section calculations are compared to a wide variety of $A(p,pN)$ experiments. We present results for the target nuclei ^{4}He, ^{12}C, ^{16}O, and ^{40}Ca, and for different kinematical settings.

- The nuclear transparency extracted from $A(p,2p)$ scattering processes is the subject of Chapter 4. This observable gives a measure of the survival probability for the protons to enter and exit the nucleus without any further interactions with the spectator nucleons. We start this chapter with a description of the features of high-momentum-transfer wide-angle proton-proton scattering. There is a discussion of the different mechanisms playing a role in this reaction: the quark-counting and the Landshoff scattering. Next, a relativistic framework for computing the $A(p,2p)$ nuclear transparency is developed. Here, the nuclear filtering mechanism is implemented as a possible explanation for the oscillatory energy dependence of the transparency. The phenomenon of color transparency (CT) is taken into account as well. The special conditions necessary to observe CT are discussed and two existing models are used for its description. Finally, results are shown for the target nuclei ^{7}Li, ^{12}C, ^{27}Al, and ^{63}Cu. The approximated, computationally less intensive version of the Glauber framework is found to be sufficiently accurate for the calculation of the nuclear transparency. After including the nuclear filtering and color transparency mechanisms, our calculations are in acceptable agreement with the data. As the outlook states, however, there remain a number of unanswered questions in connection with the nuclear transparency.

- Due to its appealing potential, the eikonal approximation is widely used. However, it is not clear down to which energies the eikonal approach is adequate. Therefore, in Chapter 5, we turn our attention to lower energies and investigate the accuracy of the eikonal approximation by taking second-order corrections into account. We restrict ourselves to $A(e,e'p)$ observables. First, the effect of the second-order corrections on the $A(e,e'p)$ nuclear transparency is studied. Next, we focus on truly exclusive observables such as the induced normal polarization, the left-right asymmetry, and the differential cross sec-

tion. These observables are expected to be more sensitive to the details of the final-state interactions than the nuclear transparency, which is an integrated quantity. As such, the eikonal approximation is put to an even more stringent test. On the whole, the effect of the second-order corrections is found to be rather small down to four-momentum transfers $Q^2 = 0.2$ (GeV/c)^2 which corresponds with proton kinetic energies of slightly above 100 MeV.

- Finally, Chapter 6 summarizes our findings and states our conclusions.

Chapter 2

Relativistic Eikonal Description of $A(p, pN)$ Reactions

The interpretation of quasielastic nucleon-knockout reaction experiments heavily depends on the availability of realistic models for the description of nucleon propagation through the nuclear medium. With three nucleons subject to IFSI effects, this is certainly the case for $A(p, pN)$ reactions. Unfortunately, there exists no uniform framework which can compute these attenuation effects for both "low" and "high" energies. At lower energies, most theoretical work on IFSI is performed in the DWIA framework [3,4,11,39]. The scattering state is obtained as a partial-wave expansion and nucleon-nucleus optical potentials are used to estimate the effect of the scatterings on the propagating particle. The validity of these DWIA models becomes questionable for nucleon kinetic energies exceeding 1 GeV. The first reason for this is that the number of partial waves needed to reach convergence increases rapidly with energy. Next, global parametrizations of optical potentials are usually restricted to nucleon kinetic energies below 1 GeV. Finally, the elementary nucleon-nucleon interaction becomes highly inelastic above 1 GeV, making optical potentials unnatural in this high-energy regime. An alternative and economical description of IFSI is offered by the eikonal method [54, 55], which finds its origins in optics [60, 61]. Being a semiclassical method, the EA becomes useful when the de Broglie wavelength $\lambda_{dB} = h/p$ of the particle with momentum p is small compared to the typical range a of the potential. This short-wavelength condition is equivalent to the requirement that $ka \gg 1$, with $k = p/\hbar$ the particle's wavenumber.

Fig. 2.1 depicts the dependence of the de Broglie wavelength of the knocked-out nucleon on the energy transfer ω. The de Broglie wavelength is approximately given by $\lambda_{dB} = \frac{hc}{\sqrt{\omega^2+2M_N\omega}}$, a relation obtained by neglecting the momentum of the residual nucleus relative to its rest mass. Since the interaction range a is typically of the order of a few fm, the condition to be fulfilled can be written as $\omega \gg 500$ MeV. An additional assumption is that $|V_0|/E \ll 1$, with V_0 the typical strength of the potential and E the energy of the particle.

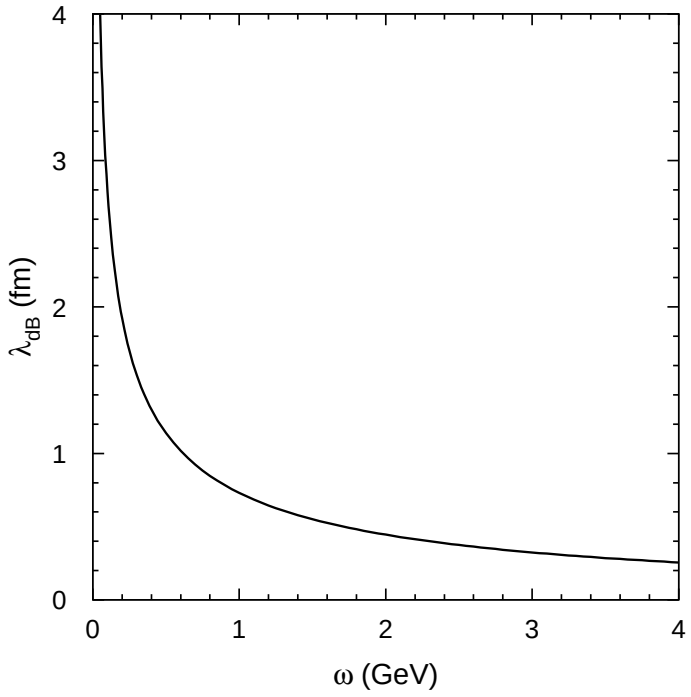

Figure 2.1 The de Broglie wavelength λ_{dB} of the knocked-out nucleon as a function of the energy ω transferred in an $A(p, pN)$ reaction.

In this chapter, we propose a relativistic and cross-section factorized formalism for computing exclusive $A(p, pN)$ cross sections at incident proton energies in the few hundred MeV to GeV range. Our approach is founded on the impulse approximation and we adopt the eikonal approximation to incorporate the IFSI effects. The eikonal formalism is implemented relativistically in combination with optical po-

tentials [9,46], as well as with Glauber theory [62–64], which is a multiple-scattering extension of the EA. The two frameworks only differ in the way they treat the IFSI.

This chapter is organized as follows. In Sections 2.1.1 and 2.1.2, the factorized cross section is derived in the relativistic plane-wave impulse approximation (RPWIA) formalism. An expression for the differential $A(p, pN)$ cross section when implementing IFSI effects is formulated in Section 2.1.3. The different eikonal methods to deal with the IFSI are developed in the following sections. In Section 2.2, the relativistic eikonal approximation is introduced and complex optical potentials are implemented to describe the IFSI distortions. Next, the Glauber multiple-scattering extension of the eikonal method is developed in Section 2.3. A numerically less intensive version of the Glauber framework is derived in Section 2.4, while Section 2.5 is devoted to the derivation of a second-order correction to the relativistic optical model eikonal approximation of Section 2.2.

2.1 Observables and Kinematics

In this section, the formalism for the description of $A(p, 2p)$ reactions is outlined. The generalization to $A(p, pn)$ reactions is straightforward. We conform to the conventions of Bjorken and Drell [65] for the γ matrices and the Dirac spinors, and we take $\hbar = c = 1$. The four-momenta of the incident and scattered proton are denoted as $P_1^\mu(E_{p1}, \vec{p}_1)$ and $K_1^\mu(E_{k1}, \vec{k}_1)$. The proton momenta $\vec{p}_1$ and $\vec{k}_1$ define the scattering plane. The four-momentum transfer is given by $(\omega, \vec{q}) \equiv q^\mu = P_1^\mu - K_1^\mu = K_{A-1}^\mu + K_2^\mu - K_A^\mu$, where $K_A^\mu(E_A, \vec{k}_A)$, $K_{A-1}^\mu(E_{A-1}, \vec{k}_{A-1})$, and $K_2^\mu(E_{k2}, \vec{k}_2)$ are the four-momenta of the target nucleus, residual nucleus, and the ejected proton. The standard convention $Q^2 \equiv -q_\mu q^\mu = |\vec{q}|^2 - \omega^2 \geq 0$ is followed for the four-momentum transfer. m_{s1i}, m_{s1f}, and m_{s2f} represent the spins of the incoming, scattered, and ejected proton, respectively.

2.1.1 The $A(p,2p)$ Scattering Cross Section and Matrix Element

In the laboratory frame, the exclusive differential cross section for $p + A \rightarrow p + p + (A-1)$ processes can be written as [65]

$$d\sigma = \frac{1}{\beta}\frac{M_p}{E_{p1}}\frac{M_A}{E_A}\overline{\sum_{if}}\left|\mathcal{M}_{fi}^{(p,2p)}\right|^2 \frac{M_p}{E_{k1}}\frac{d^3\vec{k}_1}{(2\pi)^3}\frac{M_{A-1}}{E_{A-1}}\frac{d^3\vec{k}_{A-1}}{(2\pi)^3}\frac{M_p}{E_{k2}}\frac{d^3\vec{k}_2}{(2\pi)^3} \times(2\pi)^4\,\delta^{(4)}\left(P_1^\mu + K_A^\mu - K_1^\mu - K_2^\mu - K_{A-1}^\mu\right)\,, \tag{2.1}$$

where β is the relative initial velocity and $\overline{\sum_{if}}$ corresponds to the appropriate average over initial states and sum over final states. All particle states are assumed to be normalized to unity [65]. Further, M_p, M_A, and M_{A-1} are the rest masses of the proton, the target nucleus, and the residual nucleus, respectively.

Integrating over the unobserved momentum of the recoiling nucleus $\vec{k}_{A-1}$, as well as over $|\vec{k}_2|$, results in the following fivefold differential cross section

$$\left(\frac{d^5\sigma}{dE_{k1}d\Omega_1 d\Omega_2}\right) = \frac{M_p^3 M_{A-1}}{(2\pi)^5 M_A}\frac{k_1 k_2}{p_1}\,f_{\rm rec}^{-1}\overline{\sum_{if}}\left|\mathcal{M}_{fi}^{(p,2p)}\right|^2\,. \tag{2.2}$$

Here, the hadronic recoil factor is given by

$$f_{\rm rec} = \frac{E_{A-1}}{E_A}\left|1 + \frac{E_{k2}}{E_{A-1}}\left(1 - \frac{\vec{q}\cdot\vec{k}_2}{k_2^2}\right)\right| = \left|1 + \frac{\omega k_2 - qE_{k2}\cos\theta_{k_2q}}{M_A k_2}\right|\,, \tag{2.3}$$

with the energy transfer $\omega = E_{p1} - E_{k1} = E_{A-1} + E_{k2} - E_A$, the three-momentum transfer $\vec{q} = \vec{p}_1 - \vec{k}_1 = \vec{k}_{A-1} + \vec{k}_2 - \vec{k}_A$, and θ_{k_2q} the angle between $\vec{k}_2$ and $\vec{q}$.

The invariant $A(p,2p)$ matrix element $\mathcal{M}_{fi}^{(p,2p)}$ which reflects the transition between the initial and final states, is given by

$$\mathcal{M}_{fi}^{(p,2p)} = \tag{2.4}$$
$$\left\langle K_1^\mu\, m_{s1f},\; K_2^\mu\, m_{s2f},\; A-1\,(K_{A-1}^\mu,\, J_R\, M_R)\right|\widehat{\mathcal{O}}^{(2)}\left|P_1^\mu\, m_{s1i},\; A\,(K_A^\mu,\, 0^+,\, g.s.)\right\rangle\,,$$

where

$$\widehat{\mathcal{O}}^{(2)} = \sum_{i<j=0}^{A}\widehat{O}\,(\vec{r}_i,\vec{r}_j) \tag{2.5}$$

is the unknown two-body operator describing the high-momentum transfer hard pp scattering. Further, $\left|A\,(K_A^\mu,\, 0^+,\, g.s.)\right\rangle$ is the ground state of the even-even target nucleus, and $\left|A-1\,(K_{A-1}^\mu,\, J_R\, M_R)\right\rangle$ the discrete state in which the residual

nucleus is left. In coordinate space, the matrix element takes on the form

$$\begin{aligned}\mathcal{M}_{fi}^{(p,2p)} &= \int d\vec{r}_0 \int d\vec{r}_1 \int d\vec{r}_2 \cdots \int d\vec{r}_A \left(\Psi_{A+1}^{\vec{k}_1, m_{s1f}, \vec{k}_2, m_{s2f}} \left(\vec{r}_0, \vec{r}_1, \vec{r}_2, \ldots, \vec{r}_A\right) \right)^{\dagger} \\ &\times \sum_{i<j=0}^{A} \widehat{O}\left(\vec{r}_i, \vec{r}_j\right) \Psi_{A+1}^{\vec{p}_1, m_{s1i}, gs} \left(\vec{r}_0, \vec{r}_1, \vec{r}_2, \ldots, \vec{r}_A\right) . \end{aligned} \tag{2.6}$$

For the sake of brevity of the notations, only the spatial coordinates are explicitly written.

2.1.2 Relativistic Plane-Wave Impulse Approximation

In this section, the $A(p,2p)$ matrix element of Eq. (2.6) will be evaluated in the RPWIA. In this approach, the cross section is determined by the hard collision between the projectile and a bound nucleon, thereby ignoring all soft IFSI processes.

In evaluating the $A(p,2p)$ matrix element of Eq. (2.6), a mean-field approximation for the nuclear wave functions is adopted. We also assume factorization between the hard NN coupling and the nuclear dynamics. For reasons of conciseness, the forthcoming derivations are exposed for the $A = 3$ case. The generalization to arbitrary mass number A is rather straightforward.

The antisymmetrized $(A+1)$-body wave function in the initial state is of the Slater determinant form

$$\begin{aligned}&\Psi_{A+1}^{\vec{p}_1, m_{s1i}, gs} \left(\vec{r}_0, \vec{r}_1, \vec{r}_2, \vec{r}_3\right) \\ &= \frac{1}{\sqrt{(A+1)!}} \begin{vmatrix} \phi_{\vec{p}_1 m_{s1i}}\left(\vec{r}_0\right) & \phi_{\alpha_1}\left(\vec{r}_0\right) & \phi_{\alpha_2}\left(\vec{r}_0\right) & \phi_{\alpha_3}\left(\vec{r}_0\right) \\ \phi_{\vec{p}_1 m_{s1i}}\left(\vec{r}_1\right) & \phi_{\alpha_1}\left(\vec{r}_1\right) & \phi_{\alpha_2}\left(\vec{r}_1\right) & \phi_{\alpha_3}\left(\vec{r}_1\right) \\ \phi_{\vec{p}_1 m_{s1i}}\left(\vec{r}_2\right) & \phi_{\alpha_1}\left(\vec{r}_2\right) & \phi_{\alpha_2}\left(\vec{r}_2\right) & \phi_{\alpha_3}\left(\vec{r}_2\right) \\ \phi_{\vec{p}_1 m_{s1i}}\left(\vec{r}_3\right) & \phi_{\alpha_1}\left(\vec{r}_3\right) & \phi_{\alpha_2}\left(\vec{r}_3\right) & \phi_{\alpha_3}\left(\vec{r}_3\right) \end{vmatrix} . \end{aligned} \tag{2.7}$$

Details on the bound-state single-particle wave functions $\phi_{\alpha_i}\left(\vec{r}, \vec{\sigma}\right)$ entering this mean-field $(A+1)$-body wave function can be found in Appendix B. The wave function of the incoming proton is given by a relativistic plane wave

$$\phi_{\vec{k} m_s}\left(\vec{r}\right) \equiv \sqrt{\frac{E+M}{2M}} \begin{bmatrix} 1 \\ \frac{1}{E+M} \vec{\sigma} \cdot \hat{\vec{p}} \end{bmatrix} e^{i\vec{k}\cdot\vec{r}} \chi_{\frac{1}{2} m_s} = e^{i\vec{k}\cdot\vec{r}} u(\vec{k}, m_s) . \tag{2.8}$$

The $(A+1)$-body wave function in the final state reads

$$\Psi_{A+1}^{\vec{k}_1,m_{s1f},\vec{k}_2,m_{s2f}}\left(\vec{r}_0,\vec{r}_1,\vec{r}_2,\vec{r}_3\right) = \frac{1}{\sqrt{(A+1)!}} \begin{vmatrix} \phi_{\vec{k}_1 m_{s1f}}\left(\vec{r}_0\right) & \phi_{\vec{k}_2 m_{s2f}}\left(\vec{r}_0\right) & \phi_{\alpha_2}\left(\vec{r}_0\right) & \phi_{\alpha_3}\left(\vec{r}_0\right) \\ \phi_{\vec{k}_1 m_{s1f}}\left(\vec{r}_1\right) & \phi_{\vec{k}_2 m_{s2f}}\left(\vec{r}_1\right) & \phi_{\alpha_2}\left(\vec{r}_1\right) & \phi_{\alpha_3}\left(\vec{r}_1\right) \\ \phi_{\vec{k}_1 m_{s1f}}\left(\vec{r}_2\right) & \phi_{\vec{k}_2 m_{s2f}}\left(\vec{r}_2\right) & \phi_{\alpha_2}\left(\vec{r}_2\right) & \phi_{\alpha_3}\left(\vec{r}_2\right) \\ \phi_{\vec{k}_1 m_{s1f}}\left(\vec{r}_3\right) & \phi_{\vec{k}_2 m_{s2f}}\left(\vec{r}_3\right) & \phi_{\alpha_2}\left(\vec{r}_3\right) & \phi_{\alpha_3}\left(\vec{r}_3\right) \end{vmatrix} . \tag{2.9}$$

Relative to the target nucleus ground state written in Eq. (2.7), the wave function of Eq. (2.9) refers to the situation whereby the struck proton resides in a state "α_1", leaving the residual $A-1$ nucleus as a hole state in that particular single-particle level. The outgoing protons are represented by relativistic plane waves.

Since both the initial and the final wave functions are fully antisymmetrized, one can choose the operator $\widehat{\mathcal{O}}^{(2)}$ to act on two particular coordinates ($\vec{r}_0$ and $\vec{r}_1$). Without any loss of generality, the $A(p,2p)$ matrix element of Eq. (2.6) can be written as

$$\begin{aligned} \mathcal{M}_{fi}^{(p,2p)} &= \frac{A(A+1)}{2}\frac{1}{(A+1)!}\int d\vec{r}_0\int d\vec{r}_1\int d\vec{r}_2\int d\vec{r}_3 \\ &\times \sum_{k,l\in\left\{\vec{k}_1 m_{s1f},\vec{k}_2 m_{s2f}\right\}}\ \sum_{m,n\in\{\alpha_2,\alpha_3\}}\ \sum_{o,p\in\{\vec{p}_1 m_{s1i},\alpha_1\}}\ \sum_{q,r\in\{\alpha_2,\alpha_3\}} \\ &\times \epsilon_{klmn}\,\epsilon_{opqr}\,\phi_k^\dagger\left(\vec{r}_0\right)\phi_l^\dagger\left(\vec{r}_1\right)\phi_m^\dagger\left(\vec{r}_2\right)\phi_n^\dagger\left(\vec{r}_3\right) \\ &\times \widehat{O}\left(\vec{r}_0,\vec{r}_1\right)\phi_o\left(\vec{r}_0\right)\phi_p\left(\vec{r}_1\right)\phi_q\left(\vec{r}_2\right)\phi_r\left(\vec{r}_3\right)\ , \end{aligned} \tag{2.10}$$

with ϵ_{ijkl} the Levi-Civita tensor. In the RPWIA,

$$\begin{aligned} &\int d\vec{r}_0\int d\vec{r}_1\int d\vec{r}_2\,\phi_k^\dagger\left(\vec{r}_0\right)\phi_l^\dagger\left(\vec{r}_1\right)\phi_m^\dagger\left(\vec{r}_2\right)\widehat{O}\left(\vec{r}_0,\vec{r}_1\right)\phi_o\left(\vec{r}_0\right)\phi_p\left(\vec{r}_1\right)\phi_q\left(\vec{r}_2\right) \\ &= \delta_{mq}\int d\vec{r}_0\int d\vec{r}_1\int d\vec{r}_2\,\phi_k^\dagger\left(\vec{r}_0\right)\phi_l^\dagger\left(\vec{r}_1\right) \\ &\quad\times \widehat{O}\left(\vec{r}_0,\vec{r}_1\right)\phi_o\left(\vec{r}_0\right)\phi_p\left(\vec{r}_1\right)\left|\phi_q\left(\vec{r}_2\right)\right|^2\ . \end{aligned} \tag{2.11}$$

Inserting this expression in Eq. (2.10), one obtains

$$\begin{aligned} \mathcal{M}_{fi}^{(p,2p)} &= \frac{A(A+1)}{2}\frac{1}{(A+1)!}\int d\vec{r}_0\int d\vec{r}_1\int d\vec{r}_2\int d\vec{r}_3 \\ &\times \sum_{k,l\in\left\{\vec{k}_1 m_{s1f},\vec{k}_2 m_{s2f}\right\}}\ \sum_{o,p\in\{\vec{p}_1 m_{s1i},\alpha_1\}}\ \sum_{m,n\in\{\alpha_2,\alpha_3\}} \\ &\times \epsilon_{klmn}\,\epsilon_{opmn}\,\phi_k^\dagger\left(\vec{r}_0\right)\phi_l^\dagger\left(\vec{r}_1\right)\left|\phi_m\left(\vec{r}_2\right)\right|^2\left|\phi_n\left(\vec{r}_3\right)\right|^2 \\ &\times \widehat{O}\left(\vec{r}_0,\vec{r}_1\right)\phi_o\left(\vec{r}_0\right)\phi_p\left(\vec{r}_1\right)\ . \end{aligned} \tag{2.12}$$

There are $(A-1)!$ possible choices (permutations) for the indices $m, n, \ldots$, all giving the same contribution to the matrix element. Accordingly, the above expression can be rewritten as

$$\begin{aligned}\mathcal{M}_{fi}^{(p,2p)} &= \frac{1}{2}\int d\vec{r}_0 \int d\vec{r}_1 \int d\vec{r}_2 \int d\vec{r}_3 \sum_{k,l\in\left\{\vec{k}_1 m_{s1f}, \vec{k}_2 m_{s2f}\right\}} \sum_{o,p\in\{\vec{p}_1 m_{s1i}, \alpha_1\}} \\ &\times \epsilon_{kl\alpha_2\alpha_3}\, \epsilon_{op\alpha_2\alpha_3}\, \phi_k^\dagger\left(\vec{r}_0\right) \phi_l^\dagger\left(\vec{r}_1\right) \left|\phi_{\alpha_2}\left(\vec{r}_2\right)\right|^2 \left|\phi_{\alpha_3}\left(\vec{r}_3\right)\right|^2 \\ &\times \widehat{O}\left(\vec{r}_0, \vec{r}_1\right) \phi_o\left(\vec{r}_0\right) \phi_p\left(\vec{r}_1\right) \ . \end{aligned} \tag{2.13}$$

Because the bound-state wave functions are normalized to unity ($\int d\vec{r}\, \left|\phi_\alpha\left(\vec{r}\right)\right|^2 = 1$) and $\widehat{O}\left(\vec{r}_0, \vec{r}_1\right) = \widehat{O}\left(\vec{r}_1, \vec{r}_0\right)$, the matrix element can be further simplified to

$$\begin{aligned}\mathcal{M}_{fi}^{(p,2p)} &= \int d\vec{r}_0 \int d\vec{r}_1 \left(\phi^\dagger_{\vec{k}_1 m_{s1f}}\left(\vec{r}_0\right) \phi^\dagger_{\vec{k}_2 m_{s2f}}\left(\vec{r}_1\right) - \phi^\dagger_{\vec{k}_2 m_{s2f}}\left(\vec{r}_0\right) \phi^\dagger_{\vec{k}_1 m_{s1f}}\left(\vec{r}_1\right)\right) \\ &\times \widehat{O}\left(\vec{r}_0, \vec{r}_1\right) \phi_{\vec{p}1 m_{s1i}}\left(\vec{r}_0\right) \phi_{\alpha_1}\left(\vec{r}_1\right) \ , \end{aligned} \tag{2.14}$$

including a direct and an exchange term.

Substitution of the general form of the scattering operator

$$\widehat{O}\left(\vec{r}_0, \vec{r}_1\right) = \int \frac{d\vec{p}}{(2\pi)^3}\, e^{i\vec{p}\cdot\left(\vec{r}_1 - \vec{r}_0\right)}\, \widehat{F}\left(\vec{p}\right) \ , \tag{2.15}$$

where $\widehat{F}\left(\vec{p}\right)$ is the NN scattering amplitude in momentum space, in the above expression (2.14) leads to

$$\begin{aligned}&\int \frac{d\vec{p}}{(2\pi)^3} \int d\vec{r}_0 \int d\vec{r}_1\, e^{-i\vec{k}_1\cdot\vec{r}_0}\, u^\dagger(\vec{k}_1, m_{s1f})\, e^{-i\vec{k}_2\cdot\vec{r}_1}\, u^\dagger(\vec{k}_2, m_{s2f})\, e^{i\vec{p}\cdot\left(\vec{r}_1 - \vec{r}_0\right)} \\ &\quad\times \widehat{F}\left(\vec{p}\right)\, e^{i\vec{p}_1\cdot\vec{r}_0}\, u(\vec{p}_1, m_{s1i})\, \phi_{\alpha_1}\left(\vec{r}_1\right) \\ &= u^\dagger(\vec{k}_1, m_{s1f})\, u^\dagger(\vec{k}_2, m_{s2f})\, \widehat{F}\left(\vec{p}_1 - \vec{k}_1\right)\, u(\vec{p}_1, m_{s1i})\, \phi_{\alpha_1}\left(\vec{p}_m\right) \end{aligned} \tag{2.16}$$

for the direct term and a similar expression for the exchange term. Here, $\phi_\alpha\left(\vec{p}\right)$ is the relativistic wave function for the bound nucleon in momentum space (for details see Appendix B) and $\vec{p}_m = \vec{k}_1 + \vec{k}_2 - \vec{p}_1$ is the missing momentum. In order to arrive at a cross-section factorized expression for Eq. (2.2), the quasielastic off-shell proton-proton scattering matrix element will be related to the free on-shell proton-proton cross section. For this purpose, we insert the completeness relation

$$\sum_{m_s} \left[u(\vec{p}_m, m_s)\, \bar{u}(\vec{p}_m, m_s) - v(\vec{p}_m, m_s)\, \bar{v}(\vec{p}_m, m_s)\right] = 1 \tag{2.17}$$

in

$$\begin{aligned}\mathcal{M}_{fi}^{(p,2p)} &= u^{\dagger}(\vec{k}_1, m_{s1f})\, u^{\dagger}(\vec{k}_2, m_{s2f})\, \widehat{F}\left(\vec{p}_1 - \vec{k}_1\right)\, u(\vec{p}_1, m_{s1i})\, \phi_{\alpha_1}(\vec{p}_m) \\ &\quad - \left(\vec{k}_1 m_{s1f} \leftrightarrow \vec{k}_2 m_{s2f}\right) , \end{aligned} \tag{2.18}$$

and obtain the following expression for the matrix element:

$$\begin{aligned}\mathcal{M}_{fi}^{(p,2p)} &= \sum_{m_s} \left(\mathcal{M}_{fi}^{pp}\right)_{m_{s1i}, m_s, m_{s1f}, m_{s2f}} \bar{u}(\vec{p}_m, m_s)\, \phi_{\alpha_1}(\vec{p}_m) \\ &\quad - \text{negative-energy projection term} . \end{aligned} \tag{2.19}$$

Here, $\mathcal{M}_{fi}^{pp}$ is the matrix element for free pp scattering

$$\begin{aligned}&\left(\mathcal{M}_{fi}^{pp}\right)_{m_{s1i}, m_{s2i}, m_{s1f}, m_{s2f}} \\ &= u^{\dagger}(\vec{k}_1, m_{s1f})\, u^{\dagger}(\vec{k}_2, m_{s2f})\, \widehat{F}\left(\vec{p}_1 - \vec{k}_1\right)\, u(\vec{p}_1, m_{s1i})\, u(\vec{p}_2, m_{s2i}) \\ &\quad - \left(\vec{k}_1 m_{s1f} \leftrightarrow \vec{k}_2 m_{s2f}\right) . \end{aligned} \tag{2.20}$$

At the level of the differential cross section, the decomposition of Eq. (2.19) results in three terms: two terms proportional to the square of the positive-energy $\bar{u}\,\phi_\alpha$ and negative-energy $\bar{v}\,\phi_\alpha$ projection, respectively, and a cross term containing the product of the positive- and negative-energy projections. Using expression (B.7) for the relativistic bound-nucleon wave function in momentum space, the $\bar{u}\phi_\alpha$ and $\bar{v}\,\phi_\alpha$ contractions reduce to [66]

$$\bar{u}(\vec{p}, m_s)\, \phi_\alpha(\vec{p}) = (-i)^l\, (2\pi)^{3/2}\, \tilde{\alpha}_{n\kappa}(p)\, \chi^{\dagger}_{\frac{1}{2} m_s}\, \mathcal{Y}_{\kappa m}(\Omega_p) , \tag{2.21}$$

$$\bar{v}(\vec{p}, m_s)\, \phi_\alpha(\vec{p}) = (-i)^l\, (2\pi)^{3/2}\, \tilde{\beta}_{n\kappa}(p)\, \chi^{\dagger}_{\frac{1}{2} m_s}\, \mathcal{Y}_{-\kappa m}(\Omega_p) , \tag{2.22}$$

where $\chi^{\dagger}_{\frac{1}{2} m_s}\, \mathcal{Y}_{\pm\kappa m}$ indicates the spin projection of the spin spherical harmonic $\mathcal{Y}_{\pm\kappa m}(\Omega_p)$ on a spin state $\chi_{\frac{1}{2} m_s}$ and the radial functions in momentum space $\tilde{\alpha}_{n\kappa}$ and $\tilde{\beta}_{n\kappa}$ are given by

$$\tilde{\alpha}_{n\kappa}(p) = \sqrt{\frac{\bar{E} + M_p}{2M_p}}\, \left(g_{n\kappa}(p) - \frac{p}{\bar{E} + M_p}\, S_\kappa\, f_{n\kappa}(p)\right) , \tag{2.23}$$

$$\tilde{\beta}_{n\kappa}(p) = \sqrt{\frac{\bar{E} + M_p}{2M_p}}\, \left(\frac{p}{\bar{E} + M_p}\, g_{n\kappa}(p) - S_\kappa\, f_{n\kappa}(p)\right) , \tag{2.24}$$

with $g_{n\kappa}$ and $f_{n\kappa}$ the Bessel transforms of the upper and lower radial functions of the bound-nucleon wave function in coordinate space (see Eq. (B.8)), $\bar{E} = \sqrt{p^2 + M_p^2}$ and $S_\kappa = \kappa/|\kappa|$. As such, the contribution to the differential cross section from positive- (negative-)energy projections only is proportional to the momentum distribution component $|\tilde{\alpha}_{n\kappa}(p_m)|^2$ ($|\tilde{\beta}_{n\kappa}(p_m)|^2$), while the cross term is proportional to $2|\tilde{\alpha}_{n\kappa}(p_m)\,\tilde{\beta}_{n\kappa}(p_m)|$. In Fig. 2.2 the projection components of the momentum distribution are shown for the $1p_{1/2}$ shell of ^{16}O. The component $|\tilde{\alpha}_{n\kappa}(p_m)|^2$ clearly dominates in the region $p_m \leq 300$ MeV/c. In fact, in the maximum at $p_m \approx 100$ MeV/c, it is one order of magnitude larger than the $2|\tilde{\alpha}_{n\kappa}(p_m)\,\tilde{\beta}_{n\kappa}(p_m)|$ component and more than two orders of magnitude larger than the $|\tilde{\beta}_{n\kappa}(p_m)|^2$ component. At high missing momenta $p_m > 300$ MeV/c, the situation is clearly different. In this p_m region, the values of the components $2|\tilde{\alpha}_{n\kappa}(p_m)\,\tilde{\beta}_{n\kappa}(p_m)|$ and $|\tilde{\beta}_{n\kappa}(p_m)|^2$ are similar to or even larger than that of $|\tilde{\alpha}_{n\kappa}(p_m)|^2$.

Owing to the presence of the negative-energy projection term, factorization breaks down, even when IFSI are disregarded. To recover factorization, the negative-energy projection term is neglected in the remainder of this work

$$\mathcal{M}_{fi}^{(p,2p)} \approx \sum_{m_s} \left(\mathcal{M}_{fi}^{pp}\right)_{m_{s1i},m_s,m_{s1f},m_{s2f}} \bar{u}(\vec{p}_m, m_s)\,\phi_{\alpha_1}(\vec{p}_m)\ . \tag{2.25}$$

In view of the relative importance of the $|\tilde{\alpha}_{n\kappa}(p_m)|^2$ term, this approximation may be expected to be adequate up to missing momenta $p_m \approx 300$ MeV/c. Upon squaring Eq. (2.25), the pp and nuclear bound-state parts get coupled by the summation over the intermediate spins m_s and m_s':

$$\begin{aligned}\left|\mathcal{M}_{fi}^{(p,2p)}\right|^2 \approx & \sum_{m_s,m_s'} \left(\mathcal{M}_{fi}^{pp}\right)^*_{m_{s1i},m_s,m_{s1f},m_{s2f}} \left(\mathcal{M}_{fi}^{pp}\right)_{m_{s1i},m_s',m_{s1f},m_{s2f}} \\ & \times \left(\bar{u}(\vec{p}_m, m_s)\,\phi_{\alpha_1}(\vec{p}_m)\right)^* \bar{u}(\vec{p}_m, m_s')\,\phi_{\alpha_1}(\vec{p}_m)\ .\end{aligned} \tag{2.26}$$

After summation over m, the struck nucleon's generalized angular momentum quantum number, the square of $\bar{u}(\vec{p}_m, m_s)\,\phi_{\alpha_1}(\vec{p}_m)$ yields a $\delta_{m_s m_s'}$, i.e., becomes diagonal in m_s. Thereby, use is made of the identity

$$\sum_m \left(\chi^\dagger_{\frac{1}{2}m_s}\,\mathcal{Y}_{\kappa m}\right)^* \chi^\dagger_{\frac{1}{2}m_s'}\,\mathcal{Y}_{\kappa m} = \frac{2j+1}{8\pi}\,\delta_{m_s m_s'}\ . \tag{2.27}$$

This leads to the decoupling between the pp scattering and the bound-state part in

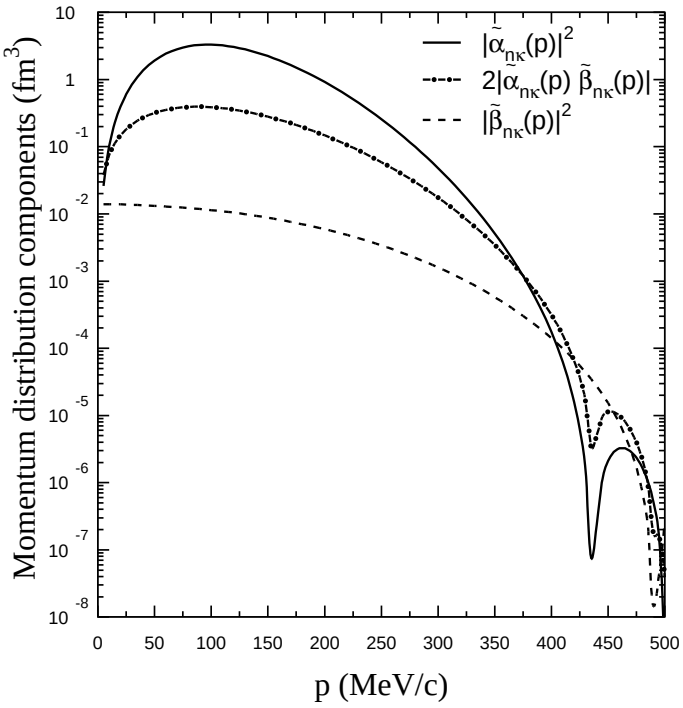

Figure 2.2 The projection components of the momentum distribution for the $1p_{1/2}$ shell of ^{16}O. The solid (dashed) line shows the contribution from positive- (negative-)energy projections only. The cross term, which involves both positive- and negative-energy projections, is represented by the dot-dashed line.

the matrix element:

$$\overline{\sum_{if}}\left|\mathcal{M}_{fi}^{(p,2p)}\right|^2 \approx (2\pi)^3\,\frac{2j+1}{8\pi}\,|\tilde{\alpha}_{n\kappa}\,(p_m)|^2 \times \overline{\sum}_{m_{s1i},m_{s1f},m_{s2f}}\sum_{m_s}\left|\left(\mathcal{M}_{fi}^{pp}\right)_{m_{s1i},m_s,m_{s1f},m_{s2f}}\right|^2 . \quad (2.28)$$

The last factor in Eq. (2.28) can be related to the free pp scattering center-of-mass

(c.m.) cross section

$$\left(\frac{d\sigma^{pp}}{d\Omega}\right)_{\rm c.m.} = \frac{M_p^4}{(2\pi)^2 s}\frac{1}{2}\overline{\sum}_{m_{s1i},m_{s1f},m_{s2f}}\sum_{m_s}\left|\left(\mathcal{M}^{pp}_{fi}\right)_{m_{s1i},m_s,m_{s1f},m_{s2f}}\right|^2 , \quad (2.29)$$

so that the RPWIA differential $A(p,2p)$ cross section of Eq. (2.2) can be written in the cross-section factorized form

$$\left(\frac{d^5\sigma}{dE_{k1}d\Omega_1 d\Omega_2}\right)^{\rm RPWIA} \approx \frac{sM_{A-1}}{M_p M_A}\frac{k_1 k_2}{p_1} f_{\rm rec}^{-1}\frac{2j+1}{4\pi}\left|\tilde{\alpha}_{n\kappa}\left(p_m\right)\right|^2\left(\frac{d\sigma^{pp}}{d\Omega}\right)_{\rm c.m.} . \quad (2.30)$$

Here, s is the Mandelstam variable for the pp scattering.

In the numerical calculations presented in Chapter 3, the free proton-nucleon cross section $\left(\frac{d\sigma^{pN}}{d\Omega}\right)_{\rm c.m.}$ is obtained from the SAID code [12,13] at an effective laboratory kinetic energy of

$$T_{\rm lab}^{\rm eff} = \frac{s-4M_p^2}{2M_p} \quad (2.31)$$

and a c.m. scattering angle $\theta_{\rm c.m.}$ given by

$$\cos\theta_{\rm c.m.} = \frac{t-u}{\sqrt{\left(s-4M_p^2\right)\left[\frac{(4M_p^2-t-u)^2}{s}-4M_p^2\right]}} , \quad (2.32)$$

with s, t, and u the Mandelstam variables for the pp scattering. For the nuclear transparency calculations of Chapter 4, the phenomenological parametrization of Ref. [67], which is more suitable at large s ($s \geq 7$ GeV^2) and c.m. scattering angle $\theta_{\rm c.m.} \approx 90^\circ$, is used (see Eq. (4.8)).

2.1.3 Treatment of the IFSI: Factorization Assumption and the Distorted Momentum Distribution

The factorized RPWIA result of Eq. (2.30) adopts an oversimplified description of the reaction mechanism. The momentum distribution $\frac{2j+1}{4\pi}\left|\tilde{\alpha}_{n\kappa}\left(p_m\right)\right|^2$, which represents the probability of finding a proton in the target nucleus with missing momentum $\vec{p}_m$, is modified by the scatterings of the incoming and outgoing protons in the nucleus. Therefore, it is necessary to incorporate the effects of these IFSI in the model.

In this section, the differential $A(p,2p)$ cross section is written in a factorized form taking IFSI effects into account. The relativistic eikonal methods used for

dealing with the IFSI effects will be discussed in depth in the forthcoming sections. Two methods will be used. The relativistic optical model eikonal approximation (ROMEA) is the subject of Section 2.2, whereas the relativistic multiple-scattering Glauber approximation (RMSGA) is discussed in Section 2.3.

In both versions of the relativistic eikonal framework for $A(p,pN)$ reactions (ROMEA and RMSGA), the antisymmetrized initial- and final-state $(A+1)$-body wave functions,

$$\begin{aligned}&\Psi_{A+1}^{\vec{p}_1,m_{s1i},gs}\left(\vec{r}_0,\vec{r}_1,\ldots,\vec{r}_A\right)\\ &\quad=\quad\widehat{\mathcal{A}}\left[\widehat{\mathcal{S}}_{p1}\left(\vec{r}_0,\vec{r}_2,\ldots,\vec{r}_A\right)e^{i\vec{p}_1\cdot\vec{r}_0}\,u(\vec{p}_1,m_{s1i})\,\Psi_A^{gs}\left(\vec{r}_1,\vec{r}_2,\ldots,\vec{r}_A\right)\right]\end{aligned}\tag{2.33}$$

and

$$\begin{aligned}\Psi_{A+1}^{\vec{k}_1,m_{s1f},\vec{k}_2,m_{s2f}}\left(\vec{r}_0,\vec{r}_1,\ldots,\vec{r}_A\right)=\widehat{\mathcal{A}}\Big[&\widehat{\mathcal{S}}_{k1}^{\dagger}\left(\vec{r}_0,\vec{r}_2,\ldots,\vec{r}_A\right)e^{i\vec{k}_1\cdot\vec{r}_0}\,u(\vec{k}_1,m_{s1f})\\ &\times\widehat{\mathcal{S}}_{k2}^{\dagger}\left(\vec{r}_1,\vec{r}_2,\ldots,\vec{r}_A\right)e^{i\vec{k}_2\cdot\vec{r}_1}\,u(\vec{k}_2,m_{s2f})\,\Psi_{A-1}^{J_R\,M_R}\left(\vec{r}_2,\ldots,\vec{r}_A\right)\Big]\,,\end{aligned}\tag{2.34}$$

differ from their RPWIA counterparts of Eqs. (2.7) and (2.9) through the presence of the operators $\widehat{\mathcal{S}}_{p1}$, $\widehat{\mathcal{S}}_{k1}$, and $\widehat{\mathcal{S}}_{k2}$. These define the accumulated effect of all interactions that the incoming and emerging protons undergo in their way into and out of the target nucleus.

Since the IFSI violate factorization, some additional approximations are in order. First, only central IFSI are considered. In both proton-nucleus and $A(e,e'p)$ scattering calculations (see, for example, Refs. [59,68]), it has been a common and successful practice to neglect spin effects. Hence, we expect a spinless treatment of the IFSI to be quite reasonable for the calculation of $A(p,pN)$ cross sections as well, especially at higher energies, since the contribution from spin-dependent terms decreases rapidly with energy. Of course, spin effects might play a more prominent role in the description of $A(p,2p)$ spin observables, but these observables will not be discussed in this work. Further, the zero-range approximation is adopted for the hard NN interaction, allowing one to replace the coordinates of the two interacting protons ($\vec{r}_0$ and $\vec{r}_1$) by one single collision point in the distorting functions $\widehat{\mathcal{S}}_{p1}$, $\widehat{\mathcal{S}}_{k1}$, and $\widehat{\mathcal{S}}_{k2}$. This leads to the distorted momentum-space wave function

$$\phi_{\alpha_1}^{D}\left(\vec{p}_m\right)=\int d\vec{r}\,e^{-i\vec{p}_m\cdot\vec{r}}\,\phi_{\alpha_1}\left(\vec{r}\right)\,\widehat{\mathcal{S}}_{\rm IFSI}\left(\vec{r}\right)\,,\tag{2.35}$$

similar to Eq. (B.7), but with the additional IFSI factor

$$\begin{aligned}\widehat{\mathcal{S}}_{\rm IFSI}(\vec{r}) &= \int d\vec{r}_2 \cdots \int d\vec{r}_A \, |\phi_{\alpha_2}(\vec{r}_2)|^2 \cdots |\phi_{\alpha_A}(\vec{r}_A)|^2 \, \widehat{\mathcal{S}}_{k1}(\vec{r},\vec{r}_2,\ldots,\vec{r}_A) \\ &\quad \times \widehat{\mathcal{S}}_{k2}(\vec{r},\vec{r}_2,\ldots,\vec{r}_A)\, \widehat{\mathcal{S}}_{p1}(\vec{r},\vec{r}_2,\ldots,\vec{r}_A) \end{aligned} \tag{2.36}$$

accounting for the soft IFSI effects.

Now, along the lines of [69], it is natural to define a distorted wave amplitude

$$\psi^D(\vec{p}_m) = \bar{u}(\vec{p}_m, m_s)\, \phi^D_{\alpha_1}(\vec{p}_m) \ , \tag{2.37}$$

so that the distorted momentum distribution is given by the square of this amplitude,

$$\rho^D(\vec{p}_m) = \frac{1}{(2\pi)^3} \sum_m \sum_{m_s} \left|\psi^D(\vec{p}_m)\right|^2 \ . \tag{2.38}$$

This distorted momentum distribution has the following properties. First, it takes into account the distortions for the incoming and outgoing protons. Second, it reduces to the plane-wave momentum distribution $\frac{2j+1}{4\pi}|\tilde{\alpha}_{n\kappa}(p_m)|^2$ in the plane-wave limit when assuming that $\phi_{\alpha_1}(\vec{p}_m)$ satisfies the relation

$$\frac{\vec{\sigma}\cdot\vec{p}}{\bar{E}+M_p}\phi^u = \phi^d \tag{2.39}$$

between the upper and lower components.

Using the ansatz (2.38) for the distorted momentum distribution, the differential $A(p,2p)$ cross section can be cast in the form

$$\left(\frac{d^5\sigma}{dE_{k1}d\Omega_1 d\Omega_2}\right)^D \approx \frac{sM_{A-1}}{M_p M_A}\frac{k_1 k_2}{p_1} f_{\rm rec}^{-1}\, \rho^D(\vec{p}_m) \left(\frac{d\sigma^{pp}}{d\Omega}\right)_{\rm c.m.} \ . \tag{2.40}$$

It differs from the RPWIA expression (2.30) through the introduction of a "distorted" momentum distribution ρ^D.

2.2 Relativistic Optical Model Eikonal Approximation

2.2.1 Nucleon-Nucleus Scattering

Following the discussion of Refs. [56,70], we consider the time-independent Dirac equation for a particle with relativistic energy $E=\sqrt{k^2+M_N^2}$ and spin state $\left|\frac{1}{2}m_s\right\rangle$ subject to a spherical Lorentz scalar $V_s(r)$ and vector potential $V_v(r)$

$$\hat{\mathcal{H}}\,\Psi^{(+)}_{\vec{k},m_s}(\vec{r}) = [\vec{\alpha}\cdot\hat{\vec{p}} + \beta M_N + \beta V_s(r) + V_v(r)]\,\Psi^{(+)}_{\vec{k},m_s}(\vec{r}) = E\,\Psi^{(+)}_{\vec{k},m_s}(\vec{r}) \ , \tag{2.41}$$

where $\Psi^{(+)}_{\vec{k},m_s}(\vec{r})$ is the unbound (scattered) Dirac state and $\hat{\vec{p}}$ represents the impulse operator. The influence of the nuclear medium on the particle is twofold: the scalar potential $V_s(r)$ shifts the particle mass to an effective value, while the vector potential $V_v(r)$ affects the energy term. The scattering wave function $\Psi^{(+)}_{\vec{k},m_s}(\vec{r})$ is decomposed in an upper and a lower component, $u^{(+)}_{\vec{k},m_s}(\vec{r})$ and $w^{(+)}_{\vec{k},m_s}(\vec{r})$. Some straightforward manipulations lead to a Schrödinger-like equation for the upper component

$$\left[-\frac{\nabla^2}{2M_N} + V_c(r) + V_{so}(r)\,(\vec{\sigma}\cdot\vec{L} - i\vec{r}\cdot\hat{\vec{p}})\right] u^{(+)}_{\vec{k},m_s}(\vec{r}) = \frac{k^2}{2M_N}\, u^{(+)}_{\vec{k},m_s}(\vec{r})\ , \qquad (2.42)$$

while the lower component is related to the upper one through

$$w^{(+)}_{\vec{k},m_s}(\vec{r}) = \frac{1}{E + M_N + V_s(r) - V_v(r)}\,\vec{\sigma}\cdot\hat{\vec{p}}\,u^{(+)}_{\vec{k},m_s}(\vec{r})\ . \qquad (2.43)$$

Here, the central and spin-orbit potentials $V_c(r)$ and $V_{so}(r)$ are defined as

$$\begin{aligned} V_c(r) &= V_s(r) + \frac{E}{M_N}V_v(r) + \frac{V_s^2(r) - V_v^2(r)}{2M_N}\ , \\ V_{so}(r) &= \frac{1}{2M_N[E + M_N + V_s(r) - V_v(r)]}\frac{1}{r}\frac{d}{dr}[V_v(r) - V_s(r)]\ . \end{aligned} \qquad (2.44)$$

So far, no approximations have been made. In the relativistic DWIA frameworks [24,25,29,30], the scattering wave function is expanded in partial waves

$$\Psi^{(+)}_{\vec{k},m_s}(\vec{r}) = 4\pi\sqrt{\frac{E+M_N}{2M_N}}\sum_{\kappa m m_l} i^l\,\langle l m_l \tfrac{1}{2} m_s | j m\rangle\, Y^*_{lm_l}(\Omega_k)\,\Psi^m_\kappa(\vec{r})\,, \qquad (2.45)$$

where $\Psi^m_\kappa(\vec{r})$ are four-spinors of the same form as the bound-state wave functions of Eq. (B.4), and Eq. (2.41) is solved numerically using optical potentials. This partial-wave procedure becomes impractical as the energy increases. Therefore, at higher energies, the Schrödinger-type equation (2.42) is solved in the eikonal approximation [56,70].

Following the method outlined in Ref. [70], the average momentum $\vec{K}$ and the momentum transfer $\vec{\Delta}$ which occur during the nucleon-nucleus collision, are defined in terms of the nucleon's initial ($\vec{k}_i$) and final momentum ($\vec{k}_f$)

$$\begin{aligned} \vec{K} &= \frac{\vec{k}_i + \vec{k}_f}{2}\ , \\ \vec{\Delta} &= \vec{k}_i - \vec{k}_f\ . \end{aligned} \qquad (2.46)$$

The EA is essentially a small-angle approximation ($\Delta/k_i \ll 1$) and hence, the following operatorial approximation is made [71]

$$\hat{p}^2 = [(\hat{\vec{p}} - \vec{K}) + \vec{K}]^2 \simeq 2\vec{K}\cdot\hat{\vec{p}} - K^2 \ . \tag{2.47}$$

Through this, the equation for the upper component becomes linear in the momentum operator:

$$\left[\vec{K}\cdot\hat{\vec{p}} - K^2 + M_N\left\{V_c(r) + V_{so}(r)\,(\vec{\sigma}\cdot\vec{r}\times\vec{K} - i\vec{r}\cdot\vec{K})\right\}\right]\ u^{(+)}_{\vec{k},m_s}(\vec{r}) = 0\ , \tag{2.48}$$

where the momentum operators in the spin-orbit ($V_{so}(r)\,(\vec{\sigma}\cdot\vec{r}\times\hat{\vec{p}})$) and Darwin terms ($V_{so}(r)\,(-i\vec{r}\cdot\hat{\vec{p}})$) have been replaced by the average momentum $\vec{K}$. In the EA, the following ansatz is postulated for the upper component of the scattering wave function:

$$u^{(+)}_{\vec{k},m_s}(\vec{r}) \equiv N\, e^{i\widehat{\mathcal{S}}_{\rm eik}(\vec{r})}\, e^{i\vec{k}\cdot\vec{r}}\, \chi_{\frac{1}{2}m_s}\ , \tag{2.49}$$

with N a normalization factor. Inserting this expression into Eq. (2.48) yields a differential equation for the eikonal phase $\widehat{\mathcal{S}}_{\rm eik}(\vec{r})$, which is an operator in spin space. Defining the z axis along the direction of the average momentum $\vec{K}$, this eikonal phase can be written in the integral form ($\vec{r}\equiv(\vec{b},z)$)

$$i\,\widehat{\mathcal{S}}_{\rm eik}(\vec{b},z) = -i\,\frac{M_N}{K}\int_{-\infty}^{z} dz'\,\left\{V_c(\vec{b},z') + V_{so}(\vec{b},z')\,(\vec{\sigma}\cdot\vec{b}\times\vec{K} - iKz')\right\}\ . \tag{2.50}$$

In the relativistic eikonal limit, the scattering wave function takes on the form

$$\Psi^{(+)}_{\vec{k},m_s}(\vec{r}) = \sqrt{\frac{E+M_N}{2M_N}}\ \begin{bmatrix} 1 \\ \frac{1}{E+M_N+V_s(r)-V_v(r)}\vec{\sigma}\cdot\hat{\vec{p}} \end{bmatrix}\ e^{i\widehat{\mathcal{S}}_{\rm eik}(\vec{r})}\, e^{i\vec{k}\cdot\vec{r}}\,\chi_{\frac{1}{2}m_s}\ . \tag{2.51}$$

It is normalized such that it coincides with the relativistic plane wave (2.8) when $\vec{r}\to-\infty$. Eq. (2.51) differs from the plane-wave solutions in two respects. First, the lower component is dynamically enhanced due to the combination of the scalar and vector potentials $V_s - V_v < 0$. Second, the eikonal phase $e^{i\widehat{\mathcal{S}}_{\rm eik}(\vec{r})}$ describes the interactions of the nucleon with the nucleus via potential scattering. Furthermore, one can identify two primary relativistic effects: the Darwin term $V_{so}(\vec{b},z')\,(-iKz')$ in Eq. (2.50) and the previously mentioned dynamical enhancement of the lower component. The EA reproduces the exact partial-wave results well in intermediate-energy proton-nucleus scattering ($T_p \approx 500$ MeV) [70] and has also been successfully applied in $A(e,e'p)$ scattering [56,57,72–76].

The eikonal phase (2.50) is determined by performing a straight line integration along the direction of $\vec{K}$. A more accurate computation of the scattering wave function would be obtained by calculating its phase along the actual curved classical trajectory. Therefore, the use of the EA is only justified for small-angle scattering. Fortunately, high-energy proton-nucleus collisions like the soft IFSI in $A(p,pN)$ reactions are diffractive and extremely forward peaked.

The scattering wave function $\Psi^{(+)}_{\vec{k},m_s}(\vec{r})$ of Eq. (2.51) satisfies outgoing boundary conditions and can be used to describe the initial-state interactions (ISI) of the impinging proton. For the description of the final-state interactions (FSI), however, incoming boundary conditions are appropriate. According to standard distorted-wave theory [77], the corresponding wave function $\Psi^{(-)}_{\vec{k},m_s}(\vec{r})$ is related to $\Psi^{(+)}_{\vec{k},m_s}(\vec{r})$ by time reversal. Under time reversal, the following transformations occur:

$$\begin{array}{rcl} t & \rightarrow & -t\,, \\ \vec{r} & \rightarrow & \vec{r}\,, \\ \hat{\vec{p}} & \rightarrow & -\hat{\vec{p}}\,, \\ \vec{\sigma} & \rightarrow & -\vec{\sigma}\,, \\ \vec{L} & \rightarrow & -\vec{L}\,, \\ c & \rightarrow & c^*\,, \end{array} \tag{2.52}$$

where the last line indicates that all complex numbers are transformed into their complex conjugates. Thus, $\Psi^{(-)}_{\vec{k},m_s}(\vec{r})$ satisfies Eqs. (2.41)–(2.43) if the potentials $V_s(r)$, $V_v(r)$, $V_c(r)$, and $V_{so}(r)$ are replaced by their complex conjugates. The eikonal solution satisfying incoming boundary conditions then takes the form

$$\begin{aligned} \Psi^{(-)}_{\vec{k},m_s}(\vec{r}) \;=\; & \sqrt{\frac{E+M_N}{2M_N}} \left[\begin{array}{c} 1 \\ \frac{1}{E+M_N+V_s^*(r)-V_v^*(r)}\vec{\sigma}\cdot\hat{\vec{p}} \end{array} \right] \\ & \times \exp\left(i\,\frac{M_N}{K}\int_z^{+\infty} dz'\,\left\{ V_c^*(\vec{b},z') + V_{so}^*(\vec{b},z')\,(\vec{\sigma}\cdot\vec{b}\times\vec{K} - iKz') \right\} \right) \\ & \times \exp\left(i\vec{k}\cdot\vec{r} \right)\, \chi_{\frac{1}{2}m_s}\,, \end{aligned} \tag{2.53}$$

or, in the conjugate "bra" form in which the outgoing wave functions appear in the $A(p,2p)$ matrix element

$$\begin{aligned} \left(\Psi^{(-)}_{\vec{k},m_s}(\vec{r}) \right)^\dagger = & \sqrt{\frac{E+M_N}{2M_N}}\,\chi^\dagger_{\frac{1}{2}m_s}\,\exp\left(-i\vec{k}\cdot\vec{r}\right) \\ & \times \exp\left(-i\,\frac{M_N}{K}\int_z^{+\infty} dz'\,\left\{ V_c(\vec{b},z') + V_{so}(\vec{b},z')\,(\vec{\sigma}\cdot\vec{b}\times\vec{K} + iKz') \right\} \right) \\ & \times \left[\begin{array}{cc} 1 & -\vec{\sigma}\cdot\hat{\vec{p}}\frac{1}{E+M_N+V_s(r)-V_v(r)} \end{array} \right]\,. \end{aligned} \tag{2.54}$$

2.2.2 ROMEA for $A(p,pN)$ Reactions

In evaluating the IFSI effects in our $A(p,pN)$ calculations, some approximations are introduced. First, the dynamical enhancement of the lower components of the scattering wave functions (2.51) is neglected in our factorized approach, the so-called noSV approximation. For small momenta, the lower components play a minor role with respect to the upper ones, due to the factor $\hat{\vec{p}}/(E+M_N+V_s(r)-V_v(r))$; while at higher momenta, $V_s(r)-V_v(r)$ can be disregarded in comparison with $E+M_N$. As such, the effect of the dynamical enhancement is not expected to be important for the $A(p,pN)$ cross sections. Next, the average momentum $\vec{K}$ is approximated by the asymptotic momenta of the impinging and outgoing nucleons ($\vec{p}_1$, $\vec{k}_1$, and $\vec{k}_2$). This is allowed within the small-angle restriction of the EA. Further, in the calculation of the scattering states, the impulse operator $\hat{\vec{p}}$ is replaced by the asymptotic momenta of the nucleons. In literature, this is usually referred to as the effective momentum approximation (EMA), in which the momentum operators that appear in spinor-distortion operators are replaced by asymptotic kinematics [78]. As mentioned before, the spin-orbit potential V_{so} is also omitted.

As a result, the effects of the interactions of the incoming and outgoing nucleons with the residual nucleus are implemented in the distorted momentum-space wave function of Eq. (2.35) through the following phase factors:

$$\widehat{\mathcal{S}}_{p1}\left(\vec{r}\right) = e^{-i\,\frac{M_p}{p_1}\int_{-\infty}^{z_{p_1}} dz\, V_c(\vec{b}_{p_1},z)}\,, \tag{2.55a}$$

$$\widehat{\mathcal{S}}_{k1}\left(\vec{r}\right) = e^{-i\,\frac{M_p}{k_1}\int_{z_{k_1}}^{+\infty} dz'\, V_c(\vec{b}_{k_1},z')}\,, \tag{2.55b}$$

$$\widehat{\mathcal{S}}_{k2}\left(\vec{r}\right) = e^{-i\,\frac{M_N}{k_2}\int_{z_{k_2}}^{+\infty} dz''\, V_c(\vec{b}_{k_2},z'')}\,, \tag{2.55c}$$

with the z-axes of the different coordinate systems lying along the trajectories of the respective particles (z along the direction of the incoming proton $\vec{p}_1$, z' along the trajectory of the scattered proton $\vec{k}_1$, and z'' along the path of the ejected nucleon $\vec{k}_2$); and $(\vec{b}_{p_1},z_{p_1})$, $(\vec{b}_{k_1},z_{k_1})$, and $(\vec{b}_{k_2},z_{k_2})$ are the coordinates of the collision point $\vec{r}$ in the respective coordinate systems. The geometry of the $A(p,pN)$ scattering process is illustrated in Fig. 2.3. The integration limits guarantee that the incoming proton only undergoes ISI up to the point where the hard NN collision occurs, and the outgoing nucleons are only subject to FSI after this hard collision.

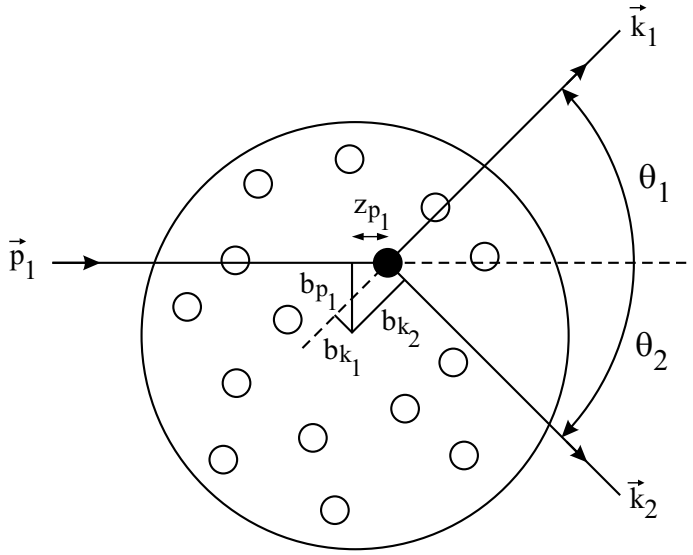

Figure 2.3 Geometry of the $A(p,pN)$ process. The vectors $\vec{b}_{p_1}$, $\vec{b}_{k_1}$, and $\vec{b}_{k_2}$ are the impact parameters for each of the three paths for a collision occurring at $\vec{r}$. z_{p_1}, z_{k_1}, and z_{k_2} are the z coordinates of the collision point in the respective coordinate systems. θ_1 and θ_2 are the angles of the outgoing nucleons relative to the incoming proton direction.

It is worth remarking that the eikonal IFSI operators of Eq. (2.55) are one-body operators, i.e., they do not depend on the coordinates $(\vec{r}_2, \vec{r}_3, \ldots, \vec{r}_A)$ of the residual nucleons. The normalization of the bound-state wave functions simplifies the IFSI factor (2.36) considerably to $\widehat{\mathcal{S}}_{\rm IFSI}(\vec{r}) = \widehat{\mathcal{S}}_{k1}\,(\vec{r})\;\widehat{\mathcal{S}}_{k2}\,(\vec{r})\;\widehat{\mathcal{S}}_{p1}\,(\vec{r})$ in the ROMEA case.

In the relativistic Hartree approximation, real potentials are used to calculate the bound-state wave functions. If the scattering states are derived using the same potentials, only elastic rescattering contributions are taken into account. In general, however, a fraction of the strength from the incident beam is removed from the elastic channel into unobserved inelastic ones like the production of an intermediate delta resonance or pion. This local absorption is commonly implemented by means of complex or optical potentials obtained by fitting nucleon-nucleus scattering data. In the numerical calculations, we employed the optical potential of van Oers *et al.* [9] to describe scattering off ^{4}He and the global $S-V$ parametrizations of Cooper *et al.* [46] for other target nuclei. Hereafter, the $A(p,2p)$ calculations which adopt Eq. (2.55) as a starting basis are labeled the relativistic optical model eikonal approximation (ROMEA).

2.3 Relativistic Multiple-Scattering Glauber Approximation

In the ROMEA approach, like in the DWIA approaches, all the IFSI effects are parametrized in terms of mean-field like optical potentials, i.e., the IFSI are seen as a scattering of the nucleon with the residual nucleus as a whole. As the energy increases, shorter distances are probed and the scattering with the individual nucleons becomes more relevant. For proton kinetic energies $T_p \geq 1$ GeV, the predominantly inelastic and diffractive character of the underlying elementary proton-nucleon scattering cross sections makes the Glauber approach [62–64] more natural. This method reestablishes the link between proton-nucleus interactions and the elementary proton-proton and proton-neutron scattering. It essentially relies on the eikonal, or, equivalently, the small-angle approximation and the assumption of consecutive cumulative scatterings of a fast nucleon on a composite target containing "frozen" point scatterers (nucleons).

In Glauber theory, the scattering wave function is related directly to the nucleon-nucleon elastic scattering data through the introduction of a profile function. This method has a long tradition of successful results in high-energy proton-nucleus elastic scattering ($T_p > 500$ MeV) [68, 79], and has also been shown to be reliable in describing $A(e,e'p)$ processes at high energies [57, 59, 80–88]. The relativistic Glauber formalism exposed here was originally developed to describe $A(e,e'p)$ observables [57, 59].

2.3.1 Nucleon-Nucleon Scattering

We start our derivations of a relativistic Glauber formalism by considering a nucleon-nucleon scattering process governed by a local Lorentz scalar and vector potential $V_s(r)$ and $V_v(r)$. In the EA, the scattering amplitude reads [70]

$$F_{m_s m'_s}(\vec{k}_i, \vec{k}_f, E) = -\frac{M_N}{2\pi} \left\langle \Psi^{(+)}_{\vec{k}_f, m'_s} \middle| (\beta V_s + V_v) \middle| \Phi_{\vec{k}_i, m_s} \right\rangle , \tag{2.56}$$

with $\Psi^{(+)}_{\vec{k}_f, m'_s}$ the relativistic scattered state of Eq. (2.51) and $\Phi_{\vec{k}_i, m_s}$ the free Dirac solution (2.8). Note that in this section, $V_s(r)$ and $V_v(r)$ represent nucleon-nucleon potentials; whereas in Section 2.2, the notation refers to nucleon-nucleus potentials. Some algebraic manipulations lead to the following form for the scattering ampli-

tude [70]

$$F_{m_s m_s'}(\vec{k}_i, \vec{k}_f, E) = \left\langle m_s' \left| \frac{iK}{2\pi} \int d\vec{b}\, e^{i\vec{\Delta}\cdot\vec{b}}\, \Gamma_{NN}(K, \vec{b}) \right| m_s \right\rangle \ , \tag{2.57}$$

where the profile function is defined as

$$\Gamma_{NN}(K, \vec{b}) = 1 - e^{i\chi(K,\vec{b})} \ , \tag{2.58}$$

with the phase-shift function given by

$$\chi(K, \vec{b}) = -\frac{M_N}{K} \int_{-\infty}^{\infty} dz \, \left\{ V_c(\vec{b}, z) + V_{so}(\vec{b}, z)\, (\vec{\sigma} \cdot \vec{b} \times \vec{K}) \right\} \ . \tag{2.59}$$

The Darwin term $V_{so}(\vec{b}, z')\,(-iKz)$ present in Eq. (2.50) does not contribute to the elastic scattering amplitude since it is an odd function of z.

In standard Glauber theory, knowledge about the NN interaction potentials $V_c(r)$ and $V_{so}(r)$ is not needed, since the phase-shift function $\chi(K, \vec{b})$ can be directly extracted from proton-proton and proton-neutron scattering data on the basis of Eq. (2.57). This procedure will be outlined in what follows.

Assuming parity conservation, time-reversal invariance, the Pauli principle, and isospin invariance, the most general form for the scattering amplitude in the NN c.m. frame can be written in terms of five invariant amplitudes [68, 89]

$$\begin{aligned} F(\vec{\Delta}) \ &= \ A(\vec{\Delta}) + B(\vec{\Delta})\, (\vec{\sigma}_1 + \vec{\sigma}_2) \cdot \hat{n} + C(\vec{\Delta})\, (\vec{\sigma}_1 \cdot \hat{n})\, (\vec{\sigma}_2 \cdot \hat{n}) \\ &\quad + D(\vec{\Delta})\, (\vec{\sigma}_1 \cdot \hat{m})\, (\vec{\sigma}_2 \cdot \hat{m}) + E(\vec{\Delta})\, (\vec{\sigma}_1 \cdot \hat{l})\, (\vec{\sigma}_2 \cdot \hat{l}) \ . \end{aligned} \tag{2.60}$$

The initial and final nucleon spin operators are denoted by $\vec{\sigma}_1$ and $\vec{\sigma}_2$, and $\hat{n} \equiv \frac{\vec{k}_i \times \vec{k}_f}{|\vec{k}_i \times \vec{k}_f|}$, $\hat{m} \equiv \frac{\vec{k}_i - \vec{k}_f}{|\vec{k}_i - \vec{k}_f|}$, and $\hat{l} \equiv \frac{\vec{k}_i + \vec{k}_f}{|\vec{k}_i + \vec{k}_f|}$. Here, $\vec{k}_i$ is the initial, $\vec{k}_f$ the final, and $\vec{\Delta}$ the transferred momentum. As such, the NN scattering amplitude consists of a central term, a spin-orbit term, and three other spin-dependent terms. In principle, the amplitudes A, B, C, D, and E can be determined through a complete phase-shift analysis of the NN scattering data. In practice, most analyses only include the central term of the NN amplitude, since the small-angle scattering of protons with momentum $k > 1$ GeV/c is assumed to be dominated by this spin-independent term. The spinless version of Glauber theory was very successful in the analysis of proton-nucleus cross-section data [62, 68, 90]. The surprising behavior of spin observables in NN scattering [91, 92], however, poses a real challenge. As of today, a quantitative understanding of the spin dependence of the NN interaction

above 1 GeV does not exist [93]. In this work, all results are obtained within the framework of spinless Glauber theory.

The central term of Eq. (2.60) is parametrized as

$$A(\vec{\Delta}) \equiv A(\vec{\Delta}=0)\,\exp\left(-\frac{\beta_{NN}^2\Delta^2}{2}\right)\,. \tag{2.61}$$

with β_{NN}^2 the slope parameter. This Gaussian parametrization is based on the diffractive pattern, with broad maxima and diffractive dips, observed in elastic NN collisions at GeV energies. Similar to Fraunhofer diffraction in optics, the diffraction phenomenon occurs when the wavelength of the projectile is short compared to the size of the interaction region. The differential cross section $d\sigma/dt$, with $t \equiv (k_f^\mu - k_i^\mu)^2$ the Mandelstam variable, is extremely forward peaked and drops exponentially over many orders. The slope parameter β_{NN}^2 describes the t dependence of the elastic NN differential cross section at forward angles:

$$\frac{d\sigma_{NN}^{\rm el}}{dt} \approx \left.\frac{d\sigma_{NN}^{\rm el}}{dt}\right|_{t=0} \exp\left(-\beta_{NN}^2\,|t|\right)\,. \tag{2.62}$$

Using the optical theorem $\mathrm{Im}\,F(\theta=0,\phi=0) = \frac{k\,\sigma_{\rm tot}}{4\pi}$, one finds

$$A(\vec{\Delta}) = \frac{k\,\sigma_{NN}^{\rm tot}}{4\pi}\,(\epsilon_{NN}+i)\,\exp\left(-\frac{\beta_{NN}^2\Delta^2}{2}\right)\,, \tag{2.63}$$

with ϵ_{NN} the ratio of the real to the imaginary part of the scattering amplitude.

The inverse Fourier transform of Eq. (2.57) brings about the following expression for the profile function:

$$\Gamma_{NN}\left(k,\vec{b}\right) = \frac{\sigma_{NN}^{\rm tot}(k)\,(1-i\epsilon_{NN}(k))}{4\pi\beta_{NN}^2(k)}\,\exp\left(-\frac{\vec{b}^2}{2\beta_{NN}^2(k)}\right)\,. \tag{2.64}$$

The profile function for central elastic NN scattering depends on the momentum k through three parameters: the total NN cross sections $\sigma_{NN}^{\rm tot}(k)$, the slope parameters $\beta_{NN}^2(k)$, and the ratios of the real to the imaginary part of the scattering amplitude $\epsilon_{NN}(k)$. These parameters can be determined directly from the elementary proton-proton and proton-neutron scattering data, and will be discussed in Section 2.3.4.

At lower energies, that part of the profile function proportional to $\epsilon_{NN}(k)$ is non-Gaussian and makes significant contributions to nuclear scattering. Rather

than Eq. (2.64), a parametrization in terms of the Arndt NN phases [12, 13] is appropriate at lower energies. For the Glauber calculations presented here, which address higher energies, the Gaussian-like real part of $\Gamma_{NN}\left(k,\vec{b}\right)$ is the dominant contributor, and the use of Eq. (2.64) is justified.

2.3.2 Glauber Multiple-Scattering Extension of the EA

Assuming that the sequential scatterings are independent, the eikonal method can easily be extended to multiple scattering. This constitutes the basis of Glauber theory [62–64]. The scattering off a composite system (the IFSI in $A(p,pN)$ reactions) is modeled as the scattering of a fast particle (the incident, scattered, or ejected nucleon) with the scattering centers of the composite system (the spectator nucleons in the residual nucleus). We assume that the fast particle's momentum is much larger than that of the spectator nucleons. Then, the particle undergoes a negligible deflection and its trajectory can be approximated by a straight line (this is the EA). In addition, because the time it takes the particle to traverse the nucleus is very small, the spectator nucleons can be approximated by fixed scattering centers (the so-called frozen approximation). As mentioned before, we adopt a spinless Glauber theory, i.e., the fast particle only interacts with the scatterers by means of two-body spin-independent interactions. Exchange effects between the fast particle and the spectator nucleons are neglected as well.

For a multiple-scattering event leading from an initial state $|i\rangle$ to a final state $|f\rangle$, the Glauber scattering amplitude reads

$$F_{\rm multi}(\vec{\Delta}) = \frac{iK}{2\pi}\int d\vec{b}\, e^{i\vec{\Delta}\cdot\vec{b}}\ \langle f|\, 1 - e^{i\chi_{\rm tot}(K,\vec{b},\vec{b}_2,\ldots,\vec{b}_A)}\,|i\rangle\ , \tag{2.65}$$

where the total Glauber phase-shift function

$$\chi_{\rm tot}(K,\vec{b},\vec{b}_2,\ldots,\vec{b}_A) = \sum_{j=2}^{A}\chi_j(K,\vec{b}-\vec{b}_j)\ , \tag{2.66}$$

is the sum of the phase shifts χ_j contributed by each of the spectator scatterers. Here, $\vec{b}$ denotes the impact parameter of the fast nucleon and $(\vec{b}_2,\vec{b}_3,\ldots,\vec{b}_A)$ those of the frozen spectator nucleons. The phase-shift additivity property of Eq. (2.66) is a direct result of the following assumptions: the one-dimensional nature of the relative motion and the neglect of three- and more-body forces, scatterer motion, and

longitudinal momentum transfer. Moreover, as Eq. (2.65) is based on the eikonal approximation, it is only valid when the energy transfer is small compared to the incident particle energy, i.e., for elastic and mildly inelastic collisions. Expression (2.65) does not apply to deeply inelastic collisions in which the nature of the particles is modified or the number of particles is altered during the collision.

Under the assumption of phase-shift additivity, the eikonal wave function of Eq. (2.51) can be generalized to many-body scattering. The scattering wave function for a fast nucleon with momentum k and spin state $\left|\frac{1}{2}m_s\right\rangle$ which scatters from $A-1$ residual nucleons reads

$$\Psi^{(+)}_{\vec{k},m_s}(\vec{r}) = \sqrt{\frac{E+M_N}{2M_N}} \begin{bmatrix} 1 \\ \frac{1}{E+M_N}\vec{\sigma}\cdot\hat{\vec{p}} \end{bmatrix} \widehat{\mathcal{S}}\, e^{i\vec{k}\cdot\vec{r}}\, \chi_{\frac{1}{2}m_s} \ , \tag{2.67}$$

where the operator $\widehat{\mathcal{S}}$ implements the subsequent collisions of the fast nucleon with the frozen spectator nucleons

$$\widehat{\mathcal{S}}\,(\vec{r},\vec{r}_2,\vec{r}_3,\ldots,\vec{r}_A) \equiv \prod_{j=2}^{A} e^{-i\frac{M_N}{K}\int_{-\infty}^{z} dz'\, V_c(\vec{b}-\vec{b}_j,z'-z_j)} \ . \tag{2.68}$$

As in the ROMEA framework, only the central spin-independent contribution $V_c(\vec{b},z)$ is retained, the impulse operator is replaced by the nucleon momentum, and the dynamical enhancement of the lower component has been neglected since $E+M_N \gg |V_s(r)-V_v(r)|$ for the high energies at which Glauber theory is applied. In this general form, the multiple-scattering wave function can not be directly related to the individual profile function for NN scattering (2.64).

The zero-range approximation along the scattering direction offers the possibility to express the multiple-scattering wave function in terms of the experimentally determined profile function, thereby avoiding the technical complications with respect to potential scattering. The zero-range approximation

$$V_c(\vec{b}-\vec{b}_j,z'-z_j) \simeq V_c^{\perp}(\vec{b}-\vec{b}_j)\,\delta(z'-z_j) \ , \tag{2.69}$$

amounts to neglecting the finite longitudinal dimension of the NN interaction region. After expanding expression (2.68) for $\widehat{\mathcal{S}}$ and adopting the zero-range approximation, one obtains

$$\widehat{\mathcal{S}} \simeq \prod_{j=2}^{A}\left(1 - i\,\frac{M_N}{K}\,V_c^{\perp}(\vec{b}-\vec{b}_j)\,\theta(z'-z_j)\right) \ . \tag{2.70}$$

Using the relation (2.58) between the profile function and the phase-shift function, a similar reasoning leads to

$$\Gamma_{NN}(K,\vec{b}) \simeq i\,\frac{M_N}{K}\,V_c^{\perp}(\vec{b})\ . \tag{2.71}$$

Finally, the Glauber operator becomes

$$\widehat{\mathcal{S}}\left(\vec{r},\vec{r}_2,\vec{r}_3,\ldots,\vec{r}_A\right) \equiv \prod_{j=2}^{A}\left[1-\Gamma_{NN}\left(K,\vec{b}-\vec{b}_j\right)\,\theta\left(z-z_j\right)\right]\ , \tag{2.72}$$

where the step function $\theta\left(z-z_j\right)$ ensures that the nucleon only interacts with other nucleons if they are localized in its forward propagation path.

2.3.3 RMSGA for $A(p,pN)$ Reactions

The Glauber operators in Eq. (2.36) take the forms

$$\widehat{\mathcal{S}}_{p1}\left(\vec{r},\vec{r}_2,\vec{r}_3,\ldots,\vec{r}_A\right) = \prod_{j=2}^{A}\left[1-\Gamma_{pN}\left(p_1,\vec{b}-\vec{b}_j\right)\,\theta\left(z-z_j\right)\right]\ , \tag{2.73a}$$

$$\widehat{\mathcal{S}}_{k1}\left(\vec{r},\vec{r}_2,\vec{r}_3,\ldots,\vec{r}_A\right) = \prod_{j=2}^{A}\left[1-\Gamma_{pN}\left(k_1,\vec{b}\,'-\vec{b}\,'_j\right)\,\theta\left(z'_j-z'\right)\right]\ , \tag{2.73b}$$

$$\widehat{\mathcal{S}}_{k2}\left(\vec{r},\vec{r}_2,\vec{r}_3,\ldots,\vec{r}_A\right) = \prod_{j=2}^{A}\left[1-\Gamma_{N_{k2}N}\left(k_2,\vec{b}\,''-\vec{b}\,''_j\right)\,\theta\left(z''_j-z''\right)\right]\ , \tag{2.73c}$$

where $N_{k2}=p\ (n)$ for $A(p,2p)$ ($A(p,pn)$) reactions. Further, $\vec{r}$ denotes the collision point and $(\vec{r}_2,\vec{r}_3,\ldots,\vec{r}_A)$ are the positions of the frozen spectator protons and neutrons in the target. The $(\vec{b},z)$, $(\vec{b}\,',z')$, and $(\vec{b}\,'',z'')$ coordinate systems are defined as in Section 2.2.2. The step functions guarantee that the incoming proton can only interact with those spectator nucleons it encounters before the hard collision and that the outgoing protons can only interact with the spectator nucleons they find in their forward propagation paths.

Contrary to ROMEA, the Glauber IFSI operators of Eq. (2.73) are genuine A-body operators, so the integration over the coordinates of the spectator nucleons in

Eq. (2.36) has to be carried out explicitly:

$$\begin{aligned}\widehat{\mathcal{S}}_{\mathrm{IFSI}}^{\mathrm{RMSGA}}\left(\vec{r}\right) &= \prod_{j=2}^{A}\Bigg\{\int d\vec{r}_j\,\left|\phi_{\alpha_j}\left(\vec{r}_j\right)\right|^2\left[1-\Gamma_{pN}\left(p_1,\vec{b}-\vec{b}_j\right)\,\theta\left(z-z_j\right)\right]\\ &\times\left[1-\Gamma_{pN}\left(k_1,\vec{b}\,'-\vec{b}\,'_j\right)\,\theta\left(z\,'_j-z\,'\right)\right]\\ &\times\left[1-\Gamma_{N_{k2}N}\left(k_2,\vec{b}\,''-\vec{b}\,''_j\right)\,\theta\left(z\,''_j-z\,''\right)\right]\Bigg\}\,. \qquad (2.74)\end{aligned}$$

This makes the numerical evaluation of the Glauber IFSI factor very challenging. Standard numerical integration techniques were adopted to evaluate the IFSI factor and no additional approximations, such as the commonly used thickness-function approximation, were introduced.

Henceforth, we refer to calculations based on Eq. (2.74) as the relativistic multiple-scattering Glauber approximation (RMSGA).

2.3.4 Glauber Parameters

In contrast to the DWIA and ROMEA models, all parameters entering the RMSGA model can be obtained directly from elementary nucleon-nucleon scattering experiments. When calculating the Glauber scattering wave function for a given momentum k, the following input is needed: the total nucleon-nucleon cross section $\sigma_{NN}^{\mathrm{tot}}$, the slope parameter β_{NN}^2, and the ratio of the real to the imaginary part of the scattering amplitude ϵ_{NN}. We obtain the proton-proton and proton-neutron parameters through interpolation of the database available from the Particle Data Group [94,95], while the neutron-neutron scattering parameters are assumed to be identical to the proton-proton ones because of isospin symmetry.

The measured total (σ^{tot}) and elastic (σ^{el}) cross sections for proton-proton and proton-neutron scattering are shown in Fig. 2.4. The nature of the NN interaction changes drastically in going from low to high energies. At proton momenta $p \leq 1$ GeV/c, the scattering of nucleons is completely elastic; while at higher momenta, the interaction becomes inelastic and absorptive, as new particles are produced. From 1 GeV/c upward, the total reaction cross section remains almost constant, even though the NN interaction leaves the elastic regime and becomes more and more inelastic.

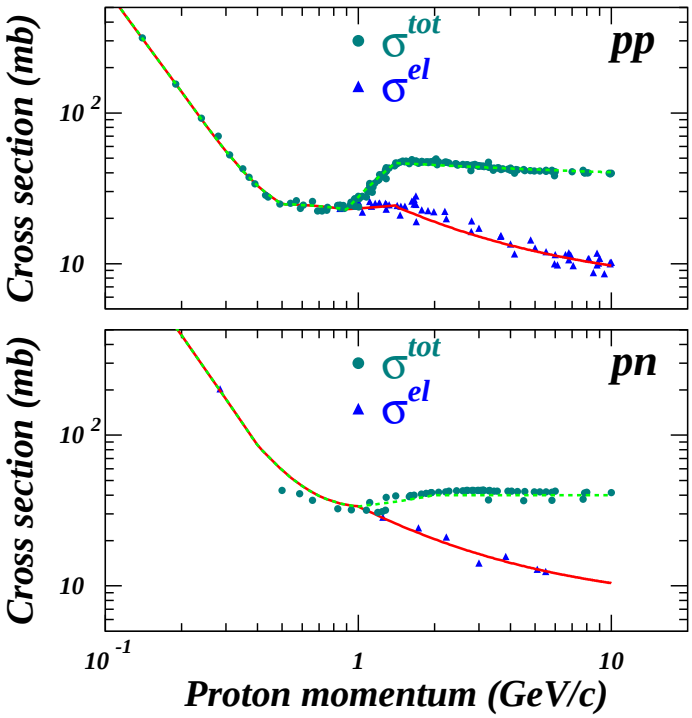

Figure 2.4 Total and elastic cross sections for proton-proton and proton-neutron scattering as a function of the proton lab momentum. The data were taken from Ref. [95]. The solid (dashed) curve is our global fit to the elastic (total) cross section.

The slope parameters β_{pp}^2 and β_{pn}^2 can be found by analyzing the t dependence of the differential cross sections with the aid of expression (2.62). Here, the spin-dependent terms are assumed to be negligible. For proton kinetic energies smaller than 1 GeV, the slope parameters extracted in this way differ significantly from the values found directly from experiment and phase-shift analysis. This can be attributed to a large contribution of the spin-dependent scattering amplitude [68]. At higher energies, this difference decreases quickly demonstrating that the spin terms are small. Below 1 GeV, values for the slope parameters obtained through Eq. (2.62) are scarce and not free of ambiguities due to spin effects. Therefore, in our

calculations, the slope parameters are determined through the following relation

$$\beta_{pN}^2 = \frac{\left(\sigma_{pN}^{\rm tot}\right)^2 \left(1+\epsilon_{pN}^2\right)}{16\pi\, \sigma_{pN}^{\rm el}} \ . \tag{2.75}$$

This parametrization can be derived from the theoretical shape of the elastic pN cross section as follows. Expression (2.63) for the elastic scattering amplitude leads to

$$\frac{d\sigma_{pN}^{\rm el}}{d(\Delta^2)} = \frac{\pi}{k^2}\, \left|A(\vec{\Delta})\right|^2 = \frac{\left(\sigma_{pN}^{\rm tot}\right)^2 \left(1+\epsilon_{pN}^2\right)}{16\pi}\, \exp\left(-\beta_{pN}^2 \Delta^2\right) \ . \tag{2.76}$$

Integrating this standard high-energy approximation of the elastic differential cross section results in

$$\sigma_{pN}^{\rm el} = \int \frac{d\sigma_{pN}^{\rm el}}{d(\Delta^2)}\, d(\Delta^2) = \frac{\left(\sigma_{pN}^{\rm tot}\right)^2 \left(1+\epsilon_{pN}^2\right)}{16\pi\beta_{pN}^2} \ , \tag{2.77}$$

so that the slope parameter is given by Eq. (2.75). In Fig. 2.5, the slope parameters obtained through this expression are compared with those determined directly through Eq. (2.62).

Fig. 2.6 displays the ratios of the real to the imaginary part of the scattering amplitude. In our formalism, global fits to the data are used. The ϵ_{pN} parameters can also be evaluated from dispersion relations, which provide a connection between the real and imaginary part of the scattering amplitude, in combination with the optical theorem. The dispersion-relation predictions for ϵ_{pp} and ϵ_{pn} [98, 99] are in good agreement with the experimental values.

2.4 Approximated RMSGA

In this section, the RMSGA IFSI factor of Eq. (2.74) is rewritten in a numerically more convenient form by adopting some approximations. First, the squared wave functions $\left|\phi_{\alpha_j}\left(\vec{r}_j\right)\right|^2$ of the spectator protons (neutrons) are replaced by $\rho_p\left(\vec{r}_j\right)/Z_{\rm res}$ ($\rho_n\left(\vec{r}_j\right)/N_{\rm res}$). Here, ρ_p and ρ_n are the proton and neutron density of the residual nucleus. $Z_{\rm res}$ and $N_{\rm res}$ are the number of protons and neutrons in the residual

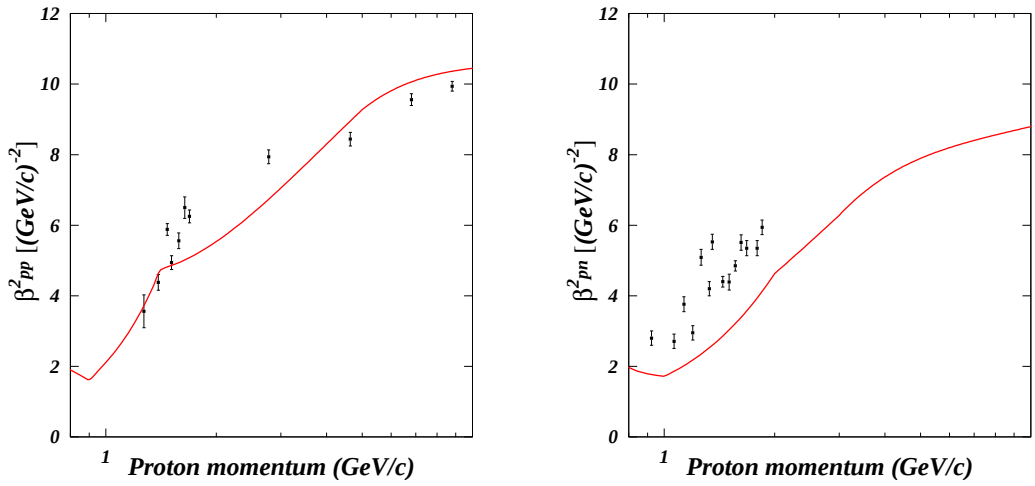

Figure 2.5 The slope parameters β_{pp}^2 and β_{pn}^2. The curves are obtained with Eq. (2.75) and the global fits to $\sigma_{pN}^{\rm tot}$, $\sigma_{pN}^{\rm el}$, and ϵ_{pN} shown in Figs. 2.4 and 2.6. The data are from Refs. [96] (proton-proton) and [97] (proton-neutron) and were determined through the small-angle t dependence (2.62) of the measured differential cross sections.

nucleus. This leaves us with

$$
\begin{aligned}
&\widehat{\mathcal{S}}_{\rm IFSI}^{\rm RMSGA}\left(\vec{r}\right) \simeq \\
&\quad\left\{\int d\vec{r}_j\,\frac{\rho_p\left(\vec{r}_j\right)}{Z_{\rm res}}\,\left[1-\Gamma_{pp}\left(p_1,\vec{b}-\vec{b}_j\right)\,\theta\left(z-z_j\right)\right]\left[1-\Gamma_{pp}\left(k_1,\vec{b}\,'-\vec{b}\,'_j\right)\,\theta\left(z'_j-z'\right)\right]\right. \\
&\qquad\left.\times\left[1-\Gamma_{N_{k2}p}\left(k_2,\vec{b}\,''-\vec{b}\,''_j\right)\,\theta\left(z''_j-z''\right)\right]\right\}^{Z_{\rm res}} \\
&\times\left\{\int d\vec{r}_j\,\frac{\rho_n\left(\vec{r}_j\right)}{N_{\rm res}}\,\left[1-\Gamma_{pn}\left(p_1,\vec{b}-\vec{b}_j\right)\,\theta\left(z-z_j\right)\right]\left[1-\Gamma_{pn}\left(k_1,\vec{b}\,'-\vec{b}\,'_j\right)\,\theta\left(z'_j-z'\right)\right]\right. \\
&\qquad\left.\times\left[1-\Gamma_{N_{k2}n}\left(k_2,\vec{b}\,''-\vec{b}\,''_j\right)\,\theta\left(z''_j-z''\right)\right]\right\}^{N_{\rm res}}\,. \qquad (2.78)
\end{aligned}
$$

Second, one assumes that the proton and neutron densities are slowly varying functions of $\vec{b}$, while $\Gamma_{NN}\left(k,\vec{b}-\vec{b}_j\right)$ is sharply peaked at $\vec{b}-\vec{b}_j=\vec{0}$. Under this assump-

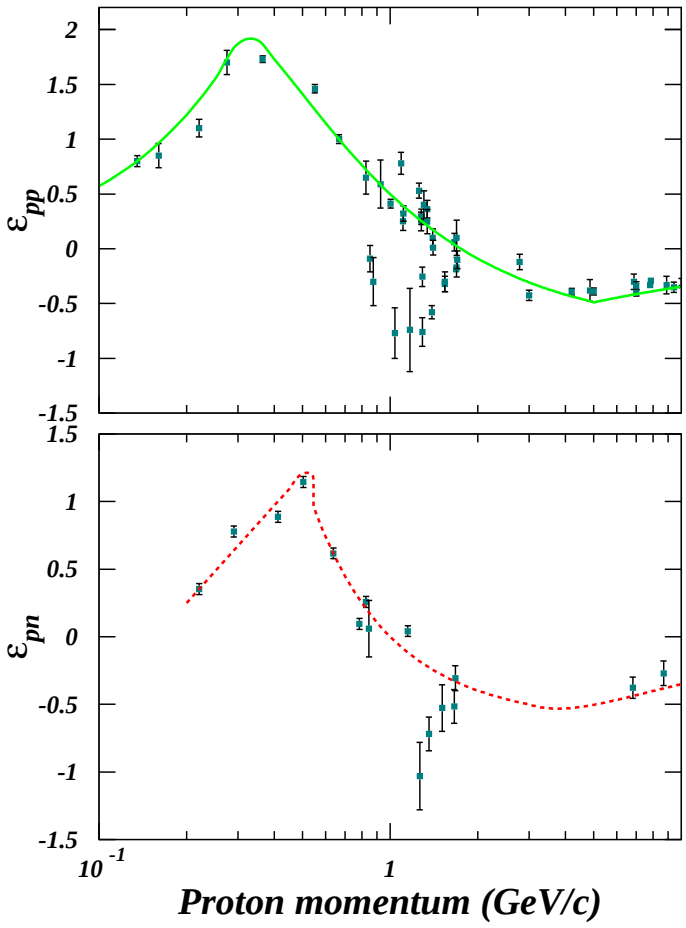

Figure 2.6 The ratios of the real to the imaginary part of the central scattering amplitude $A(\Delta)$ for proton-proton and proton-neutron scattering as a function of the proton lab momentum. The curves are global fits to the data. The data are from Ref. [68].

tion, one can make the following approximation

$$\begin{aligned}
&\int d\vec{r}_j\, \rho_N\left(\vec{r}_j\right)\, \Gamma_{pN}\left(p_1, \vec{b}-\vec{b}_j\right)\, \theta\left(z-z_j\right) \\
&= \frac{\sigma_{pN}^{\mathrm{tot}}\left(p_1\right)\left(1-i\epsilon_{pN}\left(p_1\right)\right)}{4\pi\, \beta_{pN}^2\left(p_1\right)} \int_{-\infty}^{z} dz_j\, \rho_N\left(\vec{b}, z_j\right) \int d\vec{b}_j\, \exp\left(-\frac{(\vec{b}-\vec{b}_j)^2}{2\beta_{pN}^2\left(p_1\right)}\right) \\
&\simeq \frac{1}{2}\, \sigma_{pN}^{\mathrm{tot}}\left(p_1\right)\left(1-i\epsilon_{pN}\left(p_1\right)\right) \int_{-\infty}^{z} dz_j\, \rho_N\left(\vec{b}, z_j\right)\ , \qquad (2.79)
\end{aligned}$$

and a similar approximation for the terms linear in $\Gamma_{pN}\left(k_1, \vec{b}\,' - \vec{b}\,'_j\right)$ and $\Gamma_{N_{k2}N}\left(k_2, \vec{b}\,'' - \vec{b}\,''_j\right)$, while higher-order terms are neglected. Inserting this in Eq. (2.78) yields

$$\begin{aligned}
&\widehat{\mathcal{S}}^{\mathrm{RMSGA}'}_{\mathrm{IFSI}}(\vec{r}) = \\
&\quad\left\{1 - \frac{\sigma^{\mathrm{tot}}_{pp}(p_1)\,(1 - i\epsilon_{pp}(p_1))}{2Z_{\mathrm{res}}} \int_{-\infty}^{z} dz_j\, \rho_p\left(\vec{b}, z_j\right)\right. \\
&\qquad - \frac{\sigma^{\mathrm{tot}}_{pp}(k_1)\,(1 - i\epsilon_{pp}(k_1))}{2Z_{\mathrm{res}}} \int_{z'}^{+\infty} dz'_j\, \rho_p\left(\vec{b}\,', z'_j\right) \\
&\qquad \left. - \frac{\sigma^{\mathrm{tot}}_{N_{k2}p}(k_2)\,(1 - i\epsilon_{N_{k2}p}(k_2))}{2Z_{\mathrm{res}}} \int_{z''}^{+\infty} dz''_j\, \rho_p\left(\vec{b}\,'', z''_j\right)\right\}^{Z_{\mathrm{res}}} \\
&\qquad \times \text{ factor for the spectator neutrons .}
\end{aligned} \tag{2.80}$$

In the more frequently adopted exponential form, this reads [55, 100]

$$\begin{aligned}
\widehat{\mathcal{S}}^{\mathrm{RMSGA}'}_{\mathrm{IFSI}}(\vec{r}) \;=\; &\prod_{N=p,n} e^{-\frac{1}{2}\,\sigma^{\mathrm{tot}}_{pN}(p_1)\,(1-i\epsilon_{pN}(p_1))\,\int_{-\infty}^{z} dz_j\,\rho_N(\vec{b},z_j)} \\
&\times e^{-\frac{1}{2}\,\sigma^{\mathrm{tot}}_{pN}(k_1)\,(1-i\epsilon_{pN}(k_1))\,\int_{z'}^{+\infty} dz'_j\,\rho_N(\vec{b}\,',z'_j)} \\
&\times e^{-\frac{1}{2}\,\sigma^{\mathrm{tot}}_{N_{k2}N}(k_2)\,(1-i\epsilon_{N_{k2}N}(k_2))\,\int_{z''}^{+\infty} dz''_j\,\rho_N(\vec{b}\,'',z''_j)} \;.
\end{aligned} \tag{2.81}$$

The IFSI operator of Eq. (2.74) can thus be reduced to a one-body operator. Henceforth, calculations based on Eq. (2.81) are labeled as RMSGA′.

2.5 Second-Order Eikonal Corrections

Because of its numerous advantages, the eikonal approximation has a long history of successful results in describing $A(p, pN)$ reactions as well as other scattering processes like heavy-ion collisions, photo- and electro-induced nucleon-knockout reactions. The eikonal scattering wave functions are derived by linearizing the continuum wave equation for the interacting particle. Hence, the solution is only valid to first order in $1/k$, with k the particle's momentum, and the EA is suited for the description of high-energy scattering. To extend the applicability to lower energies, Wallace [101–105] has developed systematic corrections to the eikonal scattering amplitude. Several authors have investigated the effect of higher-order

eikonal corrections in elastic nuclear scattering by protons, antiprotons, and α particles [106,107], heavy-ion scattering [108–111], and inclusive electron-nucleus scattering [112]. In this section, we develop a second-order correction to the ROMEA framework of Section 2.2. Our formalism builds upon the work of Baker [113], where an eikonal approximation for potential scattering was derived to second order in $1/k$. This approach is extended to account for the effect of the spin-orbit potential.

Like in the ROMEA approach of Section 2.2, the starting point is the Schrödinger-like equation (2.42) for the upper component $u^{(+)}_{\vec{k},m_s}(\vec{r})$. In the spin-orbit ($V_{so}(r)\,\vec{\sigma}\cdot\vec{L}$) and Darwin ($V_{so}(r)\,(-i\vec{r}\cdot\hat{\vec{p}})$) terms, as well as in the lower component (2.43), the momentum operator $\hat{\vec{p}}$ is replaced by the asymptotic momentum $\vec{k}$, i.e., the EMA is adopted. For the upper component, one postulates a solution of the form

$$u^{(+)}_{\vec{k},m_s}(\vec{r}) \equiv N\,\eta(\vec{r})\,e^{i\vec{k}\cdot\vec{r}}\,\chi_{\frac{1}{2}m_s}\ , \tag{2.82}$$

i.e., a plane wave modulated by an eikonal factor $\eta(\vec{r})$. Here, N is a normalization factor.

In the ROMEA approach, which adopts the first-order eikonal approximation, the Schrödinger-type equation (2.42) was then linearized in $\hat{\vec{p}}$ leading to the solution (2.50). Despite the fact that it is retained as an exponential phase, this solution is, strictly speaking, only valid up to first order in $V_{\rm opt}/k$, with $V_{\rm opt}(\vec{b},z) = V_c(\vec{b},z) + V_{so}(\vec{b},z)\,(\vec{\sigma}\cdot\vec{b}\times\vec{k} - ikz)$. Mathematically, the exponential expression is not justified. However, it is commonly used because physical intuition dictates that the effect of the scattering is to modulate the incoming plane wave by a phase change.

In what follows, we will derive an expression for the eikonal factor $\eta(\vec{r})$ that is valid up to order $V_{\rm opt}/k^2$. The momentum dependence in the spin-orbit and Darwin terms makes that these terms are retained up to order V_{so}/k, while central terms are included up to order V_c/k^2. Note that the expansion is not expressed in terms of the Lorentz scalar and vector potentials V_s and V_v. Looking for a solution of the form (2.82) for the Schrödinger-like equation (2.42), Baker arrived at the following equation for the eikonal factor (see Eq. (14) of Ref. [113]):

$$\begin{aligned}\eta(\vec{b},z) = 1 &- \frac{i}{v}\int_{-\infty}^{z} dz'\,V_{\rm opt}(\vec{b},z')\,\eta(\vec{b},z') + \frac{1}{2kv}\,V_{\rm opt}(\vec{b},z)\,\eta(\vec{b},z) \\ &+ \frac{1}{2kv}\int_{-\infty}^{z} dz'\,(z-z')\,\left(\frac{1}{b}+\frac{\partial}{\partial b}\right)\frac{\partial}{\partial b}\,\Big(V_{\rm opt}(\vec{b},z')\,\eta(\vec{b},z')\Big)\ ,\end{aligned} \tag{2.83}$$

where $v = k/M_N$. Note that, apart from dropping contributions of order $V_{\rm opt}/k^3$ and higher, no additional assumptions were made when deriving Eq. (2.83). In Ref. [113], Eq. (2.83) was subsequently solved for spherically symmetric potentials. The spin-orbit and Darwin terms, however, break the spherical symmetry and a novel method to solve Eq. (2.83) is required.

To that purpose, we assume that the derivative of the function η is of higher order in $1/k$ than η itself (as is true for the ROMEA solution (2.50)). This allows us to drop the $\partial\eta/\partial b$ contribution in the last term of the right-hand side of Eq. (2.83) since it is of order $V_{\rm opt}/k^3$ or higher:

$$\begin{aligned}
&\frac{1}{2kv}\int_{-\infty}^{z} dz'\,(z-z')\,\left(\frac{1}{b}+\frac{\partial}{\partial b}\right)\frac{\partial}{\partial b}\,\Big(V_{\rm opt}(\vec{b},z')\,\eta(\vec{b},z')\Big)\\
&\quad = \frac{1}{2kv}\left(\frac{1}{b}+\frac{\partial}{\partial b}\right)\int_{-\infty}^{z} dz'\,(z-z')\\
&\qquad \times\left[\frac{\partial}{\partial b}\,\Big(V_c(\vec{b},z')+V_{so}(\vec{b},z')\,(\vec{\sigma}\cdot\vec{b}\times\vec{k}-ikz')\Big)\right]\eta(\vec{b},z')\;. \qquad (2.84)
\end{aligned}$$

Spherical symmetry implies that $z'\,\partial V_c(\vec{b},z')/\partial b = b\,\partial V_c(\vec{b},z')/\partial z'$. Hence, the $z'\,\partial V_c/\partial b$ term in Eq. (2.84) can be written as

$$\begin{aligned}
&-\frac{1}{2kv}\left(\frac{1}{b}+\frac{\partial}{\partial b}\right)\int_{-\infty}^{z} dz'\,b\,\frac{\partial V_c(\vec{b},z')}{\partial z'}\,\eta(\vec{b},z')\\
&\quad = -\frac{1}{2kv}\left(\frac{1}{b}+\frac{\partial}{\partial b}\right)\int_{-\infty}^{z} dz'\,b\,\frac{\partial}{\partial z'}\,\Big(V_c(\vec{b},z')\,\eta(\vec{b},z')\Big)\\
&\quad = -\frac{1}{2kv}\left[\left(2+b\frac{\partial}{\partial b}\right)\,V_c(\vec{b},z)\right]\eta(\vec{b},z)\;. \qquad (2.85)
\end{aligned}$$

In the first step, the fact that the derivative $\partial\eta/\partial z'$ is of higher order was used to turn the integrand into an exact differential. A similar reasoning, followed by integration by parts, leads to

$$\begin{aligned}
&\frac{1}{2kv}\left(\frac{1}{b}+\frac{\partial}{\partial b}\right)\int_{-\infty}^{z} dz'\,(z-z')\,\frac{\partial V_{so}(\vec{b},z')}{\partial b}\,(-ikz')\,\eta(\vec{b},z')\\
&\quad = -\frac{i}{2v}\int_{-\infty}^{z} dz'\left[\left(2+b\frac{\partial}{\partial b}\right)\,V_{so}(\vec{b},z)\right]\eta(\vec{b},z')\;, \qquad (2.86)
\end{aligned}$$

for the Darwin term of Eq. (2.84). As a result, Eq. (2.83) takes the form

$$\begin{aligned}
\eta(\vec{b},z) = & \\
& 1 - \frac{i}{v}\int_{-\infty}^{z} dz'\, V_{\rm opt}(\vec{b},z')\,\eta(\vec{b},z') - \frac{1}{2kv}\left[\left(1+b\frac{\partial}{\partial b}\right)\, V_c(\vec{b},z)\right]\eta(\vec{b},z) \\
& + \frac{z}{2kvb}\left(1+b\frac{\partial}{\partial b}\right)\int_{-\infty}^{z} dz'\,\frac{\partial V_c(\vec{b},z')}{\partial b}\,\eta(\vec{b},z') \\
& + \frac{1}{2kv}\,V_{so}(\vec{b},z)\,(\vec{\sigma}\cdot\vec{b}\times\vec{k} - ikz)\,\eta(\vec{b},z) \\
& + \frac{1}{2kvb}\left(1+b\frac{\partial}{\partial b}\right)\int_{-\infty}^{z} dz'\,(z-z')\left[\frac{\partial}{\partial b}\,\left(V_{so}(\vec{b},z')\,\vec{\sigma}\cdot\vec{b}\times\vec{k}\right)\right]\eta(\vec{b},z') \\
& - \frac{i}{2v}\int_{-\infty}^{z} dz'\left[\left(2+b\frac{\partial}{\partial b}\right)\, V_{so}(\vec{b},z)\right]\eta(\vec{b},z')\ . \qquad (2.87)
\end{aligned}$$

We look for a solution of the form

$$\begin{aligned}
\eta(\vec{b},z) &= f(\vec{b},z)\,\exp\left(-\frac{i}{v}\int_{-\infty}^{z} d\bar{z}\,V_{\rm opt}(\vec{b},\bar{z})\,f(\vec{b},\bar{z})\right) \\
&= f(\vec{b},z)\,\exp\left(i\,S(\vec{b},z)\right)\ , \qquad (2.88)
\end{aligned}$$

which reduces to the ROMEA result of Eq. (2.50) when terms of higher order than $V_{\rm opt}/k$ are neglected. Accordingly, the function $f(\vec{b},z)$ should be of the form $f = 1 + O(V_{\rm opt}/k^2)$. Substituting (2.88) into Eq. (2.87) and multiplying by $e^{-i\,S(\vec{b},z)}$ on the right yields

$$\begin{aligned}
f(\vec{b},z) = 1 & - \frac{1}{2kv}\left[\left(1+b\frac{\partial}{\partial b}\right)\, V_c(\vec{b},z)\right] f(\vec{b},z) \\
& + \frac{z}{2kvb}\left(1+b\frac{\partial}{\partial b}\right)\int_{-\infty}^{z} dz'\,\frac{\partial V_c(\vec{b},z')}{\partial b}\,f(\vec{b},z') \\
& + \frac{1}{2kv}\,V_{so}(\vec{b},z)\,(\vec{\sigma}\cdot\vec{b}\times\vec{k} - ikz)\,f(\vec{b},z) \\
& + \frac{1}{2kvb}\left(1+b\frac{\partial}{\partial b}\right)\int_{-\infty}^{z} dz'\,(z-z')\left[\frac{\partial}{\partial b}\,\left(V_{so}(\vec{b},z')\,\vec{\sigma}\cdot\vec{b}\times\vec{k}\right)\right] f(\vec{b},z') \\
& - \frac{i}{2v}\int_{-\infty}^{z} dz'\left[\left(2+b\frac{\partial}{\partial b}\right)\, V_{so}(\vec{b},z)\right] f(\vec{b},z')\ . \qquad (2.89)
\end{aligned}$$

In deriving this equation, we set $e^{i\,S(\vec{b},z')}\,e^{-i\,S(\vec{b},z)}$ equal to 1, since higher-order terms are neglected. The difficulty in solving for $f(\vec{b},z)$ is that Eq. (2.89) is an integral equation. An expression for $f(\vec{b},z)$ can, however, be readily obtained by

adding $(1-f)$ terms, which introduce only higher-order terms, to the right-hand side of Eq. (2.89). This is permitted since the solution is only determined up to order $V_{\rm opt}/k^2$. With this manipulation, the function f becomes

$$\begin{aligned} f(\vec{b},z) = 1 &- \frac{1}{2kv}\left(1+b\frac{\partial}{\partial b}\right) V_c(\vec{b},z) + \frac{z}{2kvb}\left(1+b\frac{\partial}{\partial b}\right)\int_{-\infty}^{z} dz'\,\frac{\partial V_c(\vec{b},z')}{\partial b} \\ &+ \frac{1}{2kv}\,V_{so}(\vec{b},z)\,(\vec{\sigma}\cdot\vec{b}\times\vec{k} - ikz) \\ &+ \frac{1}{2kvb}\left(1+b\frac{\partial}{\partial b}\right)\int_{-\infty}^{z} dz'\,(z-z')\,\frac{\partial}{\partial b}\,\left(V_{so}(\vec{b},z')\,\vec{\sigma}\cdot\vec{b}\times\vec{k}\right) \\ &- \frac{i}{2v}\int_{-\infty}^{z} dz'\,\left(2+b\frac{\partial}{\partial b}\right)\,V_{so}(\vec{b},z)\ . \end{aligned} \tag{2.90}$$

The eikonal factor of Eq. (2.88) whereby f is determined by (2.90) is a solution of the integral equation (2.83) to order $V_{\rm opt}/k^2$ and indeed reduces to the ROMEA result (2.50) when truncated at order $V_{\rm opt}/k$. Furthermore, it can be easily verified that the derivative of η is of higher order in $V_{\rm opt}/k$ than η itself. Henceforth, results obtained with the eikonal factor given by Eqs. (2.88) and (2.90) are dubbed as the second-order relativistic optical model eikonal approximation (SOROMEA).

Chapter 3

Initial- and Final-State Interactions and $A(p, pN)$ Differential Cross Sections

In the previous chapter, we have developed a cross-section factorized framework for describing $A(p, pN)$ processes and have discussed various methods to treat the IFSI. In this chapter, we will put our framework to a stringent test by comparing our calculations with exclusive $A(p, pN)$ cross-section data that have been collected at various facilities. The main focus is on the optical-potential approach, as this method turns out to be the most suitable for the description of the IFSI for the kinematical settings of the experiments discussed in this chapter.

Section 3.1 is devoted to a presentation of optical-potential and Glauber results for the IFSI factor. This is a function which accounts for all IFSI effects when computing the $A(p, pN)$ observables. In Section 3.2, the radial and polar-angle contributions to the $A(p, pN)$ cross sections are studied. Finally, in Section 3.3, the optical-potential predictions of our model are compared with cross-section data that have been collected at the Petersburg Nuclear Physics Institute (PNPI), the Enrico Fermi Institute (EFI), and the Tri-University Meson Facility (TRIUMF). First, we present our calculations for the ^{12}C, ^{16}O, and ^{40}Ca$(p, 2p)$ and (p, pn) PNPI data for 1 GeV incoming proton energies [114]. Second, the results from the ^{40}Ca$(p, 2p)$ experiment performed at EFI [115], one of the first of its kind, are scrutinized. Finally, our predictions for scattering off ^{16}O and ^{4}He are compared to the TRIUMF data of

McDonald [116], Kitching [8], and van Oers [9].

Most results presented in this chapter were originally published in [117].

3.1 Numerical Results for the IFSI Factor

In this section, results for the IFSI factor (2.36) are given for the knockout of nucleons from the Fermi level in ^{12}C, ^{16}O, and ^{40}Ca, at an incident energy $T_{p1} = 1$ GeV and a scattered proton kinetic energy $T_{k1} = 870$ MeV. Thereby, we adopt coplanar scattering angles $(\theta_1, \theta_2) = (13.4^\circ, 67^\circ)$ on opposite sides of the incident beam, i.e., kinematics corresponding with the PNPI experiment of Ref. [114]. All IFSI effects are included in the IFSI factor $\mathcal{S}_{\rm IFSI}(\vec{r})$. Note that in the absence of initial- and final-state interactions the real part of the IFSI factor equals one, whereas the imaginary part vanishes identically.

The $A(p,pN)$ IFSI factor is a function of three independent variables (r, θ, ϕ). The z axis is chosen along the direction of the incoming beam $\vec{p}_1$, the y axis lies along $\vec{p}_1 \times \vec{k}_1$, and the x axis lies in the scattering plane defined by the proton momenta $\vec{p}_1$ and $\vec{k}_1$. θ and ϕ denote the polar and azimuthal angles with respect to the z axis and the x axis, respectively. The radial coordinate r represents the distance relative to the center of the target nucleus.

3.1.1 Polar-Angle Dependence

To gain a better insight into the dependence of the IFSI factor on r, θ, and ϕ, we calculated the contribution of the three distorting functions $\widehat{\mathcal{S}}_{p1}$, $\widehat{\mathcal{S}}_{k1}$, and $\widehat{\mathcal{S}}_{k2}$ to the IFSI factor. In Figs. 3.1 and 3.2 results are displayed for the computed real and imaginary part of $\mathcal{S}_{\rm IFSI}(r, \theta, \phi = 0)$ for proton emission from the Fermi level in ^{12}C. The results were computed within the ROMEA framework, using the EDAD1 optical-potential parametrization of [46].

The θ dependence can be interpreted as follows. For a given r, the distance that the incoming proton travels through the target nucleus before colliding hard with a target nucleon decreases with increasing angle θ. As a consequence, small values of θ induce the largest ISI. For the FSI of the scattered proton, the opposite holds true, and $\theta = 180^\circ$ for a large r value corresponds to an event whereby the hard collision transpires at the outskirts of the nucleus and the scattered proton has to

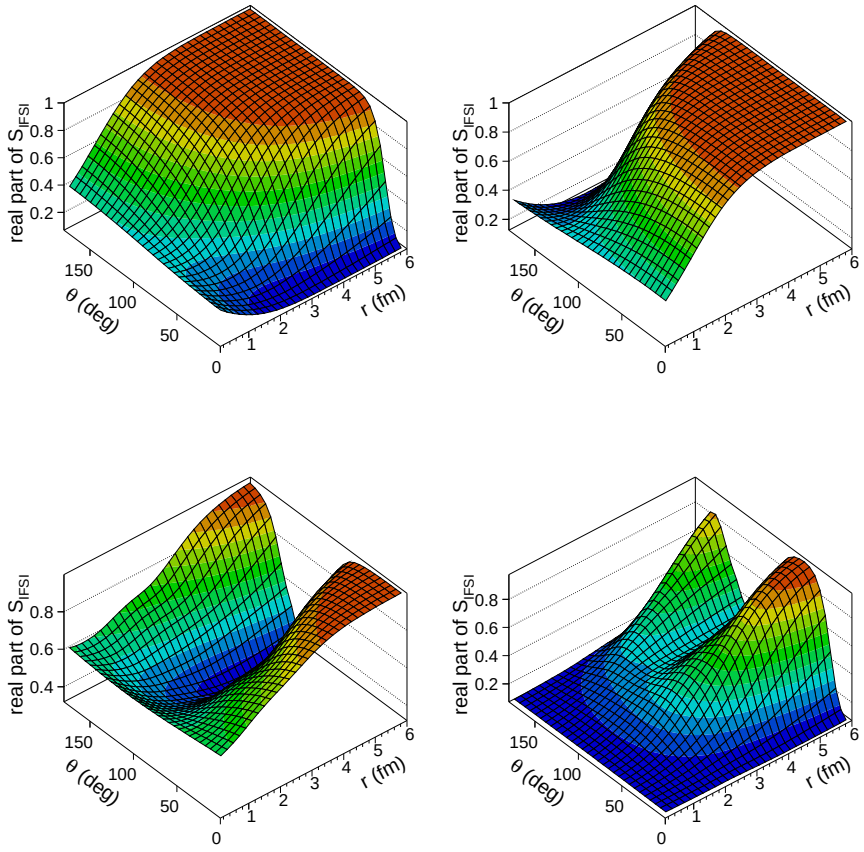

Figure 3.1 The radial and polar-angle dependence of the real part of the IFSI factor $\mathcal{S}_{\rm IFSI}$ in the scattering plane ($\phi = 0°$) for proton knockout from the Fermi level in ^{12}C. The upper left panel is the contribution from the impinging proton ($\widehat{\mathcal{S}}_{p1}$), while the upper right panel shows the effect of the FSI of the scattered proton ($\widehat{\mathcal{S}}_{k1}$). In the bottom left figure, the effect of the FSI of the ejected proton ($\widehat{\mathcal{S}}_{k2}$) is presented and the bottom right figure shows the complete IFSI factor ($\widehat{\mathcal{S}}_{k1}\ \widehat{\mathcal{S}}_{k2}\ \widehat{\mathcal{S}}_{p1}$). The kinematics was $T_{p1} = 1$ GeV, $T_{k1} = 870$ MeV, $\theta_1 = 13.4°$, and $\theta_2 = 67°$.

travel through the whole nucleus before it becomes asymptotically free, thus giving rise to the smallest (largest) values for the real (imaginary) part of the IFSI factor. Unlike the scattered proton, which moves almost collinear to the z axis, the ejected nucleon leaves the nucleus under a large scattering angle θ_2. Hence, the FSI are minimal for θ close to $0°$ or $180°$ and maximal for θ around $180° - \theta_2$. Finally, the

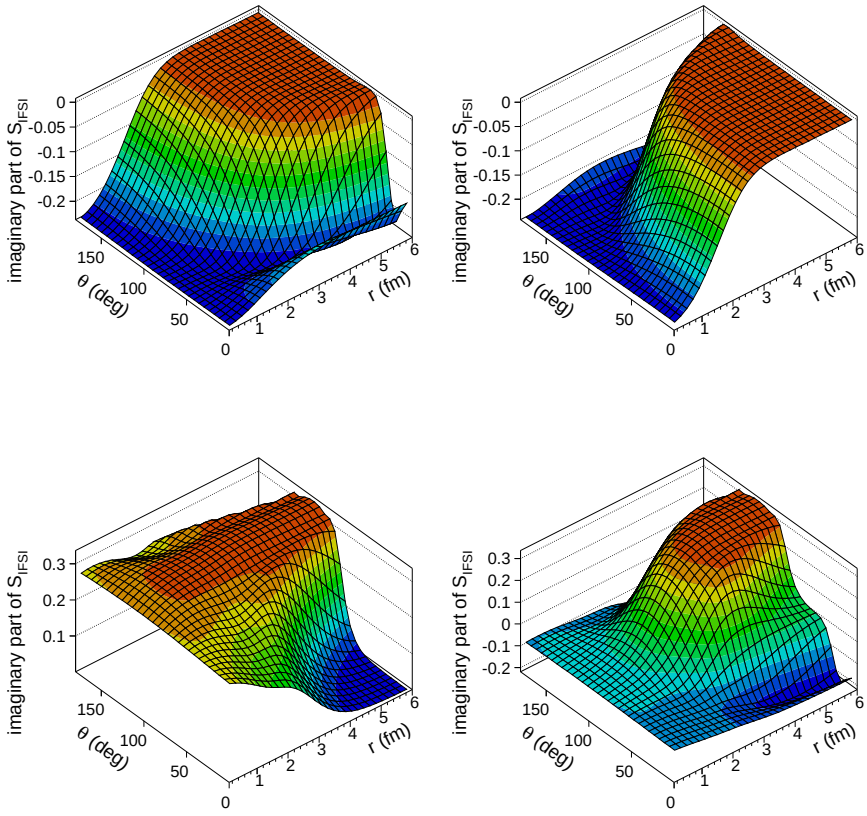

Figure 3.2 As in Fig. 3.1, but for the imaginary part of the IFSI factor.

θ dependence of the complete IFSI factor is the result of the interplay between the three distorting effects, with the strongest scattering and absorption observed at θ close to 0°, $180^\circ - \theta_2$, and 180°.

3.1.2 Radial Dependence

Fig. 3.3 displays the real part of the ^{40}Ca IFSI factor as a function of r at various values of θ. The ROMEA calculations were performed for the same kinematics as in Figs. 3.1 and 3.2, and employed the EDAI optical-potential fit of [46].

The upper left panel suggest that the ISI effects increase with growing r for $\theta = 0^\circ$. For $\theta = 45^\circ$ and increasing r, initially, the growing distance the proton

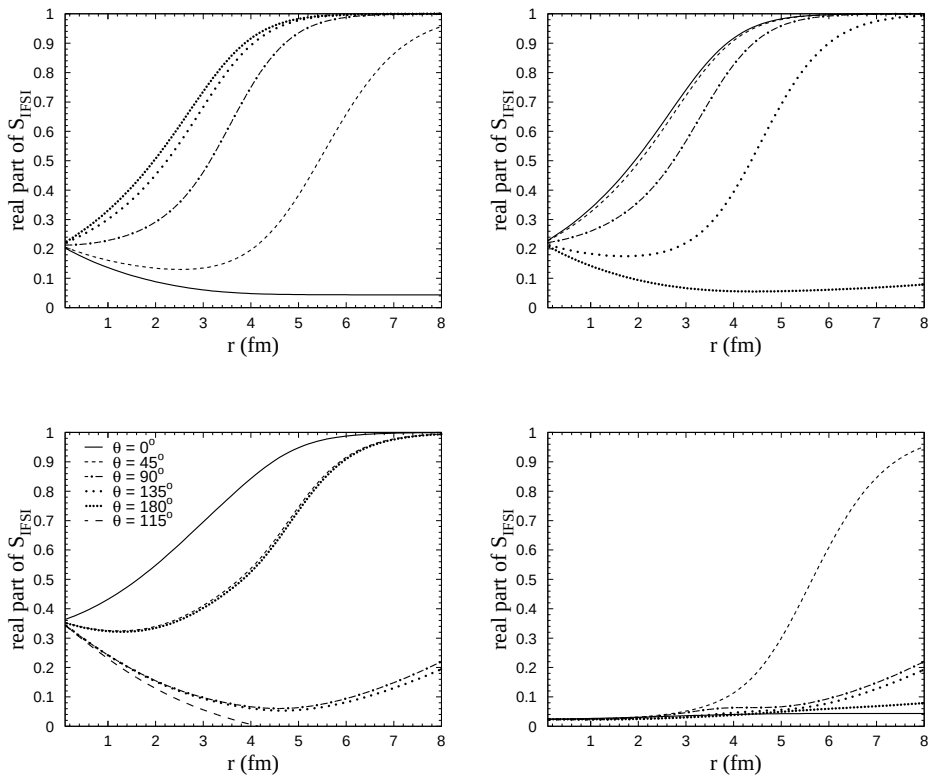

Figure 3.3 The radial dependence of the real part of the IFSI factor $\mathcal{S}_{\rm IFSI}$ in the scattering plane ($\phi = 0°$) for neutron knockout from the Fermi level in ^{40}Ca. The upper left, upper right, and bottom left panels display $\widehat{\mathcal{S}}_{p1}$, $\widehat{\mathcal{S}}_{k1}$, and $\widehat{\mathcal{S}}_{k2}$, respectively; while the complete IFSI factor is shown in the bottom right picture.

has to travel through the nucleus leads to a decrease of the real part of $\widehat{\mathcal{S}}_{p1}$. This is followed by an increase for larger r up to $\widehat{\mathcal{S}}_{p1} = 1$. This reduction in ISI effects with increasing r is brought about by the incoming proton's path through the nucleus moving away from the nuclear interior and closer to the less dense nuclear surface. The other curves of the upper left figure reveal a general trend for $90° \leq \theta \leq 180°$: as r increases, the real part of the IFSI factor grows correspondingly. As can be appreciated from Fig. 3.3 as well as from the previous figures, the global behavior of the $\widehat{\mathcal{S}}_{k1}$ factor describing the scattered proton's FSI can be related to that of the ISI factor $\widehat{\mathcal{S}}_{p1}$ through the substitution $\theta \rightarrow 180° - \theta$. This approximate symmetry can be attributed to the small scattering angle θ_1, i.e., the scattered proton leaves

the nucleus almost parallel to the incoming proton's direction. In the bottom left panel, the additional curve ($\theta = 115°$, i.e., close to $180° - \theta_2$) represents the situation of maximal FSI of the ejected nucleon. For this θ value, the path of the ejected nucleon passes through the center of the nucleus, and the distance traveled through the nucleus increases with r. Accordingly, the real part of $\widehat{\mathcal{S}}_{k2}$ is a monotonously decreasing function of r. The other extreme is the $\theta = 0°$ case, where increasing r means less FSI. For the other θ values, the absorption reaches its maximum for some intermediate r value. Again, the combination of $\widehat{\mathcal{S}}_{p1}$, $\widehat{\mathcal{S}}_{k1}$, and $\widehat{\mathcal{S}}_{k2}$ determines the total IFSI factor, with the strongest attenuation predicted in the nuclear interior.

3.1.3 Azimuthal-Angle Dependence

The dependence of the IFSI factor on the azimuthal angle of the collision point is quite straightforward. One representative result is displayed in Fig. 3.4. Here, $\cos\phi \geq 0$ ($\cos\phi \leq 0$) refers to a situation where the hard NN collision occurs in the upper (lower) hemisphere with respect to the yz plane (see Fig. 2.3 for a collision point located in the upper hemisphere). Because of the cylindrical symmetry about the z axis, the factor describing the ISI of the incoming proton is independent of ϕ. Regarding the scattered proton, we observe the least FSI in the upper hemisphere, since the proton then avoids passing through the highly absorbing nuclear interior. For the ejected nucleon, the opposite applies, and the strongest FSI effects are found for $\phi = 0°$. As the xz plane is defined as the scattering plane, the IFSI factor possesses the symmetry $\mathcal{S}_{\mathrm{IFSI}}(r, \theta, 2\pi - \phi) = \mathcal{S}_{\mathrm{IFSI}}(r, \theta, \phi)$ for coplanar scattering.

3.1.4 Level and A Dependence

Results for the emission from levels other than the Fermi level have not been plotted here, because it turns out that the IFSI factors hardly depend on the single-particle level in which the struck nucleon resides. Also, the IFSI factors for neutron emission are almost identical to the corresponding IFSI factors for proton knockout and, as expected, the overall effect of IFSI is more pronounced for heavier target nuclei due to the larger number of scattering centers. The latter is illustrated in Fig. 3.5, which shows the ratio of the ^{40}Ca absolute value of the IFSI factor to the ^{12}C one.

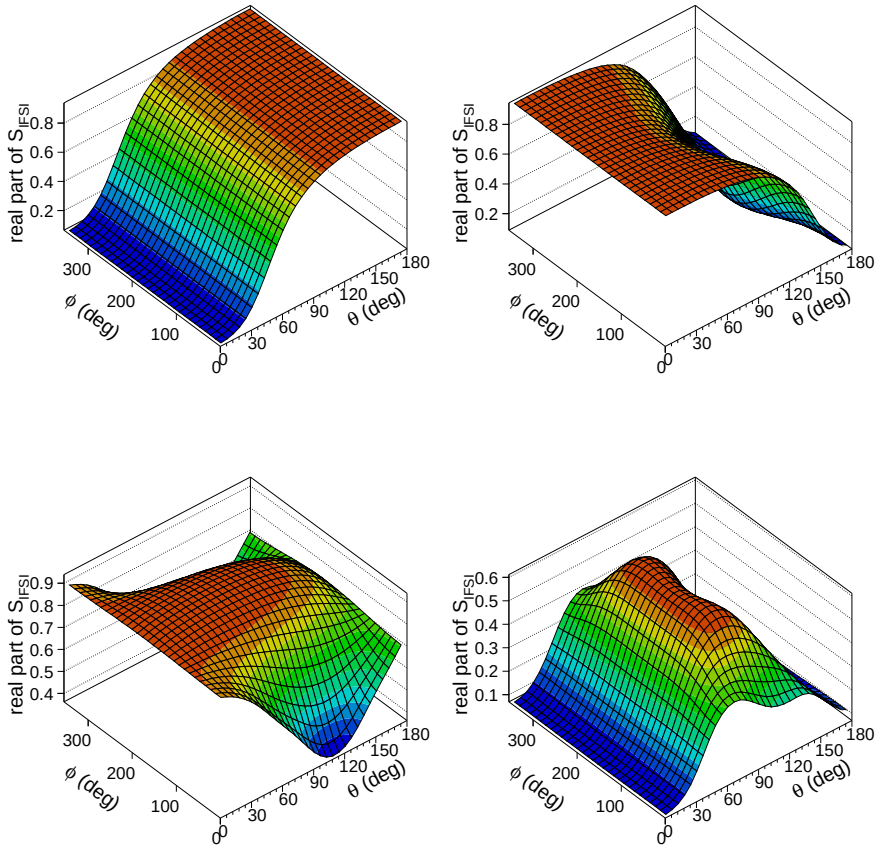

Figure 3.4 The polar- and azimuthal-angle dependence of the real part of $\mathcal{S}_{\rm IFSI}(r = 3\ fm, \theta, \phi)$ for proton knockout from the Fermi level in ^{16}O. Kinematics as in Fig. 3.1. ROMEA calculation with the EDAD2 optical potential [46]. As in the previous figures, the upper left, upper right, and bottom left panels represent the effect of the ISI of the incoming proton, the FSI of the scattered proton, and the FSI of the struck nucleon, respectively; whereas the bottom right figure displays the complete IFSI factor.

3.1.5 Comparison between ROMEA and RMSGA Calculations

In this subsection, we investigate the sensitivity of the computed IFSI factors to the adopted parametrizations for the optical potentials and compare the ROMEA results with the RMSGA predictions. As can be seen in Fig. 3.6, the IFSI factor depends on whether A-dependent (EDAD1/EDAD2) or A-independent (EDAI) fits

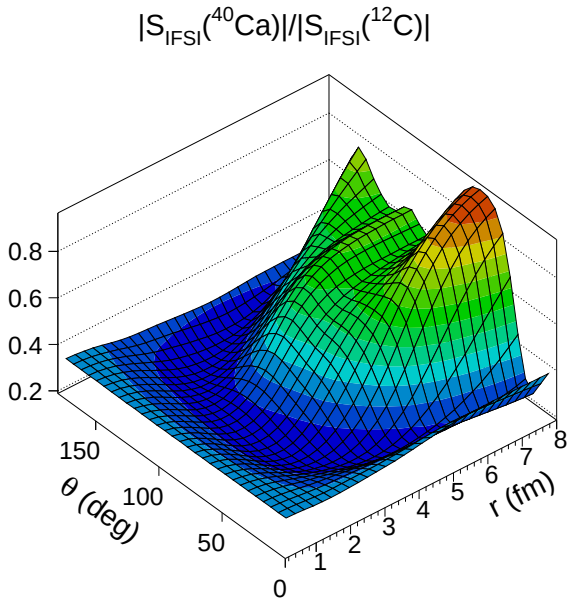

Figure 3.5 The ratio of the ^{40}Ca absolute value of the complete IFSI factor to the ^{12}C one as a function of r and θ. The results are for proton emission from the Fermi level and $\phi = 0°$, and were obtained within the ROMEA model using the EDAD1 optical potential of Ref. [46]. Kinematics as in Fig. 3.1.

for the potentials are selected, but the global features are comparable. Fig. 3.7, as contrasted to Fig. 3.1, demonstrates that the RMSGA method adequately describes the ISI of the incoming proton and the FSI of the scattered proton. However, the discrepancies between ROMEA and RMSGA become significant in the calculation of the FSI of the ejected nucleon (note the different scales in the bottom left panels of Figs. 3.1 and 3.7), and, therefore, also in the complete IFSI factor. The noted difference is attributed to the low ejectile kinetic energy ($T_{k2} \approx 114$ MeV for the specific case of Fig. 3.7, and comparable values for knockout from other levels and other nuclei). At such low energies, the RMSGA predictions are not realistic because of the underlying approximations, mostly the postulation of linear trajectories and frozen spectator nucleons. So, for the kinematics discussed here, the ROMEA method is to be preferred over the RMSGA one, as the latter overestimates the distortion for the low-energetic ejectile nucleon.

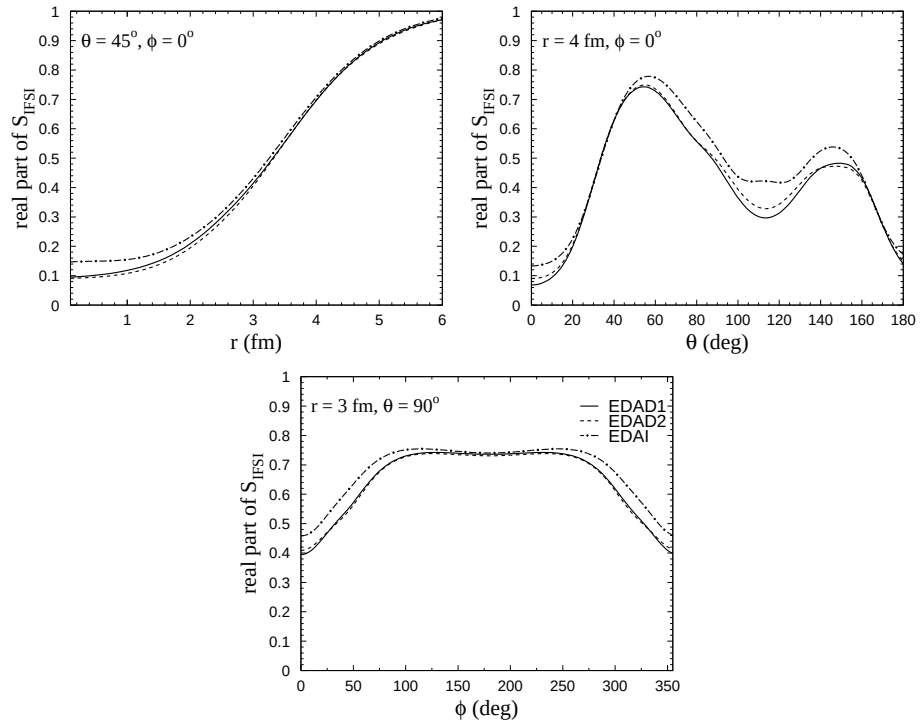

Figure 3.6 The sensitivity of the real part of the complete IFSI factor for neutron knockout from ^{12}C to the adopted choice for the parametrization of the optical potentials. Results of ROMEA calculations with the EDAD1 (solid curve), EDAD2 (dashed curve), and EDAI (dot-dashed curve) optical potentials are shown. Kinematics as in Fig. 3.1.

3.2 Radial and Polar-Angle Contributions to $A(p, pN)$ Cross Sections

In Section 3.1.4, it was already mentioned that the IFSI factors are insensitive to the single-particle level from which the nucleon is ejected. The peculiar spatial characteristics of the different single-particle orbits have an impact on the observables, though. Indeed, the distorted momentum-space wave function $\phi^D_{\alpha_1}$ of Eq. (2.35) is determined by the values of the IFSI factor folded with a relativistic bound-state wave function $\phi_{\alpha_1}(\vec{r})$. As the particles experience less IFSI close to the nuclear surface, one obtains a stronger reduction of the quasifree cross section for nucleon knockout from a level which has a larger fraction of its density in the nuclear interior. This will become apparent in Fig. 3.8, but even more so in Section 3.3.1.

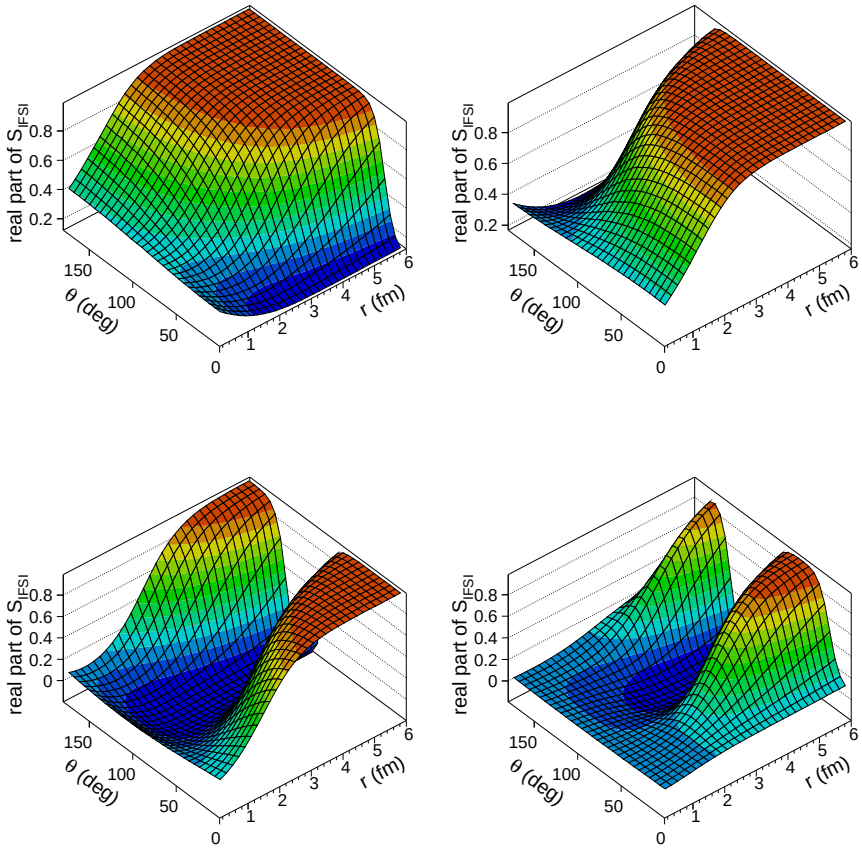

Figure 3.7 As in Fig. 3.1, but using the RMSGA method.

Fig. 3.8 shows a function $\delta_r\,(r)$ which represents the contribution of the nuclear region with radial coordinate r to the differential cross section. The procedure for calculating this function is similar to the method exposed in Ref. [118] and is developed in Appendix C. Comparison of the upper and lower panels illustrates that IFSI mechanisms make the $A(p, 2p)$ cross sections reflect surface mechanisms, unlike the $A(e, e'p)$ reaction where the weakly interacting electron probes the entire nuclear volume and only the outgoing proton interacts with the residual system. Apart from the shift to higher r, the IFSI brings about a strong reduction in the magnitude of the cross sections, whereby the Fermi level is least affected. Even though

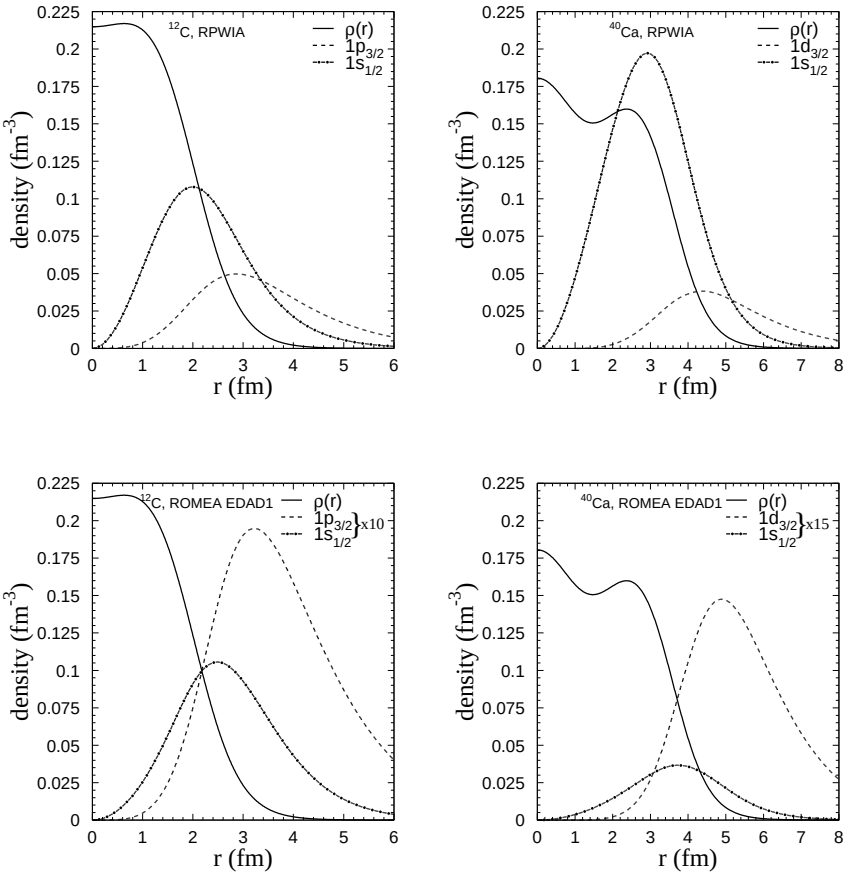

Figure 3.8 Contribution to the $A(p,2p)$ cross section $\delta_r\,(r)$ as a function of r. The upper figures present the results obtained after setting the IFSI factor $\mathcal{S}_{\rm IFSI}(\vec{r})$ equal to 1 in Eq. (C.4), whereas in the lower panels the ROMEA calculations using the EDAD1 optical potential of Ref. [46] are depicted. The dashed (dot-dashed) curves show the result for emission from the Fermi (lowest lying $1s_{1/2}$) level. The baryon density $\rho\,(r)$ is also shown (solid curve). The ordinate is given for $\rho\,(r)$. The $\delta_r\,(r)$ are plotted in units of fm^2 up to an arbitrary scaling factor. The kinematics was $T_{p1} = 1$ GeV, $T_{k1} = 870$ MeV, $\theta_1 = 13.4^\circ$, and $\theta_2 = 67^\circ$.

$\delta_r\,(r)$ is concentrated in the surface region, the average density seen through this reaction still amounts to 0.069 fm^{-3} (0.080 fm^{-3}) or 32% (45%) of the central density in the case of $1s_{1/2}$ knockout from ^{12}C (^{40}Ca). In the case of emission from the Fermi level, on the other hand, the average density is only 12% (13%) of the central density for a ^{12}C (^{40}Ca) target.

In Fig. 3.9 we show which (r, θ) coordinates of the collision point provide the largest contributions to the cross section. The kinematics was the same as in Fig. 3.8 and the ROMEA calculations used the EDAD1 optical potential. As can be inferred from the left panels, the contributions to the RPWIA cross sections are symmetric around $\theta = 90^\circ$. The IFSI not only shift the maximum in $\delta_{r,\theta}$ to higher r, but also to lower values of θ. This can be explained by looking at the complete IFSI factor in Fig. 3.1: the attenuation effect is clearly larger for $\theta \geq 90^\circ$. Apart from breaking the symmetry around $\theta = 90^\circ$, the IFSI also narrow the peak in the θ dependence. Of course, these IFSI effects are most pronounced for the lowest lying $1s_{1/2}$ level.

3.3 Numerical Results for $A(p, pN)$ Differential Cross Sections

3.3.1 ^{12}C, ^{16}O, and ^{40}Ca$(p, 2p)$ and (p, pn) at 1 GeV

The PNPI experiment [114] was carried out with an incident proton beam of energy 1 GeV. The scattered proton was detected at $\theta_1 = 13.4^\circ$ with a kinetic energy between 800 and 950 MeV, while the knocked-out nucleon was observed at $\theta_2 = 67^\circ$ having a kinetic energy below 200 MeV.

Figs. 3.10–3.12 display a selection of differential cross section results as a function of the kinetic energy of the most energetic nucleon in the final state. The EDAI optical potential [46] was used for the ROMEA calculations. The other parametrizations of Ref. [46] produce similar predictions, whereas the RMSGA approach fails to give an adequate description of the data because of the low kinetic energy of the ejected nucleon. Since the experiment of Ref. [114] only measured relative cross sections, the ROMEA results were normalized to the experimental data.

The ROMEA calculations reproduce the shapes of the measured differential cross sections. Furthermore, comparison of the RPWIA and ROMEA calculations shows that the effect of the IFSI is twofold. First, IFSI result in a reduction of the RPWIA cross section that is both level and A dependent. From the figures it is clear that ejection of a nucleon from a deeper lying level leads to stronger initial- and final-state distortions. This reflects the fact that the incoming and outgoing nucleons encounter more obstacles when a deeper lying bound nucleon is probed. The A dependence also conforms with our expectations, i.e., the IFSI effects are

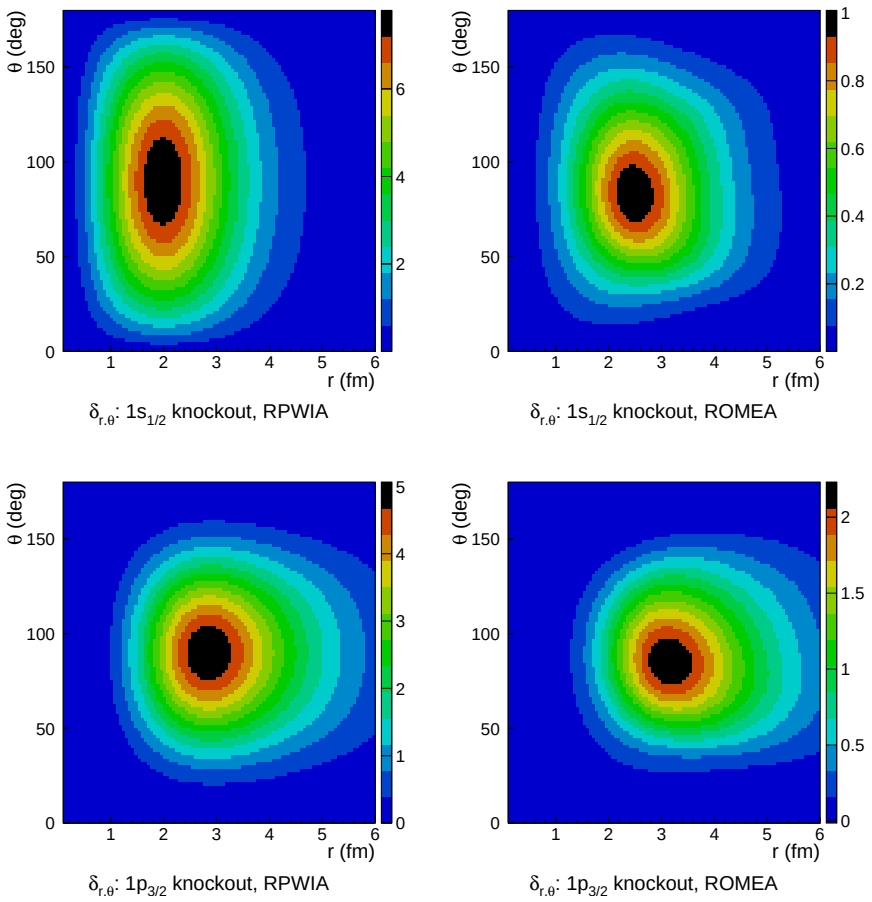

Figure 3.9 Contribution to the $A(p, 2p)$ cross section $\delta_{r,\theta}(r, \theta)$ (in units of fm^2 up to an arbitrary scaling factor) as a function of the radial coordinate r and polar angle θ of the hard collision point. The function $\delta_{r,\theta}(r, \theta)$ is defined in Appendix C. The upper (lower) figures show the results for emission from the $1s_{1/2}$ ($1p_{3/2}$) level in ^{12}C.

larger for heavier nuclei. Besides the attenuation, the IFSI also make the measured missing momentum different from the initial momentum of the struck nucleon. As can be inferred from Fig. 3.13, this momentum shift leads to an asymmetry between the positive and negative missing-momentum side of the momentum distribution. Note that a positive missing momentum corresponds to $p_{m_x} = k_1 \sin\theta_1 + k_2 \sin\theta_2 \cos\phi_2 > 0$.

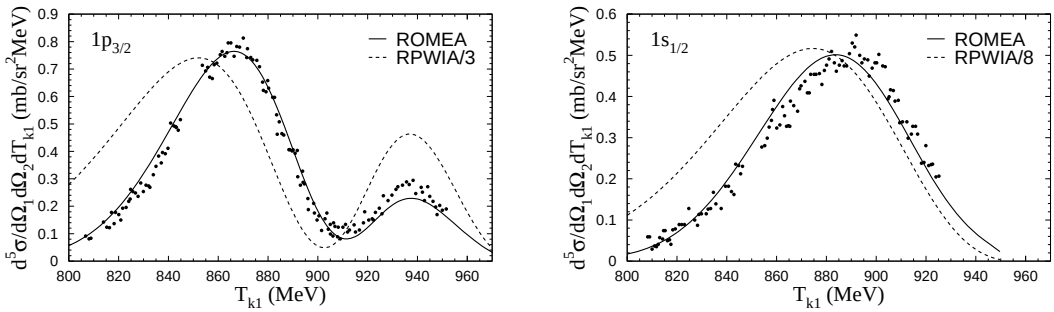

Figure 3.10 Differential cross section for the ^{12}C$(p, 2p)$ reaction. The solid curve represents the ROMEA calculation, whereas the dashed curve is the plane-wave result reduced by the indicated factor. The ROMEA results are normalized to the data. Data points are from Ref. [114]. The magnitude of the experimental error bars is estimated to be of the order of 5–10%.

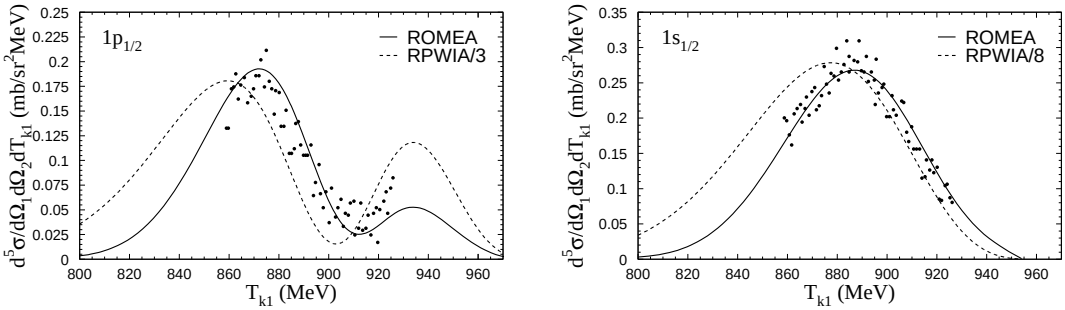

Figure 3.11 As in Fig. 3.10, but for the ^{16}O(p, pn) reaction.

3.3.2 ^{40}Ca$(p, 2p)$ at 460 MeV

Next, we focus on a ^{40}Ca$(p, 2p)$ experiment conducted at the EFI facility in Chicago by Tyrén *et al.* [115]. The impinging proton had a kinetic energy of $T_{p1} = 460$ MeV, while the outgoing protons were detected at symmetric coplanar angles ($\theta_1 = \theta_2$ and $\phi_2 = 180°$) and equal momenta ($k_1 = k_2$). The differential cross sections for $1d_{3/2}$, $1d_{5/2}$, and $2s_{1/2}$ knockout are displayed as a function of the scattering angle

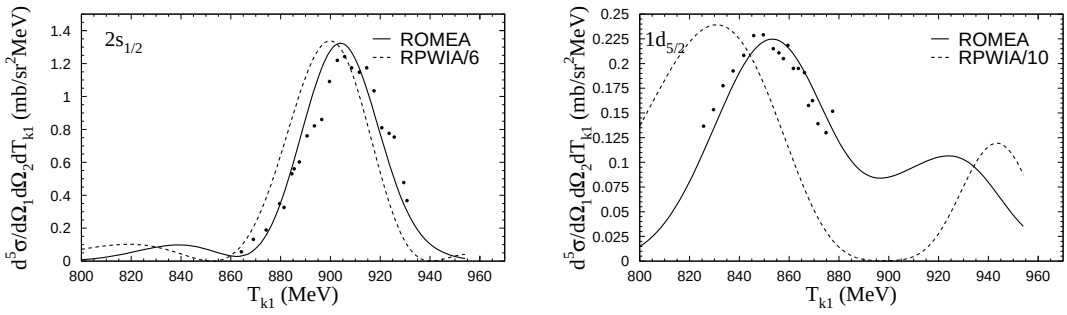

Figure 3.12 As in Fig. 3.10, but for the ^{40}Ca(p, pn) reaction.

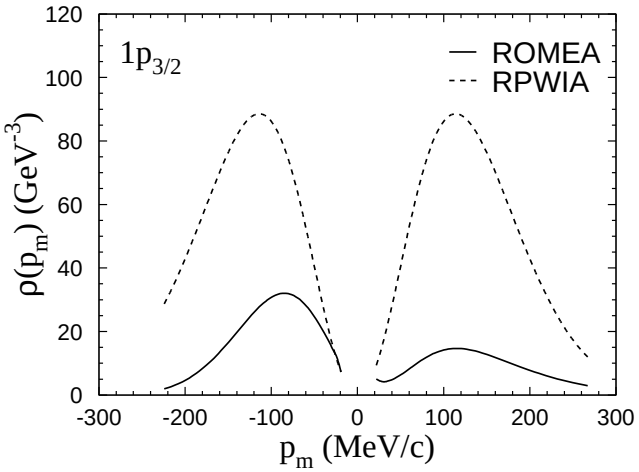

Figure 3.13 The ^{12}C$(p, 2p)$ momentum distribution for the $1p_{3/2}$ state as a function of the missing momentum. The solid (dashed) curve represent ROMEA (RPWIA) calculations.

$\theta_1 = \theta_2$ in Figs. 3.14, 3.15, and 3.16, respectively. The solid curves show the ROMEA calculations assuming full occupancy of the shells, while the dashed curves are scaled by the spectroscopic factors.

The shape of the $1d_{3/2}$ cross section is nicely reproduced by the calculations, although the solid curve somewhat overestimates the magnitude. Normalization

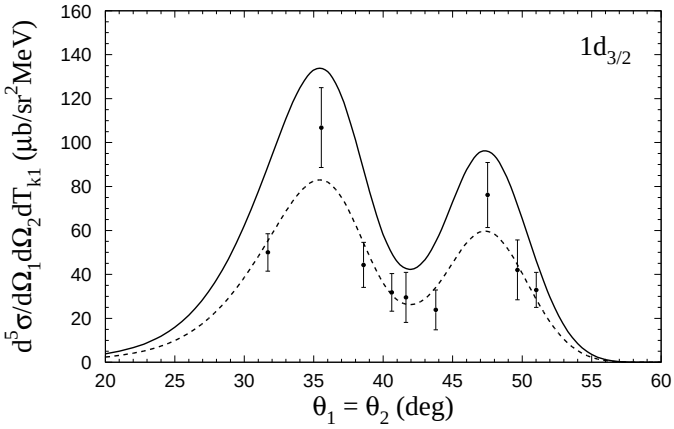

Figure 3.14 Symmetric coplanar angular distribution for the ^{40}Ca$(p, 2p)^{39}$K$(1d_{3/2}^{-1})$ reaction at 460 MeV. The curves are obtained from a ROMEA calculation with the EDAD2 optical potential [46]. The data are taken from Ref. [119], a re-analysis of the original experiment [115].

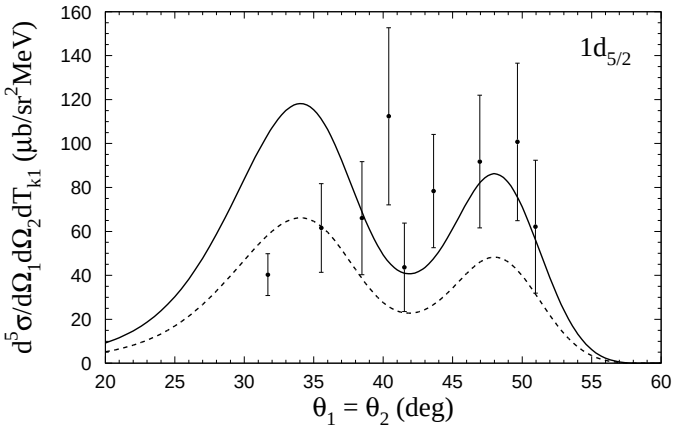

Figure 3.15 As in Fig. 3.14, but for knockout from the $1d_{5/2}$ shell.

to the data leads to a spectroscopic factor of 0.62. For the $1d_{5/2}$ shell, the overall magnitude of the data is quite well reproduced, but the shape of the calculated distribution is in poor agreement with the data. However, it should be noted that the error bars on the experimental $1d_{5/2}$ cross sections are relatively large, making it difficult to draw any meaningful conclusion. Finally, our calculations describe the

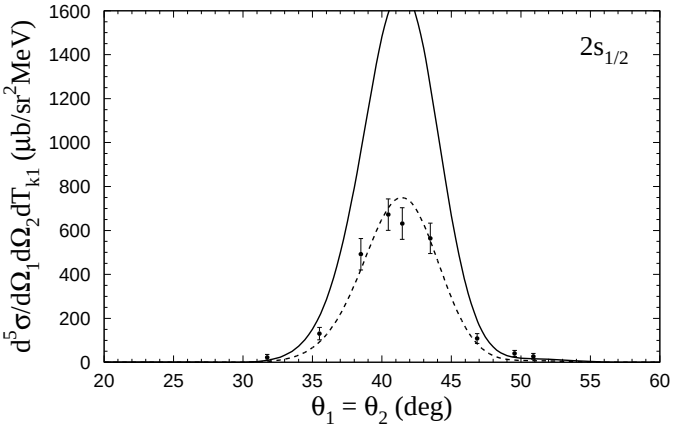

Figure 3.16 As in Fig. 3.14, but for knockout from the $2s_{1/2}$ shell.

shape of the $2s_{1/2}$ cross section very well, but overshoot the data by a factor of more than 2. Therefore, the conclusion that the occupation number for the $2s_{1/2}$ shell is significantly smaller than the shell-model value of 2 seems inescapable. This depletion of the occupancy of single-particle levels that are fully occupied in the naive independent-particle model is a general feature of nuclear matter and has been confirmed by both experimental and theoretical studies [120]. However, the fact that the $2s_{1/2}$ shell is so strongly depleted has so far not been explained theoretically or corroborated by other experiments. For example, from the ^{40}Ca$(e,e'p)$ data of Ref. [121], a spectroscopic factor of 0.66 was deduced for the $2s_{1/2}$ orbital. The $1d_{3/2}$ spectroscopic factor of 0.65 obtained from this experiment, on the other hand, does agree with our value.

3.3.3 ^{16}O$(p,2p)$ and (p,pn) at 505 MeV

At TRIUMF, cross sections for scattering off ^{16}O in coplanar kinematics have been measured at several incident energies. First, we consider the ^{16}O(p,pN) experiment carried out by McDonald *et al.* [116]. Their data were obtained at an incident energy of 505 MeV with the scattered proton detected at $\theta_1 = 22.15^\circ$ and the ejected nucleon at various angles centered about the quasifree angle. In Fig. 3.17 our ROMEA calculations are compared with the data for $(\theta_1,\theta_2) = (22.15^\circ, 53.7^\circ)$.

Overall, the shapes of the calculated cross sections as a function of the kinetic

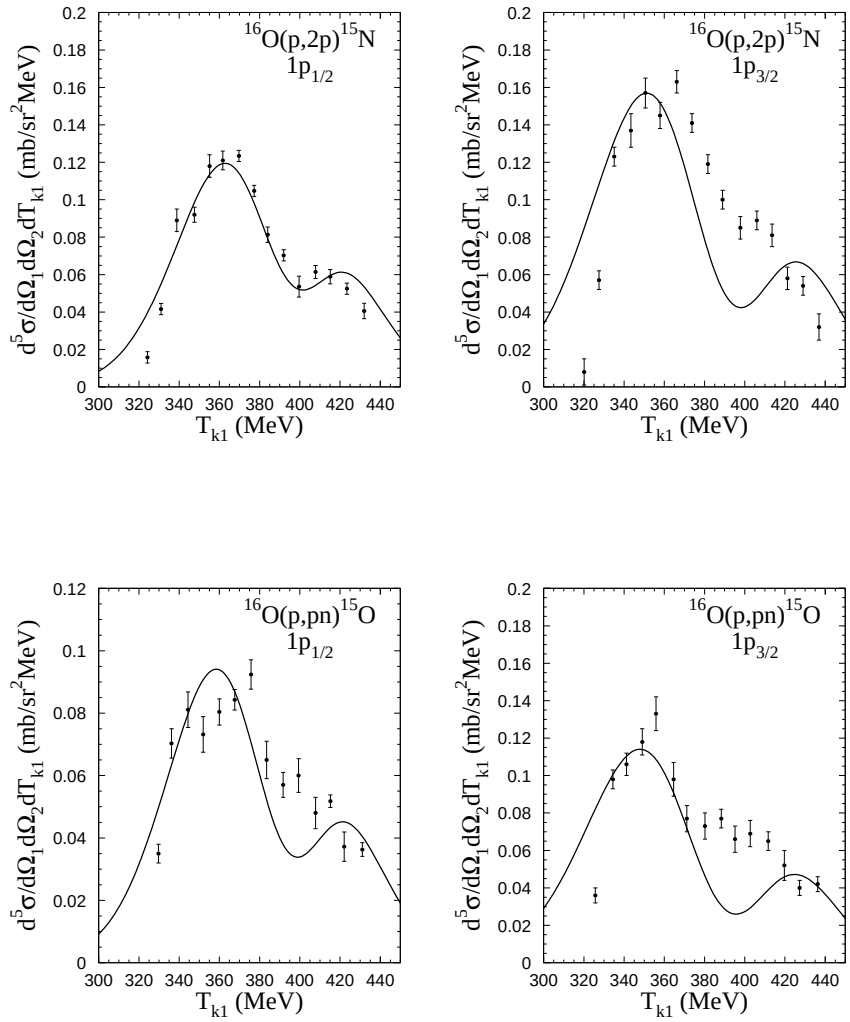

Figure 3.17 Differential cross sections for the $^{16}\mathrm{O}(p, 2p)^{15}\mathrm{N}$ (upper row) and $^{16}\mathrm{O}(p, pn)^{15}\mathrm{O}$ (lower row) reactions. The left panels correspond with knockout from the $1p_{1/2}$ orbital, while the right panels show $1p_{3/2}$-shell knockout cross sections. The incoming proton beam had an energy of 505 MeV and the scattering angles of the outgoing nucleons were $(\theta_1, \theta_2) = (22.15°, 53.7°)$. The curves are ROMEA calculations with the EDAD1 optical potential [46], normalized to the data. The data are from Ref. [116].

energy T_{k1} of the scattered proton follow the trend of the experimental results. In general, the experimental cross sections for knockout from the $1p_{1/2}$ state are described somewhat better than the $1p_{3/2}$ data. Further, the calculations overestimate the experimental values by a factor between 1.2 and 1.8. The spectroscopic factors normalizing the calculations to the data are the largest (smallest) for neutron knockout from the $1p_{3/2}$ shell (proton knockout from the $1p_{1/2}$ shell) and depend slightly on the choice for the optical potential. The results of our calculations are similar to those of Ref. [31].

3.3.4 ^{16}O$(p,2p)$ at 200 MeV

Another TRIUMF experiment [8] studied the reaction ^{16}O$(p,2p)$ at 200 MeV incoming energy. The differential cross section $d^5\sigma/d\Omega_1 d\Omega_2 dE_{\rm diff}$, where $E_{\rm diff} = T_{k1} - T_{k2}$, was measured at 10 pairs of coplanar scattering angles (θ_1, θ_2). Fig. 3.18 shows a representative sampling of the cross-section results. Overall, the ROMEA model provides a good description of the data as both the peak positions and the widths of the experimental cross sections are reproduced. Again, the agreement with the data is slightly better for the $1p_{1/2}$ shell. The values for the spectroscopic factors are consistent with those of Section 3.3.3.

3.3.5 ^{4}He$(p,2p)$ at 250 MeV

Finally, we present some results for the ^{4}He$(p,2p)$ reaction at an incident proton energy of 250 MeV. Fig. 3.19 compares the data from the TRIUMF experiment of Ref. [9] with ROMEA calculations using the optical potential of van Oers *et al.* [9]. The typical shape for knockout of an s-state proton is reproduced by the ROMEA predictions.

The analysis of the different experiments in this chapter has shown that our ROMEA formalism explains the global shape of the differential cross sections. The fair agreement with the data of Sections 3.3.4 and 3.3.5 demonstrates that the ROMEA model works satisfactorily at lower incident energies. While the shape of the $A(p,pN)$ differential cross sections is probably not substantially affected by spin effects, this is not the case for $A(p,pN)$ spin observables like the analyzing power. To adequately describe these observables, it is necessary to add the spin-orbit potential in the treatment of the IFSI in our model.

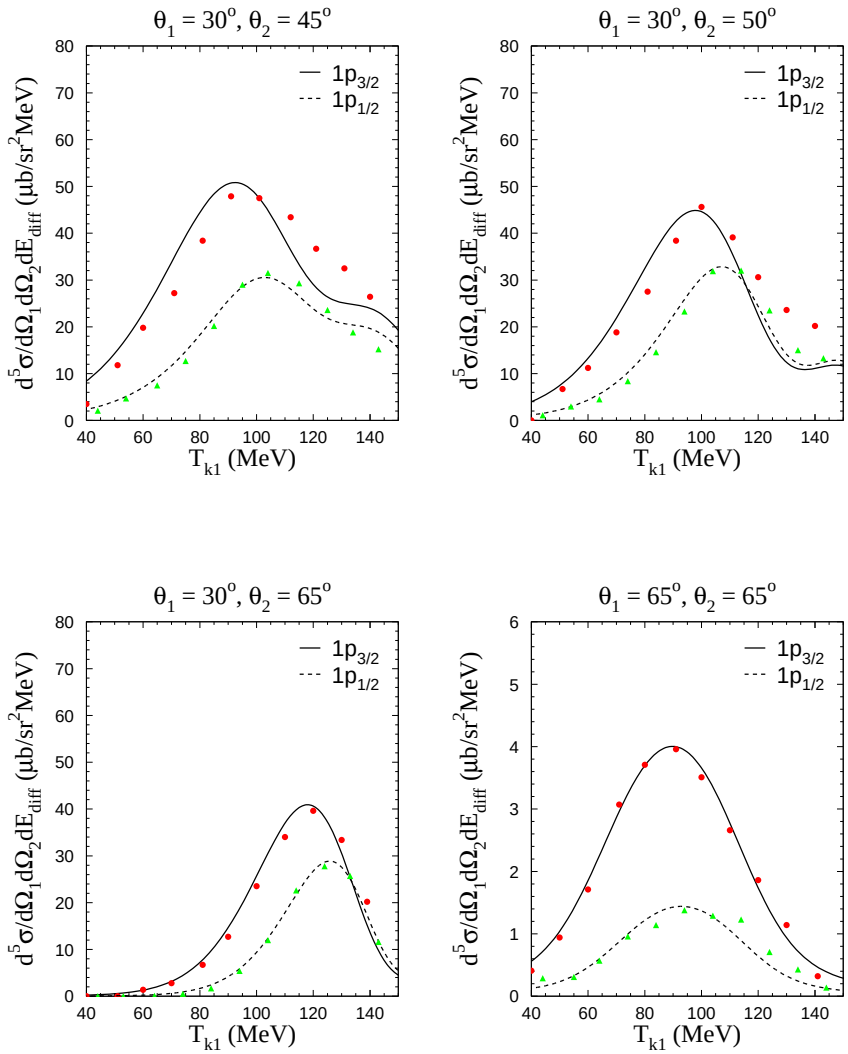

Figure 3.18 ^{16}O$(p, 2p)$ differential cross sections for four of the angle combinations (θ_1, θ_2) of experiment [8]. The curves showing our ROMEA calculations based on the EDAI optical potential [46] are normalized to the data points from Ref. [8]. The solid lines and red circles pertain to the $1p_{3/2}$ state, while the dashed lines and green triangles correspond to the $1p_{1/2}$ state.

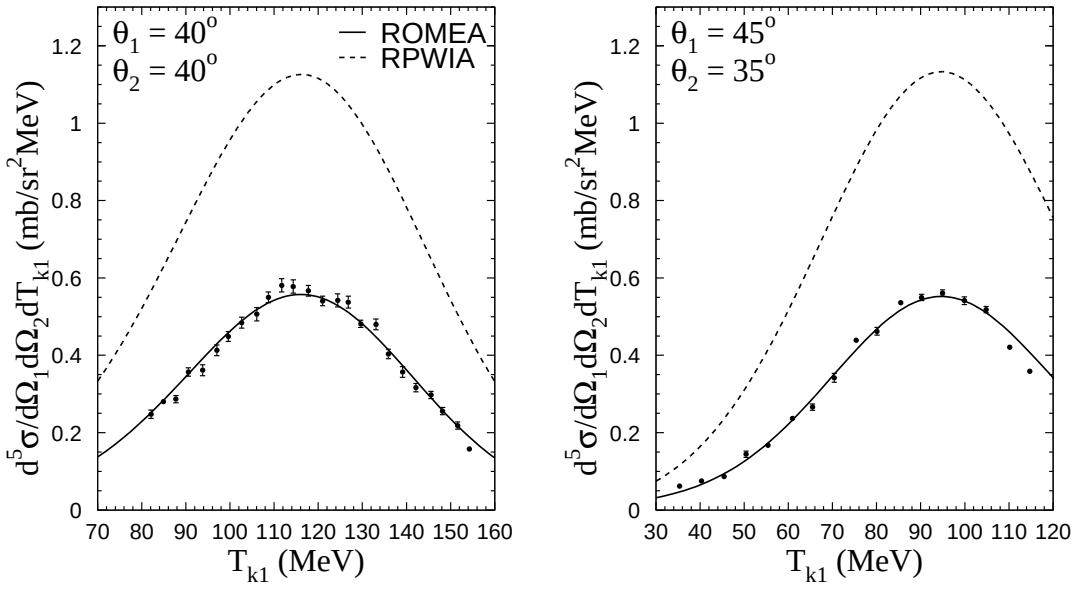

Figure 3.19 Differential cross section for the ^{4}He$(p, 2p)$ reaction at angle pairs $(40°, 40°)$ and $(45°, 35°)$ at 250 MeV. The solid (dashed) curves refer to ROMEA (RPWIA) results. The data are from Ref. [9].

Chapter 4

Nuclear Transparency from $A(p, 2p)$ Reactions

The transition region between nucleon-meson (hadronic) and quark-gluon (partonic) degrees of freedom is a topic of longstanding interest in nuclear physics. A promising observable to map this transition is the transparency of the nuclear medium to the propagation of hadrons. In $A(p, 2p)$ experiments, the nuclear transparency is defined as the ratio of the cross section per nucleon to the hydrogen one. Accordingly, the nuclear transparency is a measure for the attenuation effects of the spectator nucleons on the impinging and outgoing protons.

In the conventional Glauber picture [71], the nuclear transparency extracted from $A(p, 2p)$ reactions is predicted to be rather constant for incoming momentum larger than a few GeV/c. The color transparency (CT) phenomenon suggests an anomalously large transmission probability of protons through nuclei [122, 123] and leads to a nuclear transparency that increases with incoming momentum. At Brookhaven National Laboratory (BNL), two experiments, E834 [124] and E850 [125, 126], measured the nuclear transparency in the $A(p, 2p)$ quasielastic scattering process near 90° in the pp c.m. frame. As can be appreciated from Fig. 4.1, the data suggest a CT-like increase in the transparency for impinging proton momenta between 5 and 10 GeV/c. For higher momenta, the measured nuclear transparency falls back to the level predicted by typical Glauber calculations. This oscillatory energy dependence is not unique to the $A(p, 2p)$ nuclear transparency: it has been observed or hinted at in pp elastic scattering [127], elastic πp fixed-angle

scattering [128–134], pion photoproduction [134–137], and deuteron photodisintegration [138–143].

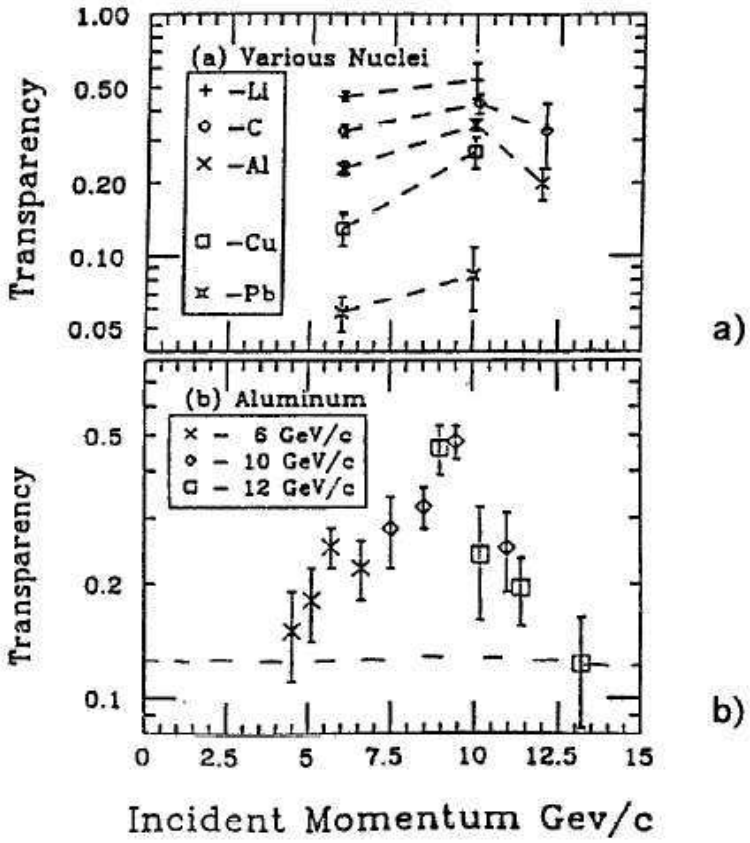

Figure 4.1 The beam-momentum dependence of the $A(p, 2p)$ nuclear transparency as measured in the E834 experiment [124]. The upper panel shows the transparency as a function of the incoming lab momentum p_1 for various nuclear targets and -0.2 GeV/c $< p_{m_z} < 0.1$ GeV/c, with p_{m_z} the longitudinal component of the missing momentum. In the bottom panel, the ^{27}Al data points are plotted versus the effective incident momentum $p_{\text{eff}} = p_1(1 - p_{m_z}/M_p)$, which takes the motion of the target proton in the nucleus into account. The dashed line in the bottom panel corresponds to a Glauber calculation. This figure is taken from Ref. [124].

Two explanations for the measured energy dependence of the $A(p, 2p)$ transparency have been proposed [144,145]. Both the Ralston-Pire [144] and the Brodsky-de Teramond model [145] are based on the presence of two terms in the free pp scattering amplitude: one representing a small object and the other representing a

normal-sized object. The interference between these two amplitudes induces the oscillation of the free pp cross section about the scaling behavior. Inside the nuclear medium, the normal-sized components in the hadron wave functions are filtered away. This phenomenon of "nuclear filtering" (NF) [144,146,147] reproduces qualitatively the observed bump in the $A(p,2p)$ transparency.

In this chapter, the relativistic and cross-section factorized framework of Section 2.1 is extended to incorporate the Ralston-Pire model for the pp scattering amplitude and the concepts of CT and NF. Section 4.1 is devoted to the Ralston-Pire description of elastic pp scattering. In Section 4.2, the idea of nuclear filtering is reviewed and the $A(p,2p)$ formalism of Section 2.1 is adjusted to take into account both the small-sized and the normal-sized contribution to the hard pp scattering amplitude. The IFSI effects are computed within the RMSGA approaches of Sections 2.3 and 2.4. The phenomenon of CT constitutes the subject of Section 4.3. To estimate its effects, we consider the quantum diffusion model of Ref. [148] and the hadronic picture of Jennings and Miller [149]. The comparison between the two CT models is made in a consistent way. This implies that all the ingredients in the transparency calculations not related to CT are kept identical. Section 4.4 presents the nuclear transparency results for the target nuclei ^{7}Li, ^{12}C, ^{27}Al, and ^{63}Cu. The effect of IFSI, CT, and NF is discussed. Furthermore, the accuracy of the approximated RMSGA approach is investigated and the two CT treatments are compared. Finally, some concluding remarks and an outlook with regard to the research into nuclear transparency can be found in Section 4.5.

The results contained in this chapter have been published in Ref. [150].

4.1 High-Momentum-Transfer Wide-Angle Scattering

At low energies or long distances, the global features of the strong interaction can be described within the nucleon-meson picture [151]. At high energies or short distances, perturbative QCD (pQCD) provides a precise description of hadronic reactions in terms of quark-gluon degrees of freedom. At present, it is not clear how these two regimes are connected. Exclusive hadronic reactions such as proton-proton elastic scattering, meson photoproduction and deuteron photodisintegration have been studied extensively in order to explore this transition region. Excellent reviews can be found in Refs. [152,153].

4.1.1 Quark-Counting Rule

At high energy and large momentum transfer, the differential cross section for many exclusive $A + B \rightarrow C + D$ reactions [154] obeys the quark-counting (QC) rule [155–158]

$$\left(\frac{d\sigma}{dt}\right)_{AB\rightarrow CD} \propto s^{2-n} f(\frac{t}{s}) \ , \tag{4.1}$$

$$\text{for } s \rightarrow \infty \ , \ \frac{t}{s} \equiv \text{const} \ , \ n = n_A + n_B + n_C + n_D \ .$$

Here, the variables s and t are the Mandelstam variables

$$s = (P_A + P_B)^2 \ , \ t = (P_A - K_C)^2 \ , \tag{4.2}$$

where P_A, P_B and P_C are the four-momenta of the hadrons. n_A, n_B, n_C, and n_D are the number of valence quarks inside the hadrons A, B, C, and D, respectively. For pp scattering, the differential cross section scales roughly as $\left(\frac{d\sigma}{dt}\right)_{pp\rightarrow pp} \propto s^{-10}$. As for the function $f(\frac{t}{s})$, which describes the angular dependence of the differential cross section, no rigorous pQCD calculation has been performed yet. The constituent interchange model [159] predicts

$$f(\frac{t}{s}) \equiv f(\cos\theta_{\text{c.m.}}) = \left(1 - \cos^2\theta_{c.m.}\right)^{-4\gamma} \ , \tag{4.3}$$

where γ can be in the range 1.3–2.0.

Eq. (4.1) is also known as the dimensional scaling law, since it was originally derived [155–157] using dimensional analysis. The main assumption of this analysis is that only one constituent (a dimensionless point-like quark) of each hadron participates in the reaction whereas the other constituents are spectators. In order for the spectator quarks to be able to follow the interacting quarks after the wide-angle scattering, each hadron must fluctuate to its minimal Fock space component during the reaction. This minimal state must be much smaller than a regular hadron because otherwise the spectator quarks will continue in their original direction independently from the interacting quark and produce more hadrons, thus destroying the exclusive nature of the reaction. The amplitude for such a fluctuation is $\left(\frac{1}{q}\right)^{n_i-1}$ per hadron, where q is the momentum transfer of the reaction (assumed to be transferred directly between the two interacting quarks) and n_i is the number of

quarks in hadron i. The combination of these amplitudes leads to Eq. (4.1). Later, this naive description was confirmed by a short-distance pQCD derivation [158].

Fig. 4.2 shows the diagrams which contribute to the quark-counting scattering. The QC process is characterized by the exchange of five hard gluons inside the interacting hadrons. The quark-interchange diagram presented in the right panel of Fig. 4.2 dominates the cross section [160, 161].

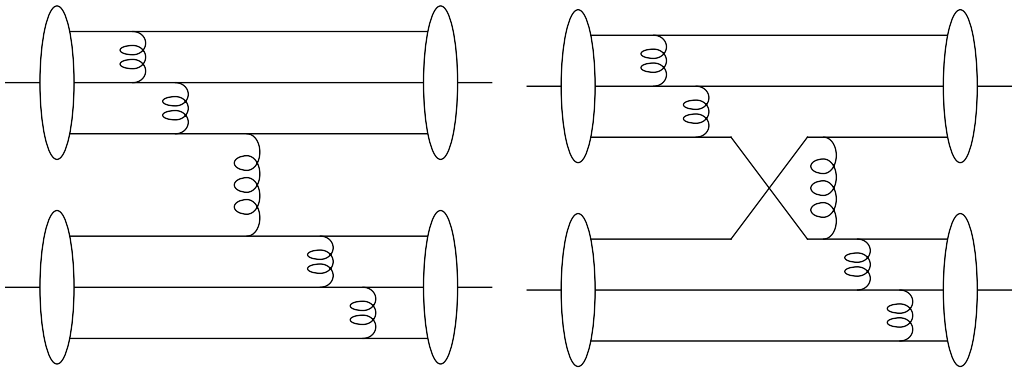

Figure 4.2 Typical diagrams for quark-counting scattering. The left panel shows the pure gluon-exchange diagram, while the quark-interchange mechanism is represented in the right panel.

Despite the success of pQCD in describing the energy dependence of exclusive cross sections at fixed center-of-mass scattering angle, there are strong indications that the short-distance pQCD picture might be wrongly built into dogma. The hadron helicity conservation (HHC) rules predicted by the asymptotic short-distance approach of Brodsky and Lepage [162] are violated by experimental data in the same energy and momentum region [163–166]. However, the statement that hadron helicity flip is in contradiction with pQCD is currently under debate [167, 168]. In pp scattering, the striking energy and angular dependence of the spin-spin correlation factor A_{NN} attracts attention [169–173]. Furthermore, pQCD calculations of the magnitudes of form factors [174–177] fail to describe the data, as non-perturbative long-distance effects are shown to play a crucial role. Often, the QC rule of Eq. (4.1) is only approximately obeyed. Indeed, when examined in detail, several reactions exhibit oscillations around the overall scaling-law dependence. The oscillatory behavior of the free pp scattering is illustrated in Fig. 4.3.

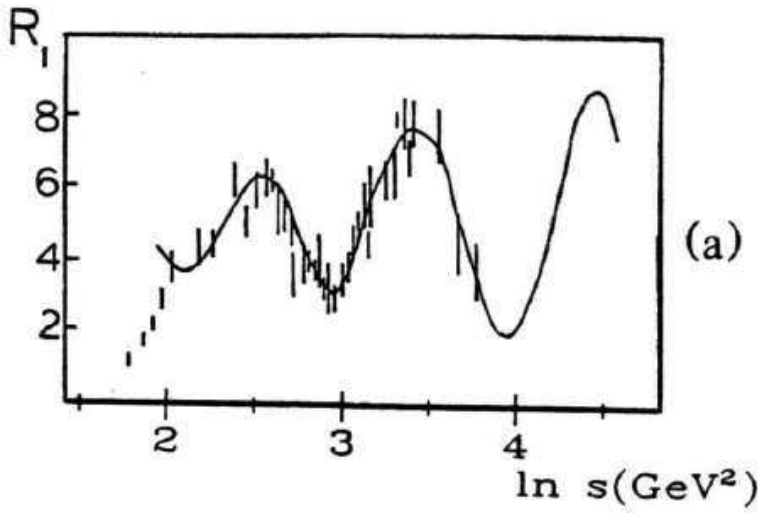

Figure 4.3 The energy dependence of $R_1\,(s) = \text{const}\, s^{10}\,(d\sigma/dt)_{pp\to pp}\,|_{90^\circ}$ for the high-energy pp elastic scattering at 90° c.m. angle. The data are compared to the parametrization of Eq. (4.8) (solid line). This figure is taken from Ref. [178].

4.1.2 Landshoff Scattering

Besides the quark-counting scattering of Section 4.1.1, another scattering mechanism is considered to play a role in exclusive high-momentum-transfer hadronic reactions. This process was proposed by Landshoff [179–181] and is referred to as the multiple-scattering model, independent scattering, or Landshoff scattering. The diagram for this process is displayed in Fig. 4.4: each constituent quark of one hadron scatters on one of the quarks of the other hadron. The pairs of quarks scatter independently and the energy dependence of the cross section is obtained through the condition that the outgoing quarks must align to recombine to a hadron. The s dependence of the cross section is found to be

$$\left(\frac{d\sigma}{dt}\right)_{AB\to CD} \propto s^{-n}\, f(\frac{t}{s})\;, \tag{4.4}$$

$$\text{for } s\to\infty\;,\;\; \frac{t}{s} \ll 1\;,\;\; n = 8 \text{ for } pp \text{ scattering}\;.$$

The main feature of this picture is that the hadrons stay normal-sized during the interaction. At first sight, the Landshoff mechanism is expected to dominate at high energies, in disagreement with the available data. However, Landshoff scattering

is partially suppressed by soft gluon radiation [182]. The radiative corrections are taken into account through Sudakov form factors [183–186] and bring the cross section dependence for the Landshoff mechanism close to $d\sigma/dt \propto s^{-10}$ for pp scattering [178].

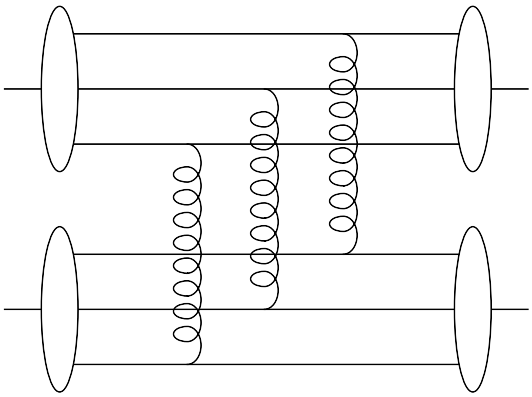

Figure 4.4 Scattering via the Landshoff mechanism.

4.1.3 Ralston-Pire Picture and Parametrization of the Free pp Cross Section

Ralston and Pire explained the oscillations in free pp scattering by the interference between the quark-counting and the Landshoff amplitude. In their approach [178, 187], the spin-averaged pp scattering amplitude consists of the quark-counting (QC) and the Landshoff (L) contribution:

$$\mathcal{M}^{pp} = \mathcal{M}^{pp}_{\mathrm{QC}} + \mathcal{M}^{pp}_{\mathrm{L}} \; . \tag{4.5}$$

The Landshoff term can be related to the quark-counting term through

$$\mathcal{M}^{pp}_{\mathrm{L}} = \frac{\rho_1}{2} \sqrt{\frac{s}{1\,GeV^2}}\, e^{\pm\, i\, \left(\phi(s)+\delta_1\right)}\, \mathcal{M}^{pp}_{\mathrm{QC}} \; . \tag{4.6}$$

Here, $\rho_1 = 0.08$ and $\delta_1 = -2.0$ is an incalculable, energy-independent phase. These values were determined from a fit to the pp data at 90° [178, 187]. The energy-dependent phase $\phi\,(s)$ arises from the gluonic radiative corrections and is calculable in pQCD [178, 187, 188]:

$$\phi\,(s) = \frac{\pi}{0.06}\, \ln\left\{\ln\left[\frac{s}{0.01\,GeV^2}\right]\right\} \; . \tag{4.7}$$

The quantum electrodynamics (QED) variant of this effect is observed in charged-particle scattering: the Coulomb-nuclear interference phase shift between the strong-interaction and the electromagnetic contributions to the scattering amplitude [189–191]. By analogy with this Coulomb-nuclear interference effect, $\phi(s)$ is called the chromo-Coulomb phase shift. The sole parameter which remains undetermined is the sign of the phase difference $\phi(s) + \delta_1$ between the quark-counting and the Landshoff term. Therefore, both possibilities are tested in the calculations of the nuclear transparency.

For the parametrization of the free pp scattering cross section $\left(\frac{d\sigma}{dt}\right)_{pp\to pp}$, the Ralston-Pire separation of Eq. (4.6) is combined with the $\theta_{\mathrm{c.m.}}$ dependence suggested by [159] (see Eq. (4.3)). This leads to [67]

$$\begin{aligned}\left(\frac{d\sigma}{dt}\right)_{pp\to pp} &\propto \left|\mathcal{M}^{pp}_{\mathrm{QC}} + \mathcal{M}^{pp}_{\mathrm{L}}\right|^2 \\ &= 45.0\,\frac{\mu b}{sr\;GeV^2}\left(\frac{10\,GeV^2}{s}\right)^{10}\left(1-\cos^2\theta_{c.m.}\right)^{-4\gamma} \\ &\quad\times\left[1+\rho_1\sqrt{\frac{s}{GeV^2}}\,\cos\phi(s)+\frac{\rho_1^2}{4}\,\frac{s}{GeV^2}\right]F(s,\theta_{c.m.})\ , \quad (4.8)\end{aligned}$$

where $\gamma = 1.6$. The function $F(s,\theta_{c.m.})$ is used to further adjust the phenomenologically motivated parametrization of the experimental data in the range $60^\circ \leq \theta_{c.m.} \leq 90^\circ$ [192].

On a log-log plot, the $pp \to pp$ data fall roughly like s^{-10}, but a closer look reveals that the scaling-law behavior is modulated by oscillations with the logarithm of the energy, as was shown in Fig. 4.3.

4.1.4 Brodsky-de Teramond Picture

Another interpretation of the behavior of the pp cross section and spin-spin correlation was given by Brodsky and de Teramond [145]. In their model, two broad baryon resonances are associated with strange and charmed particle production thresholds at $\sqrt{s} = 2.55$ and 5.08 GeV. The resonances represent normal-sized hadrons and interfere with the small-sized quark-counting amplitude, thereby explaining the anomalous behavior of the pp cross section, the pp spin-spin correlation, and the $A(p,2p)$ transparency. Their idea is supported by the fact that the mass scale of the charm threshold concurs with that of the rapid energy variation

in the spin-spin correlation and nuclear transparency data. In our calculations, we restrict ourselves to the model of Ralston and Pire.

4.2 Nuclear Filtering

Inside the nuclear medium, the normal-sized component (the Landshoff amplitude) is suppressed by the strong interactions with the spectator nucleons, while the small-sized component (the quark-counting amplitude) escapes the nucleus with relatively small attenuation due to CT (see Section 4.3). This phenomenon is called "nuclear filtering" [144, 146, 147]: the nucleus filters away the normal-sized components. Accordingly, the nucleus plays an active role in selecting small-sized components. As a result, the oscillations seen in free pp scattering will be weaker in $A(p,2p)$ reactions.

Incorporating the Ralston-Pire approach and the NF mechanism into the $A(p,2p)$ formalism of Section 2.1, the amplitude for the $p\left(E_{p1},\vec{p}_1,m_{s1i}\right)+A\left(E_A,\vec{k}_A,0^+\right)\rightarrow p\left(E_{k1},\vec{k}_1,m_{s1f}\right)+p\left(E_{k2},\vec{k}_2,m_{s2f}\right)+A-1\left(E_{A-1},\vec{k}_{A-1},J_RM_R\right)$ reaction becomes

$$\begin{aligned}\mathcal{M}_{fi}^{(p,2p)} &= \sum_{m_s}\left(\mathcal{M}_{\mathrm{QC}}^{pp}\right)_{m_{s1i},m_s,m_{s1f},m_{s2f}}\bar{u}(\vec{p}_m,m_s)\,\phi_{\alpha_1}^{\mathrm{RMSGA+CT}}\left(\vec{p}_m\right)\\ &\quad+\sum_{m_s}\left(\mathcal{M}_{\mathrm{L}}^{pp}\right)_{m_{s1i},m_s,m_{s1f},m_{s2f}}\bar{u}(\vec{p}_m,m_s)\,\phi_{\alpha_1}^{\mathrm{RMSGA}}\left(\vec{p}_m\right)\ ,\end{aligned}\tag{4.9}$$

where $\vec{p}_m$ is the missing momentum and α_1 refers to the state wherein the struck proton resided. The distorted momentum-space wave functions $\phi_{\alpha_1}^{\mathrm{RMSGA(+CT)}}\left(\vec{p}_m\right)$ are defined as in Eq. (2.35). The IFSI of the impinging and two outgoing protons are calculated in the RMSGA frameworks of Sections 2.3 and 2.4. Since the quark-counting term is associated with small size, the corresponding momentum-space wave function $\phi_{\alpha_1}^{\mathrm{RMSGA+CT}}\left(\vec{p}_m\right)$ includes the effect of CT. The Landshoff term, on the other hand, corresponds with a hadron of normal size. Consequently, the IFSI can be computed in standard Glauber theory.

Using the spin-averaged pp matrix element of Eq. (4.5), the squared $A(p,2p)$

matrix element for knockout from the α_1 shell can be cast in the form

$$\overline{\sum_{if}}\left|\mathcal{M}_{fi}^{(p,2p)}\right|^2 = \sum_{m,m_s}\Bigg\{\left|\mathcal{M}_{\rm QC}^{pp}\right|^2\left|\bar{u}(\vec{p}_m,m_s)\,\phi_{\alpha_1}^{\rm RMSGA+CT}(\vec{p}_m)\right|^2 + 2Re\Big[\mathcal{M}_{\rm QC}^{pp}\left(\mathcal{M}_{\rm L}^{pp}\right)^*\bar{u}(\vec{p}_m,m_s)\,\phi_{\alpha_1}^{\rm RMSGA+CT}(\vec{p}_m) \times\left(\bar{u}(\vec{p}_m,m_s)\,\phi_{\alpha_1}^{\rm RMSGA}(\vec{p}_m)\right)^*\Big] + \left|\mathcal{M}_{\rm L}^{pp}\right|^2\left|\bar{u}(\vec{p}_m,m_s)\,\phi_{\alpha_1}^{\rm RMSGA}(\vec{p}_m)\right|^2\Bigg\}, \tag{4.10}$$

with m the struck nucleon's generalized angular momentum quantum number. The differential cross section is obtained as an incoherent sum of the squared matrix elements over all proton levels α_1, thereby factoring in the occupation number of every level.

For all the results presented in this chapter, the relativistic bound-state wave function $\phi_{\alpha_1}(\vec{r})$ is computed in the Hartree approximation to the $\sigma-\omega$ model [38], using the W1 parametrization for the different field strengths [193] (see Appendix B). Hereafter, results obtained on the basis of Eq. (4.10) are dubbed RMSGA + CT + NF.

In our numerical calculations, we will also consider the standard RMSGA + CT picture. In this scenario, the entire wave packet of the incoming and outgoing protons is assumed to be in a small-sized configuration, which propagates through a passive nuclear medium. This amounts to neglecting the Landshoff term in the amplitudes $\mathcal{M}^{pp}$ and $\mathcal{M}_{fi}^{(p,2p)}$ of Eqs. (4.5) and (4.9). Finally, in the standard RMSGA calculations, both the Landshoff term and CT effects are neglected.

4.3 Color Transparency

4.3.1 Requirements for CT

The manifestation of the quark-gluon degrees of freedom gives rise to several phenomena in exclusive hadronic reactions. One such prediction of QCD is color transparency [122, 123]. The basic idea of CT is that hadrons, which interact very strongly with the nuclear medium under normal circumstances, form small objects (so-called point-like configurations, or PLCs) that move through nuclear matter al-

most undisturbed. So, while NF uses the nuclear medium actively, in CT large momentum transfer selects short-distance objects and the nucleus functions as a passive medium for the passage of the PLCs. The physics of CT is based on three ideas [194–197]:

(i) Small objects are produced in high-momentum-transfer reactions

As can be seen in Fig. 2.4, the nucleon-nucleon interaction becomes predominantly inelastic at high energies. Consequently, a nucleon struck by a highly energetic particle (hadron, lepton, ...) is expected to scatter into the inelastic channels. However, due to the association of high momentum transfer with small wavelengths, the impinging particle can probe the subnucleonic degrees of freedom. Suppose now that the incoming particle hits one of the confined colored quarks. The excited quark becomes off-shell with an energy surplus of $\delta E \sim \omega$ and will decay with a lifetime $\tau \sim 1/\omega$ by emitting gluons. Owing to quark confinement, two things can happen: the colored quark hadronizes or it recombines with its two companion quarks. In order for the second option to take place, the quarks must have been close together initially. The radiated gluons must be absorbed by quarks which were at most a distance $r \sim 1/\omega$ away from the off-shell quark. This implies that the struck nucleon must have been in a small-sized fluctuation or point-like configuration.

QCD lattice calculations indicate that hadrons are bound states of strongly interacting quarks and gluons. Each hadron can be characterized in terms of an infinite number of configurations, e.g., $|qqq\rangle$, $|qqq + \pi\rangle$, ... with varying sizes. A quantum system fluctuates between its different configurations. Hence, "snapshots" of a hadron taken at different times would disclose both small- and large-sized configurations, a phenomenon referred to as color fluctuations. On the basis of the uncertainty principle, the time scale for fluctuations can be estimated to be inversely proportional to the mass difference of the two configurations: $\tau \sim 1/(m - M)$. The relevant mass differences are typically of the order of hundreds of MeV, so the fluctuation time is of the order of 1 fm/c.

(ii) Small objects experience reduced interactions

The second requirement on which the existence of CT depends, is that a small object interacts in an anomalously weak manner with the surrounding nuclear medium.

This phenomenon of color neutrality or color screening is the QCD analogue of the charge screening effect in QED and arises naturally from a two-gluon-exchange model between color singlets [198–200]. As gluons carry color, single gluon exchange is forbidden. A small object has a small color dipole moment and interacts with nuclear matter in a much weaker way than a normal-sized object. In this respect, the force between two color singlets can be regarded as a "color Van der Waals force".

(iii) Small objects can be considered as frozen while traversing the nuclear medium

A PLC is not a stationary eigenstate of the QCD Hamiltonian, but a superposition of eigenstates. As such, it is subject to time evolution, leading to an increase of its transverse size and the restoration of soft quark-gluon fields [148, 201]. Suppose a hadron with a large laboratory momentum p fluctuates from a PLC with bare mass M to a normal-sized hadron with ground-state mass m. The energy difference between both configurations is given by $\sqrt{p^2+M^2}-\sqrt{p^2+m^2} \approx (M^2-m^2)/2p$. Therefore, the expanding PLC can propagate for a distance

$$l_h \simeq \frac{2p}{M^2-m^2} \ , \tag{4.11}$$

the so-called hadronic expansion length or coherence length, before reaching its normal hadronic size. This length increases with hadron momentum p and is inversely proportional to the squared mass difference ΔM^2 between the intermediate PLC and the normal-sized hadron. The bare mass M of the PLC is an undetermined parameter, but it is commonly assumed that $0.7 \leq \Delta M^2 \leq 1.1$ (GeV/c^2)^2 are reasonable values.

It is clear that the condition for full CT to occur, $l_h \gg R_A$ (with R_A the nuclear radius), will not be fulfilled for the present experimental kinematics. The PLCs expand and the IFSI are not completely suppressed. Consequently, the physical picture of the $A(p,2p)$ reaction with CT can be described as follows: The impinging proton compresses to a PLC as it hits a target nucleon, after which the outgoing protons expand from PLCs to normal-sized objects as they move through the nucleus. A schematic representation of this CT picture is given in Fig. 4.5. Here, it should be noted that PLCs are only formed in scattering via the quark-counting mechanism, where the exchange of hard gluons (see Fig. 4.2) brings the quarks inside

the hadrons close together. The Landshoff scattering does not possess this feature, since the hard gluon exchange is between the quarks of the different protons (see Fig. 4.4), which only makes the interaction region small.

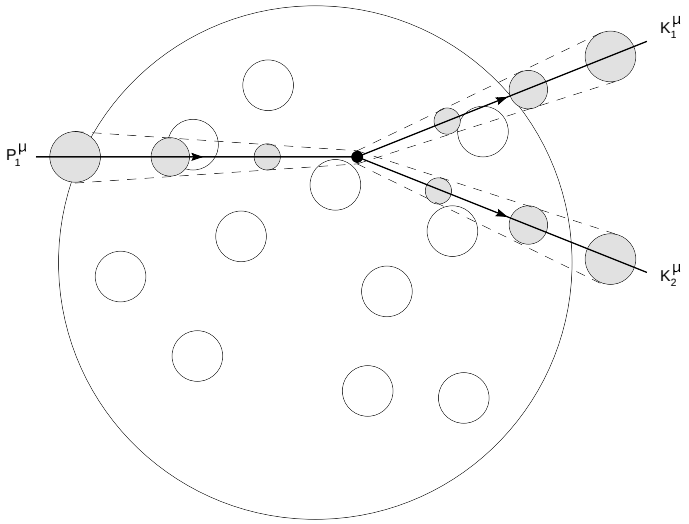

Figure 4.5 Schematic representation of the CT phenomenon in the $A(p, 2p)$ reaction. The incoming proton is compressed to a PLC before hitting a target proton. The outgoing protons are produced as PLCs but expand as they move through the nucleus.

4.3.2 Quantum Diffusion Model of Farrar *et al.*

To account for the reduced interaction of a PLC with the nuclear medium, the total cross sections $\sigma_{pN}^{\rm tot}$ in Eqs. (2.64) and (2.81) are replaced by effective ones. As suggested for pQCD by [198], the effective cross section $\sigma_{pN}^{\rm eff}$ is simply scaled by the transverse size of the PLC relative to the average size of a regular nucleon:

$$\sigma_{pN}^{\rm eff} = \frac{r_t^2}{\langle r_t^2 \rangle}\, \sigma_{pN}^{\rm tot} \text{ for } r_t^2 < \langle r_t^2 \rangle \,. \tag{4.12}$$

Here, r_t is the transverse radius of the PLC and $\langle r_t^2 \rangle^{1/2}$ is the rms transverse radius of a regular nucleon. It is assumed that the quarks in the PLC occupy a transverse area of $r_t^2 \simeq \frac{\langle n^2 k_t^2 \rangle}{Q^2} \langle r_t^2 \rangle$ at the point of interaction, where $Q^2 = |t|$ is the four-momentum transfer, $n = 3$ is the number of constituents in the nucleon, and $\langle k_t^2 \rangle^{1/2} = 0.35$ GeV/c is the average transverse momentum of a parton in a hadron.

This assumption agrees with the Q^2 dependence of the transverse size of the nucleon found in the realistic models of the nucleon form factor [202].

In the partonic model of Farrar *et al.* [148] (denoted by FLFS), two models are considered to find the dependence of r_t on Z, the distance from the hard interaction point along the trajectory of the particle. In the naive quark expansion picture, the partons fly apart at the velocity of light, so that $r_t \sim (E/m)^{-1}Z$, with E/m the time dilatation factor. The hadronic expansion length is then determined by the Lorentz boost, $l_h \simeq (E/m)(\sigma_{pN}^{\rm tot}/\pi)^{1/2}$. The alternate scenario follows from an analysis of pQCD Feynman diagrams [201, 203], but this behavior is rather generically called quantum diffusion. Considering the asymptotically most important energy denominator in these diagrams leads to $r_t \sim Z^{1/2}$. The hadronic expansion length is determined by the average value of the dominant energy denominator: $l_h \simeq \langle 1/(E_{\rm PLC} - E)\rangle \simeq 2p/\Delta M^2$ (see Eq. (4.11)), where $E_{\rm PLC}$ and E are the energy of the intermediate PLC and the normal-sized hadron, respectively.

Based on the above reasoning, the interaction cross section is argued to be

$$\sigma_{pN}^{\rm FLFS}(p,Z) = \sigma_{pN}^{\rm tot}\left(\left\{\left(\frac{Z}{l_h}\right)^{\tau} + \frac{\langle n^2 k_t^2\rangle}{|t|}\left[1-\left(\frac{Z}{l_h}\right)^{\tau}\right]\right\}\theta(l_h - Z) + \theta(Z - l_h)\right)\,, \quad (4.13)$$

where $\tau = 1$ corresponds to the quantum diffusion picture and $\tau = 2$ to the naive quark expansion case. In this work, we shall present results only for the quantum diffusion model, $\tau = 1$. The merit of this approach is its simplicity and physical motivations. It is, however, nothing more than an educated guess, a semiclassical geometrical expansion model.

4.3.3 Hadronic Expansion Model of Jennings and Miller

An alternative perspective on CT was provided by the hadronic picture of Jennings and Miller (JM) [149]. Their approach is completely quantum mechanical and avoids the use of semiclassical approximations. Using hadronic degrees of freedom, they suggested the following expression for the effective cross section

$$\sigma_{pN}^{\rm JM}(p,Z) = \sigma_{pN}^{\rm tot}\left(1 - \frac{p}{p^*}\, e^{i(p-p^*)Z}\right)\,, \quad (4.14)$$

with p the proton momentum and p^* the momentum of a baryon resonance with a complex mass M^* and the same energy as the nucleon, i.e., $(p^*)^2 = p^2 + M_p^2 - (M^*)^2$. The expression for the effective cross section emanates from the intermediate PLC

being a superposition of the nucleon ground state and a nucleon resonance. The imaginary part of M^* ensures the decay of the intermediate state to an asymptotically free, normal-sized proton. Later, Jennings and Miller developed a more sophisticated approach [204], where the intermediate PLC is expanded in a complete set of hadronic states. This treatment uses experimentally measured matrix elements for deep inelastic scattering and diffractive dissociation to compute the effective cross section, thereby reducing the model dependence. In this work, however, we restrict ourselves to the simple model of Eq. (4.14). Like the FLFS approach of Eq. (4.13), it considers one excited state in the PLC.

It is worth noting that both the FLFS and JM model take into account the suppression of interaction in the collision point and the time evolution of the PLC to a normal-sized proton during its propagation through the nucleus. This can be appreciated from the Z dependence of the real part of the effective cross section shown in Fig. 4.6. The area below the curve is a measure for the strength of the CT effect: the smaller this area, the more transparent the nuclear medium. The $Z = 0$ intercept shows that in the FLFS model the reduction in cross section is not complete at the collision point, $\sigma_{pN}^{\mathrm{FLFS}}(Z = 0)$ goes like $1/Q^2$. The FLFS effective cross section then rises linearly up to $\sigma_{pN}^{\mathrm{tot}}$ representing the expansion of the PLC. As mentioned before, the Z value at which this asymptotic value is reached, l_h, depends on the proton momentum p and the parameter ΔM^2. In the JM model, the real part of the effective cross section increases from zero at the interaction point, then overshoots the total pN cross section and oscillates about this value. This oscillating behavior dies out with increasing Z and $\mathrm{Re}\,\sigma_{pN}^{\mathrm{JM}}$ approaches $\sigma_{pN}^{\mathrm{tot}}$ asymptotically. Likewise, the imaginary part of $\sigma_{pN}^{\mathrm{JM}}$ exhibits a damped oscillation around 0. The initial increase of $\mathrm{Re}\,\sigma_{pN}^{\mathrm{JM}}$ with Z is determined by the real part of the parameter M^*: the larger $\mathrm{Re}\,M^*$, the sharper the increase. The imaginary part of M^*, on the other hand, has an effect on the size of the oscillations of the effective cross section $\sigma_{pN}^{\mathrm{JM}}$ around the asymptotic value, with small values for the imaginary part leading to large oscillations.

4.3.4 Effect of CT on the IFSI Factor

In Fig. 4.7 the absolute value of the IFSI factor is shown for two values of the incoming beam momentum p_1 as a function of the (x, z) coordinate of the hard collision

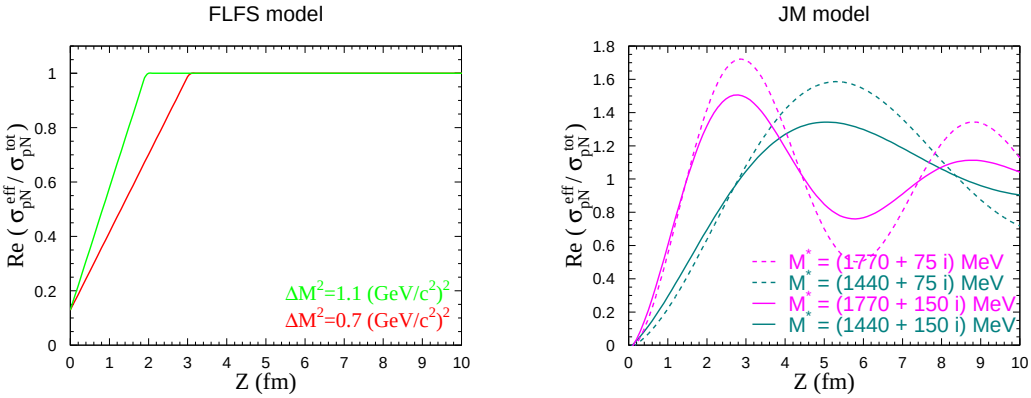

Figure 4.6 The real part of $\sigma_{pN}^{\rm eff}/\sigma_{pN}^{\rm tot}$ as a function of the distance Z from the hard interaction point at $p \simeq 5.4$ GeV/c and $|t| \simeq 8.5$ (GeV/c)^2. The left panel shows the Z dependence of the effective cross section in the FLFS model, while the right panel displays the results of the JM model.

point. The absolute value of the IFSI factor is a measure for the total absorption due to the incoming and outgoing protons. The kinematics is chosen such that the c.m. scattering angle for the elementary hard pp scattering is $90°$. Accordingly, the pair of final-state protons is produced at equal momenta, equal polar angles, and opposite azimuthal angles in the laboratory frame. The scattering angles of the two final-state protons become smaller as the incident beam energy increases for a fixed c.m. scattering angle. At $p_1 = 5.9$ GeV/c, the outgoing protons have momenta $k_1 = k_2 = 3.3$ GeV/c and scattering angles $\theta_1 = \theta_2 = 27.5°$; while at $p_1 = 14.4$ GeV/c, the kinematics is $k_1 = k_2 = 7.6$ GeV/c and $\theta_1 = \theta_2 = 19.3°$. The standard RMSGA results are compared with the RMSGA + CT predictions of the FLFS model using $\Delta M^2 = 0.7$ (GeV/c^2)^2.

The RMSGA results show that the effect of IFSI is mostly constrained to low impact parameter $|x|$, i.e., trajectories that pass through the dense nuclear interior. The overall behavior of the IFSI factor in the RMSGA approach is very similar for both incoming momenta. After all, the attenuation effect is controlled by the total pN cross section $\sigma_{pN}^{\rm tot}$ which, at the high energies in question, is almost constant (see Fig. 2.4). The main difference between both kinematics is in the scattering angles

$\theta_1 = \theta_2$, i.e., it is purely geometrical. This causes the dissimilarities between the $p_1 = 5.9$ GeV/c and $p_1 = 14.4$ GeV/c IFSI factors in the backward hemisphere ($z < 0$), where the FSI effects are largest. Turning to CT, its effect is particularly prominent for hard interaction points that are located near the center of the nucleus. For these points, the region where the protons are in PLCs (i.e., where the interaction with the nuclear medium is most reduced) coincides with the part of the nucleus where the spectator nucleons are most abundant.

4.3.5 Nuclear Color Screening Effect

To complete the discussion on CT, we mention the nuclear color screening effect (NCSE) [203, 205]. In this QCD effect, the binding of the nucleonic system results in a reduced PLC probability. Since the potential for the interaction of a bound nucleon in a PLC with nearby nucleons is smaller than for a normal-sized nucleon, the creation of a PLC gives rise to smaller binding energies. This is not preferable energywise and leads to the suppression of the nucleon's PLC component. This suppression can be included in the calcutions by multiplying the CT cross section by the factor

$$\delta k = \theta(Q_0^2 - Q^2) + \theta(Q^2 - Q_0^2)\left[1 + \left(1 - \frac{Q_0^2}{Q^2}\right)\frac{\frac{k^2}{M_p} + 2\epsilon_A}{\Delta E}\right]^{-2} . \tag{4.15}$$

Here, $Q^2 = |t|$ is the four-momentum transfer, k is the bound nucleon's momentum, and $\epsilon_A \simeq 8$ MeV is the average binding energy per nucleon. For the parameter ΔE, we will take a value of 0.6 GeV, while an analysis of the ^{2}He(e, e') SLAC data in Ref. [203] indicates that $Q_0^2 \simeq 2$ (GeV/c)^2.

4.4 Nuclear Transparency Results

Experimentally, the nuclear transparency is defined as the ratio of the cross section for quasielastic scattering from the protons in the nucleus to the cross section for free pp scattering corrected for the number of protons in the nucleus Z:

$$T = \frac{\sigma\,(pp\,\text{quasielastic in nucleus})}{Z\,\sigma\,(pp\,\text{elastic in hydrogen})} . \tag{4.16}$$

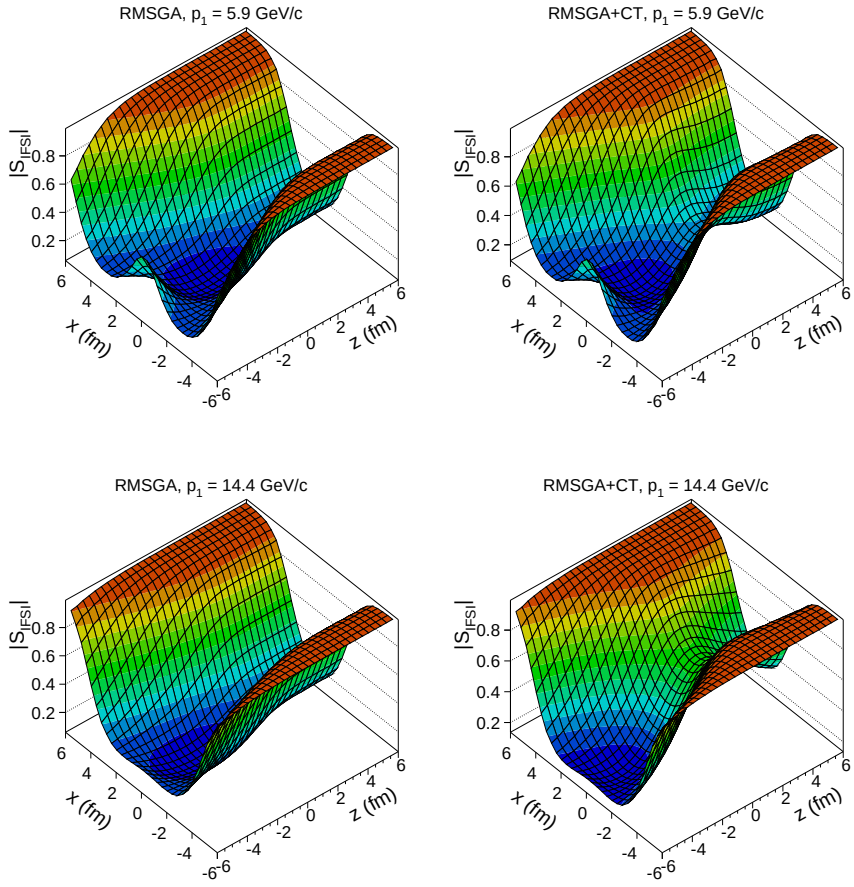

Figure 4.7 The (x, z) dependence of the absolute value of the IFSI factor $\mathcal{S}_{\rm IFSI}$ in the RMSGA (left panels) and RMSGA + CT picture (right panels). (x, z) is the coordinate of the hard collision point in the scattering plane with the z axis lying along the incoming momentum $\vec{p}_1$. In the CT calculations, the FLFS model of Eq. (4.13) with $\Delta M^2 = 0.7$ (GeV/c^2)^2 was employed. The upper (lower) panels correspond to an incoming momentum of 5.9 GeV/c (14.4 GeV/c). The kinematics of the outgoing protons is in-plane and symmetric, defined by 90° pp scattering in the pp c.m. frame.

In our calculations, the nuclear transparency is computed as the ratio of the $A(p, 2p)$ cross sections including and excluding IFSI effects:

$$T = \frac{\sigma^{(p,2p)}}{\sigma^{(p,2p)}_{\rm RPWIA}} \, . \tag{4.17}$$

The RPWIA limit is reached by setting the IFSI operator $\widehat{\mathcal{S}}_{\rm IFSI}^{\rm RMSGA(+CT)}(\vec{r})$ equal to one in Eq. (4.10) and as such the free pp cross section is recovered in the denominator. The numerator and denominator of Eq. (4.17) are obtained by integrating the corresponding differential cross sections over the phase space defined by the kinematic cuts. In our calculations, we adopted identical cuts as in the experiments [124–126] and assumed a flat experimental acceptance within the kinematical ranges for each data point. These experimental cuts, which are applied to extract the quasielastic events from the background, constrain the values of p_{m_x}, p_{m_y}, α_0, and $\theta_{\rm c.m.}$. Here, the z direction is defined to coincide with the incident beam direction, so p_{m_x} and p_{m_y} are the transverse components of the missing momentum. The variable

$$\alpha_0 \equiv 1 - \frac{\sqrt{(E_{p1}+M_p)^2 - 4M_p^2}\cos\left(\frac{\theta_1-\theta_2}{2}\right)\cos\left(\frac{\theta_1+\theta_2}{2}\right) - p_1}{M_p}\,, \tag{4.18}$$

is an approximation to $\alpha \equiv A\frac{E_m - p_{m_z}}{M_A}$, the longitudinal light-cone momentum fraction carried by the struck proton [206]. The range of the c.m. scattering angle extends from 80° to 90° for the E834 experiment by Carroll *et al.* [124], while the sequel E850 experiment [125, 126] covers the region $86^\circ \lesssim \theta_{\rm c.m.} \lesssim 90^\circ$. The c.m. scattering angle can be determined directly by transforming the outgoing particle momentum to the c.m. frame and calculating its dot product with the beam momentum. Unfortunately, this procedure generates a result with unsatisfactory resolution. Therefore, $\theta_{\rm c.m.}$ is calculated using the approximate relation [206]

$$\cos\theta_{\rm c.m.} = \frac{2p_1\sqrt{(E_{p1}+M_p)^2 - 4M_p^2}\sin\left(\frac{\theta_1-\theta_2}{2}\right)\sin\left(\frac{\theta_1+\theta_2}{2}\right)}{s - 4M_p^2}\,. \tag{4.19}$$

For fixed beam energy E_{p1}, α_0 and $\theta_{\rm c.m.}$ depend mainly on the sum and difference of the polar angles θ_1 and θ_2 of the outgoing nucleons, respectively. The introduction of the approximations (4.18) and (4.19) turned out to be essential to interpret the experiments, as they significantly improved the resolution.

We consider the experimental nuclear transparency values as presented in [207]. The incident lab momentum varies from 5.9 to 14.4 GeV/c and the scattering angle is near 90° in the pp center of mass. The Mandelstam variable $|t| \simeq \left(s - 4M_p^2\right)/2$ extends from 4.7 to 12.7 (GeV/c)^2. In Ref. [207], the originally published values of

Carroll *et al.* [124] were rescaled using the improved nuclear momentum distributions of Ref. [208], thereby making them consistent with the data of Refs. [125,126].

First, we address the energy dependence of the ^{12}C$(p,2p)$ transparency and study the role of IFSI, CT, and NF. Further, we use the ^{12}C$(p,2p)$ calculations as a test case to determine the accuracy of the IFSI operator of Eq. (2.81) relative to the expression of Eq. (2.74). Fig. 4.8 displays the ^{12}C transparency as a function of the incoming proton momentum p_1. The solid curves represent the full RMSGA calculations, whereas the RMSGA′ results are shown as dashed curves. Three different scenarios were considered. As expected, the standard RMSGA calculations lead to a nuclear transparency that is almost independent of the beam momentum. The main effect of the IFSI is to reduce the nuclear transparency from the asymptotic value of 1 to ~ 0.15. The inclusion of CT effects produces a transparency linearly rising with energy. The increase relative to the RMSGA result is highly dependent on the adopted model and corresponding parameters for CT. The curves including CT shown in Fig. 4.8 adopt the FLFS model with $\Delta M^2 = 0.7$ (GeV/c^2)^2. The increase of the transparency is consistent with the data in the range 5–10 GeV/c, but the RMSGA + CT picture fails to explain the drop in the transparency at higher momenta. Our RMSGA and RMSGA + CT predictions confirm the results of [209]. A better agreement with the data is obtained when adding the mechanism of NF. Compared to the RMSGA + CT results, the transparency is increased at intermediate momenta (5–10 GeV/c) and decreased at higher momenta, two effects which improve the description of the data. A similar result was obtained in Ref. [210] where the JM model of CT was used.

Concerning the comparison of the RMSGA and RMSGA′ results, it can be inferred from Fig. 4.8 that both approaches yield nearly identical results which differ at the 2–3% level. Consequently, the operator of Eq. (2.81) is considered sufficiently accurate for the calculation of the nuclear transparency and will be used in the remainder of this work. We wish to stress that the computational cost of Eq. (2.81) is about a factor of 10^3 lower than the full-blown RMSGA operator of Eq. (2.74).

Figs. 4.9 and 4.10 are devoted to a comparison of the different CT models. Results of the FLFS quantum diffusion model are plotted for $\Delta M^2 = 0.7$ and 1.1 (GeV/c^2)^2. For the M^* parameter of the JM model we consider three different values, representing the Δ, the Roper resonance, and the average of the lowest

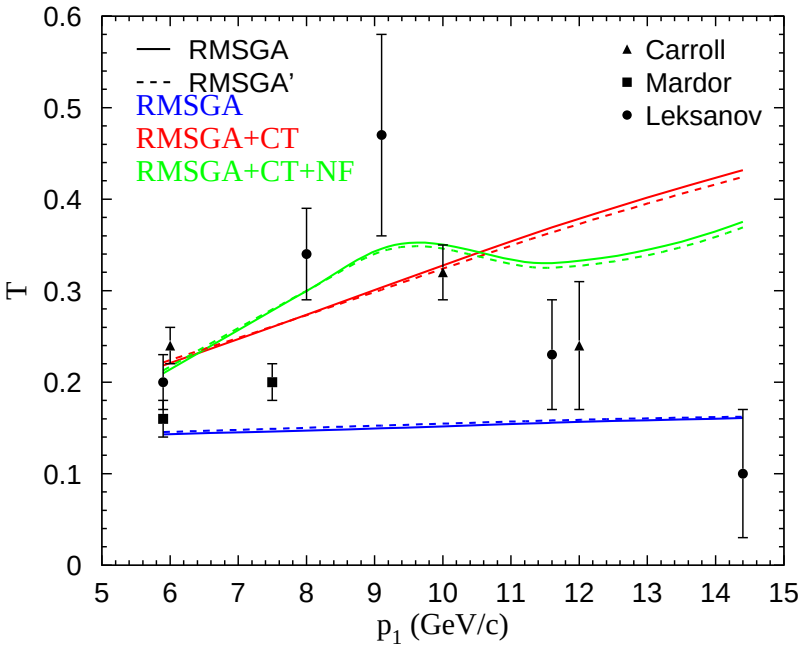

Figure 4.8 The nuclear transparency for the ^{12}C$(p, 2p)$ reaction as a function of the incoming lab momentum p_1. The full RMSGA (solid lines) are compared to the RMSGA′ (dashed lines) results. The different curves represent the RMSGA, RMSGA + CT and RMSGA + CT + NF calculations. The CT effects are calculated in the FLFS model [148] with $\Delta M^2 = 0.7$ (GeV/c^2)^2 and the results including the mechanism of NF are obtained using the positive sign of $\phi(s) + \delta_1$. Data are from Refs. [124] (solid triangles), [125] (solid squares), and [126] (solid circles).

P-wave N^* resonances. For the imaginary part of M^* a value of 150 MeV was taken. The lowest values of the parameters ΔM^2 and M^* induce the strongest increase of the RMSGA + CT transparency with the beam momentum p_1 and also lead to the largest deviations between the predictions including the NF mechanism and the corresponding RMSGA + CT results.

Fig. 4.9 shows that after including NF and CT, the calculations correctly reproduce the maximum in the ^{12}C$(p, 2p)$ transparency at about 9.5 GeV/c, but badly fail to fall back low enough to account for the 14.4 GeV/c data point. Ralston and Pire [144], on the other hand, do succeed in reproducing the maxima and minima in the nuclear transparency data. However, they assume that the transparency of the quark-counting term is beam-energy independent, a rather speculative as-

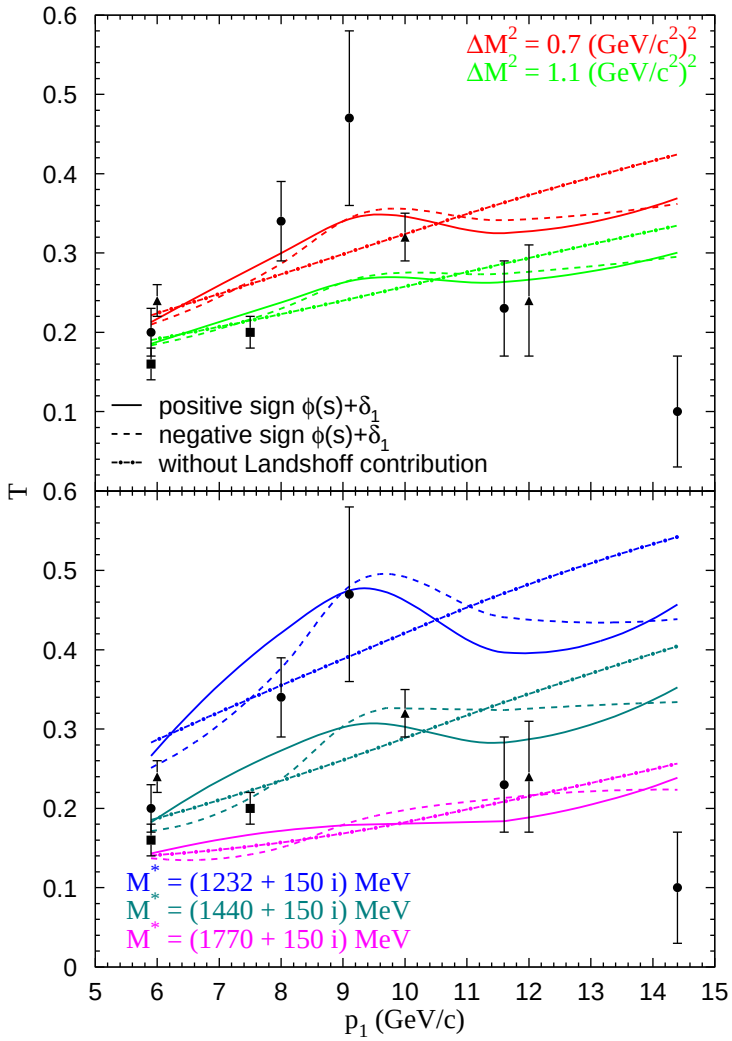

Figure 4.9 The ^{12}C$(p, 2p)$ transparency versus the incoming lab momentum p_1. The upper (lower) panel depicts results using the FLFS (JM) model for CT. Calculations including the effects of CT and NF with the positive (solid lines) and negative (dashed lines) sign for $\phi(s) + \delta_1$ are shown, along with the RMSGA + CT predictions (dot-dashed lines). Data are from Refs. [124] (solid triangles), [125] (solid squares), and [126] (solid circles).

sumption. The CT-induced increase of the quark-counting transparency with energy causes our RMSGA + CT + NF predictions to rise again at a momentum $p_1 \simeq 12\,\mathrm{GeV/c}$.

In the FLFS as well as the JM approach, the RMSGA + CT + NF predictions

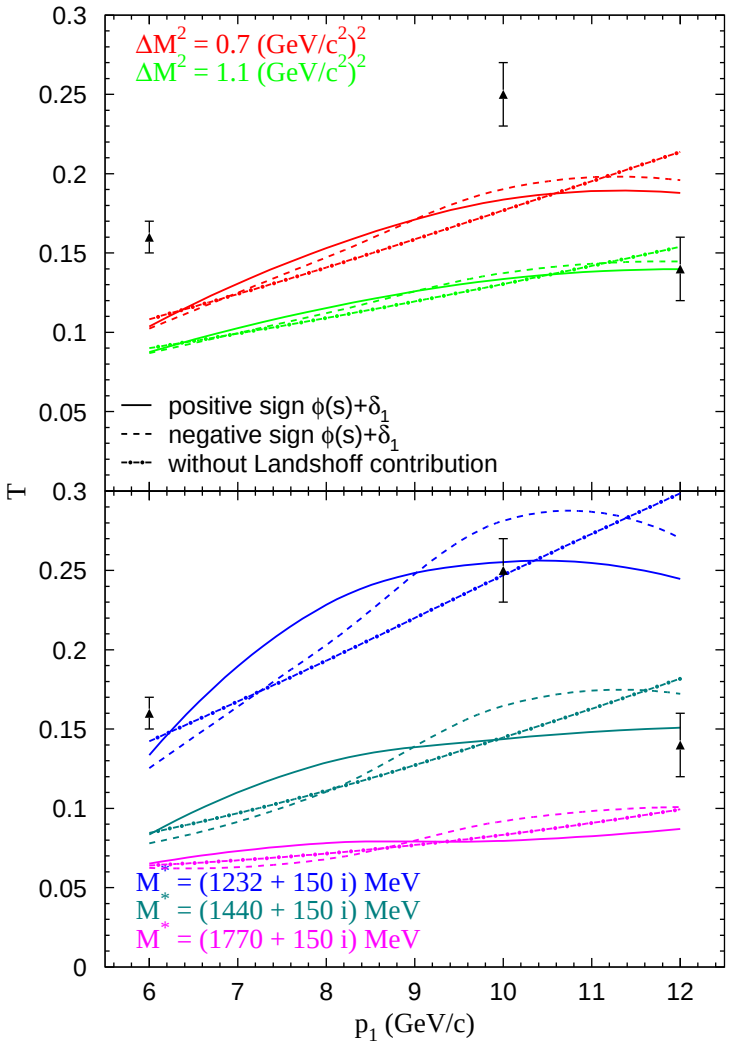

Figure 4.10 As in Fig. 4.9, but for ^{27}Al. Data are from Ref. [124].

reproduce the general trend of the data, but no variant achieves very good agreement. Furthermore, it is not possible to unambiguously determine the value of the parameters ΔM^2 and M^*, as the best choice for these parameters depends on the target nucleus under consideration. Fig. 4.9 suggests that for the ^{12}C$(p, 2p)$ reaction $M^* = (1440 + 150\,i)$ MeV leads to the best agreement, while for the ΔM^2 parameter no "best" choice can be put forward. Fig. 4.10, on the other hand, shows that for the ^{27}Al target nucleus the FLFS results are systematically below the data in the

region below 10 GeV/c. Using $M^* = (1440 + 150\,i)$ MeV in the JM model also does not increase the transparency high enough so as to match the 6 and 10 GeV/c data points, only with $M^* = (1232 + 150\,i)$ MeV is the CT-induced increase of the transparency strong enough.

Another effect that can be studied in Figs. 4.9 and 4.10 is the influence of the sign of $\phi\,(s) + \delta_1$ on the RMSGA + CT + NF results. For the FLFS model of CT, the differences between calculations using both signs of $\phi\,(s) + \delta_1$ are minor. As already observed by Jennings and Miller [210], the results using the JM model of CT are rather sensitive to this sign. The discrepancy between the FLFS- and JM-based calculations arises from the different structure of the effective cross sections (4.13) and (4.14). Indeed, these effective cross sections not only determine the attenuation of the quark-counting term in the nuclear medium, but also the phase difference between the quark-counting and the Landshoff term. Whereas the real parts of both effective cross sections are quite similar (see Fig. 4.6), the FLFS effective cross section (4.13) is purely real, while its JM counterpart has an imaginary part as well. This imaginary part causes the enhanced sensitivity of the JM results to the sign of $\phi\,(s) + \delta_1$. As for which sign causes the best agreement with the data, no firm conclusions can be drawn. Indeed, the optimum choice for the sign of $\phi\,(s) + \delta_1$ depends on the used CT model (FLFS or JM), the value of the parameter ΔM^2 or M^*, and the target nucleus. For the ^{7}Li$(p, 2p)$ reaction, the positive sign provides the best agreement, while the ^{63}Cu transparency data rather require a negative sign.

None of the results shown in this section include the nuclear color screening effect of Section 4.3.5. We deem that the CT parameters are so badly constrained that controlling additional mechanisms is out of reach for the moment. In both the RMSGA + CT and the RMSGA + CT + NF calculations, the inclusion of the NCSE decreases the transparency by 6–12%, with the largest effect occuring at higher p_1. Another additional effect that is not included here are the NN short-range correlations (SRC). It should be noted that the SRC and CT both lead to a suppression of the absorptive interaction close to the hard collision point and therefore are in some sense competing mechanisms. However, the effects stemming from SRC are independent of energy, and, hence, can be disentangled from the pure CT effects. The SRC were found to increase the standard distorted-wave $A(p, 2p)$ transparency (i.e., without CT or NF taken into account) by about 30%, without changing the

energy dependence [209, 211].

Studying the A dependence of the experimental nuclear transparency is a very efficient tool to search for CT effects. Indeed, a change in the shape of the A dependence with increasing incoming momentum could indicate the onset of CT, with complete CT corresponding to a vanishing A dependence. The A dependence of the nuclear transparency at two values of the incoming momentum p_1 is studied in Fig. 4.11. The standard RMSGA calculations fall considerably below the data. Further, none of the RMSGA + CT + NF calculations succeed in simultaneously describing the data for all target nuclei. While the FLFS approach agrees with the ^{7}Li and ^{12}C data points rather well using $\Delta M^2 = 0.7$ (GeV/c^2)^2, the FLFS results tend to underestimate the ^{27}Al and ^{63}Cu data. With regard to the M^* parameter of the JM model, for the ^{7}Li and ^{12}C nuclei a value of $M^* = (1440 + 150\,i)$ MeV seems acceptable, whereas the heavier ^{27}Al and ^{63}Cu nuclei need a smaller M^* value. A general feature of the RMSGA + CT + NF predictions is that their A dependence is steeper than the data. The RMSGA calculations of the $A(e, e'p)$ transparency by our research group [87] also display this characteristic of overestimating the measured A dependence. Finally, the dot-dashed and dotted curves indicate that the 6 GeV/c data are proportional to $A^{-2/3}$; while at 10 GeV/c, the A dependence of the data is more gradual ($T \propto A^{-1/3}$). This trend could point to the onset of CT and is not reproduced by the standard RMSGA predictions, which are almost independent of the incoming momentum. When CT and NF effects are included, the softening of the A dependence with increasing incoming momentum is also present in the calculations, albeit not as pronounced as in the data. For example, the FLFS calculations with $\Delta M^2 = 0.7$ (GeV/c^2)^2 correspond to $T \propto A^{-0.83}$ at 6 GeV/c incoming momentum and $T \propto A^{-0.70}$ at 10 GeV/c.

4.5 Outlook

To conclude this chapter, we present some closing remarks and point out some suggestions for further research.

Introducing the concept of nuclear filtering, our calculations can be brought in qualitative agreement with the $A(p, 2p)$ transparency data, thereby confirming earlier calculations [204, 210, 212]. We wish to stress that CT is imperative to increase the predicted transparencies to the level of the data. A similar conclusion

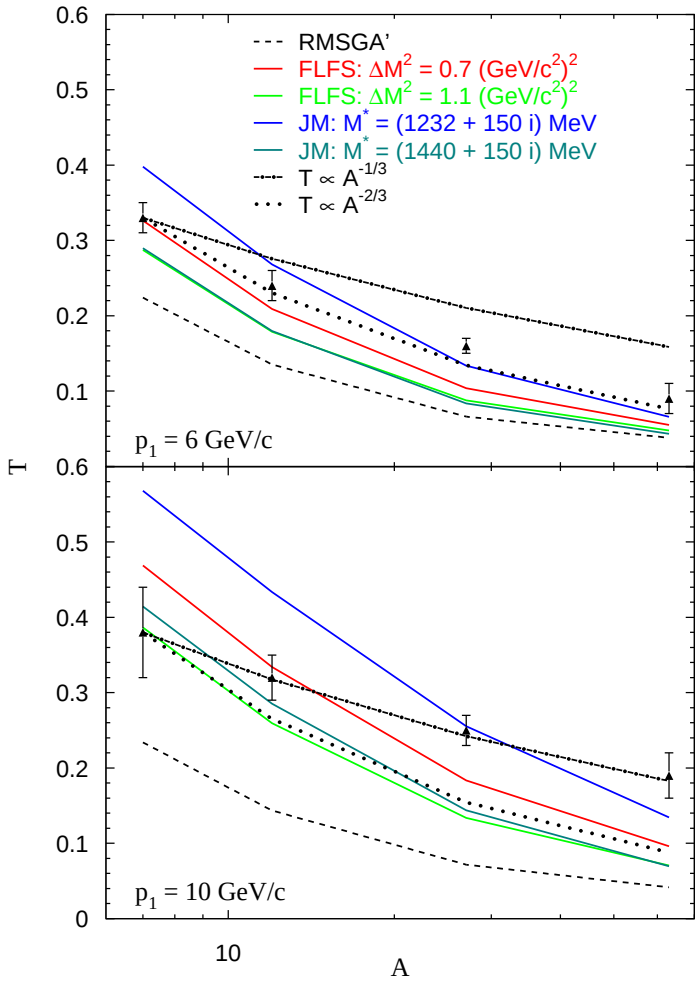

Figure 4.11 A dependence of the nuclear transparency at two values of the incoming lab momentum p_1. The standard RMSGA calculations are represented by dashed curves, while the solid curves are RMSGA + CT + NF calculations with the positive sign for $\phi(s) + \delta_1$. The solid curves correspond with different descriptions of the CT effects, as indicated by the legend. The dot-dashed (dotted) curves display the $A^{-1/3}$ ($A^{-2/3}$) parametrization, normalized to the ^{7}Li data points. Data are from Ref. [124].

was drawn in Refs. [212, 213]. The quantitative description of the data, however, is far from perfect and it is not possible to constrain the magnitude of the parameters in the CT models. More specifically, the oscillations seem to be more outspoken in the data than in the calculations. This is because including the non-zero absorption

of the expanding PLC and the non-complete absorption of the normal-sized proton tends to make the two terms similar and weakens the interference effects.

The indications for CT in $A(p, 2p)$ reactions are not necessarily in contradiction with the results from $A(e, e'p)$ experiments. Although the $A(e, e'p)$ transparencies exhibit no significant increase with the four-momentum transfer Q^2 [214–218] and can be reasonably reproduced in the RMSGA framework [87], the existence of CT can not be excluded since the predicted effect is small [197, 219–221]. The calculations of Lava [221] are depicted in Fig. 4.12 and show that there is indeed no conclusive evidence for the onset of CT in $A(e, e'p)$ reactions. The smallness of the CT effect in the $A(e, e'p)$ experiments is caused by the short expansion times of the PLC to normal size at the present kinematics. The effect of CT is more pronounced in the $A(p, 2p)$ transparency for different reasons. First, in the $A(p, 2p)$ reaction there are three particles that can experience CT instead of only one in $A(e, e'p)$ reactions. Second, $A(p, 2p)$ data are available up to $Q^2 = |t|$ values of 12.7 (GeV/c)^2, while $A(e, e'p)$ transparency experiments are restricted to $Q^2 \lesssim 8$ (GeV/c)^2.

Despite the fact that CT is expected to reveal itself more rapidly in the $A(p, 2p)$ reaction, there are some disadvantages. The free pp scattering data show oscillations which are rather clear evidence for quantum mechanical interference of two amplitudes. For the pp scattering inside the nucleus, however, the oscillations are much reduced. An indication for this is the correlation between the increases in the transparency ratio and the decreases in the free-space data, and vice versa. Furthermore, a plot of the nuclear differential cross section multiplied by the overall power-law factor s^{10} shows a reasonably flat s dependence (see Ref. [224] and Fig. 4.13). These observations support the idea that pp scattering inside the nuclear medium differs from free pp scattering. Hence, the experimentally attractive transparency ratio is not a reliable observable to measure CT on its own. Indeed, the experimental nuclear transparency is not a pure survival probability, but also reflects the effect of the nuclear medium on the underlying hard wide-angle scattering. In other words, the NF effect obscures the observation of CT.

A number of uncertainties involving the $A(p, 2p)$ transparency remain. One subject of discussion is the size of the Landshoff term. According to Botts *et al.* [185, 186, 225–227], this term might also be small-sized. This would bring the survival probability of the Landshoff and the quark-counting term closer together

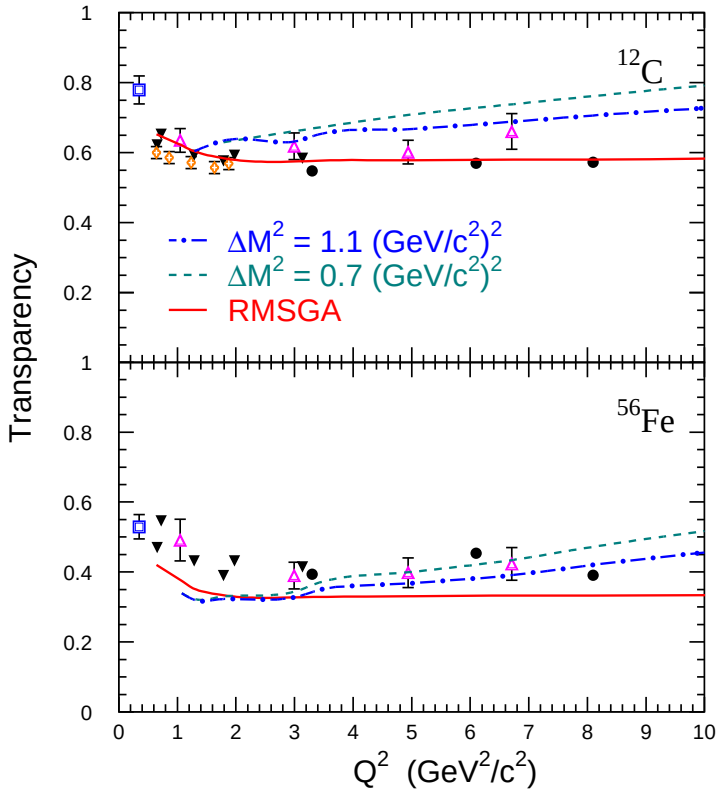

Figure 4.12 The $A(e,e'p)$ nuclear transparency versus Q^2 in quasielastic kinematics. The upper (lower) panel displays the results for ^{12}C (^{56}Fe). The solid line shows the standard RMSGA results. The dashed (dot-dashed) curves account for the effect of CT in the FLFS model with $\Delta M^2 = 0.7\ (1.1)$ (GeV/c^2)^2. Data are from Refs. [222] (open squares), [214,215] (open triangles), [217] (solid circles), [216,218] (solid triangles), and [223] (open diamonds). This figure is taken from Ref. [221].

and would further weaken the oscillations in the energy dependence of the computed transparencies, an effect that the data do not seem to support. It might also be of interest to examine the influence of the helicity-nonconserving amplitudes on the $A(p,2p)$ transparency. Recently, it was shown that including the helicity-nonconserving amplitudes and their interference with the Landshoff amplitude leads to a better description of the pp elastic scattering cross section and spin correlation [228].

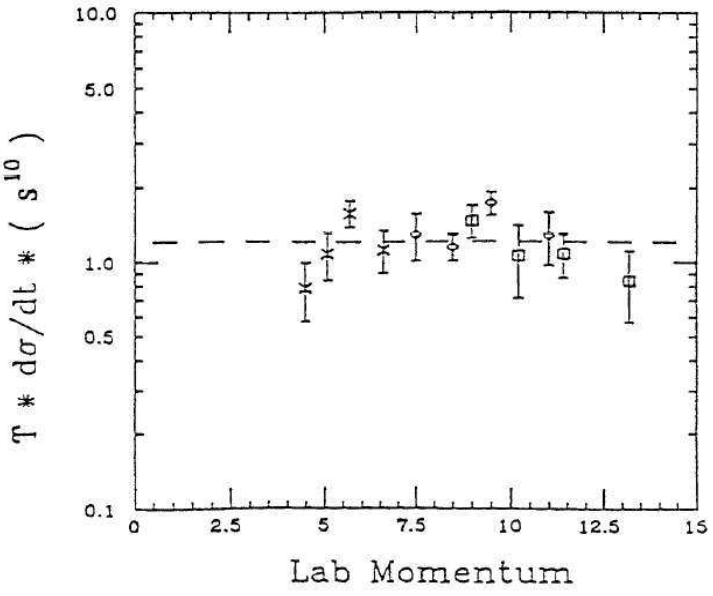

Figure 4.13 The nuclear cross section $T\,d\sigma/dt$ multiplied by an overall power-law factor s^{10}. This plot is taken from Ref. [224] and shows that the oscillations in the nuclear cross section are fairly small.

As mentioned before (see Section 4.1.4), apart from the Ralston-Pire picture on which our results are based, other explanations of the energy dependence of the transparency have been suggested. At the present energies, both the Ralston-Pire approach and the dibaryon resonance model of Brodsky and de Teramond can accomodate the experimental transparencies. At higher energies, however, the predictions of both models are very different. An improved set of data, particularly at higher energies, is essential to distinguish between both models. The 50 GeV proton synchrotron that is under construction at J-PARC [229, 230] opens great opportunities for this research.

Finally, the $\theta_{\mathrm{c.m.}}$ dependence of the nuclear transparency is as yet unexplained. At an incoming momentum of 5.9 GeV/c, the data show a significant dependence on the c.m. scattering angle, while at 7.5 GeV/c the $\theta_{\mathrm{c.m.}}$ dependence flattens out [125, 206]. Most theoretical predictions, including ours, do not heavily depend on $\theta_{\mathrm{c.m.}}$. The $\theta_{\mathrm{c.m.}}$ dependence is similar only to the inverse of the spin correlation, $(A_{NN})^{-1}$, and this possible relation between A_{NN} and nuclear transparency is cer-

tainly worthy of further investigation. In that respect, the possibility of $A(p, 2p)$ transparency measurements at $\theta_{\mathrm{c.m.}} = 15$–$40^\circ$ in the same Q^2 region ($Q^2 = 2$–10 (GeV/c)^2) at the Serpukhov 70 GeV accelerator [231] sounds very promising.

Chapter 5

Second-Order Eikonal Corrections in $A(e, e'p)$ Observables

The previous chapter dealt with the issue of scattering in the GeV energy regime and the accompanying phenomena like CT. In this chapter, we will turn our attention to lower energies and investigate the low-energy accuracy of the eikonal approach. Hereby, our focus is on exclusive electro-induced $A(e, e'p)$ reactions. $A(e, e'p)$ processes provide access to a wide range of nuclear phenomena like short- and long-range correlations, relativistic effects, the transition from hadronic to partonic degrees of freedom, and medium modifications of nucleon properties. Just like $A(p, pN)$ reactions, the interpretation of $A(e, e'p)$ data heavily relies on an accurate description of the effect of the FSI, i.e., the interactions of the ejected proton with the residual nucleus such as rescattering and/or absorption. The eikonal approximation has been widely used to treat these distortions, either in conjunction with optical potentials [56,57,72–75], or with Glauber theory, its multiple-scattering extension [57, 59, 80–86]. The eikonal approach, however, is commonly used in a first-order approximation. The purpose of this chapter is to determine the influence of second-order eikonal corrections on $A(e, e'p)$ observables by using the SOROMEA model that was developed in Section 2.5.

The outline of this chapter is as follows. In Section 5.1, we briefly discuss the various ingredients entering into the calculation of the $A(e, e'p)$ matrix element. The following sections present the results of our $A(e, e'p)$ numerical calculations. In Section 5.2, we look into how the second-order eikonal correction affects an in-

clusive quantity like the nuclear transparency. The induced normal polarization P_n is the subject of investigation in Section 5.3. This observable serves as a rigid test for models dealing with FSI mechanisms, since it is exactly zero in the absence of FSI. The left-right asymmetry A_{LT}, another quantity that reflects the sensitivity to the different ingredients that enter into our model calculations, is studied in Section 5.4. Finally, we end this chapter with a discussion of the effect of the second-order eikonal corrections on $A(e,e'p)$ differential cross sections in Section 5.5.

5.1 The $A(e,e'p)$ Matrix Element

For the description of the $A(e,e'p)$ reaction, we adopt the impulse approximation (IA), where a quasifree single-nucleon knockout reaction mechanism is assumed, and the independent-nucleon picture. Within this approach, the basic quantity to be computed is the transition matrix element [221, 232]

$$\langle J^\mu \rangle = \int d\vec{r}\, \overline{\Psi}^{(-)}_{\vec{k},m_s}(\vec{r})\, \hat{J}^\mu(\vec{r})\, e^{i\vec{q}\cdot\vec{r}}\, \phi_{\alpha_1}(\vec{r})\ . \tag{5.1}$$

Here, ϕ_{α_1} and $\Psi^{(-)}_{\vec{k},m_s}$ are the relativistic bound-state and scattering wave functions, with α_1 the state wherein the struck proton resided and $\vec{k}$ and m_s the momentum and spin of the ejected proton. The relativistic bound-state wave function is obtained in the Hartree approximation to the $\sigma-\omega$ model [38] with the W1 parametrization for the different field strengths [193] and is discussed in more detail in Appendix B. The scattering wave function $\Psi^{(-)}_{\vec{k},m_s}$ appears with incoming boundary conditions and is related by time reversal to the standard scattering wave function $\Psi^{(+)}_{\vec{k},m_s}$ as determined in Sections 2.2 and 2.5. Furthermore, $\hat{J}^\mu$ is the relativistic one-body current operator modeling the coupling between the virtual photon and a nucleon embedded in the medium. Throughout this chapter, we use the Coulomb gauge and the CC2 form of $\hat{J}^\mu$ [233]. For more details on the $A(e,e'p)$ model, we refer to [221].

5.2 Nuclear Transparency

One way to quantify the overall effect of FSI in $A(e,e'p)$ processes is via the nuclear transparency. The measurements [214–216, 218, 222, 223] are commonly performed

under quasielastic conditions. We obtain the theoretical transparencies by adopting similar expressions and cuts as in the experiments. Hence, the nuclear transparency is extracted from the computed $A(e,e'p)$ differential cross sections on the basis of the following ratio [87]

$$T = \frac{\sum_\alpha \int_{\Delta^3 p_m} d\vec{p}_m S^\alpha(\vec{p}_m, E_m, \vec{k})}{c_A \sum_\alpha \int_{\Delta^3 p_m} d\vec{p}_m S^\alpha_{\rm PWIA}(\vec{p}_m, E_m)} \ . \tag{5.2}$$

Here, S^α is the reduced cross section for knockout from the shell α

$$S^\alpha(\vec{p}_m, E_m, \vec{k}) = \frac{\frac{d^5\sigma^\alpha}{d\Omega_p d\epsilon' d\Omega_{\epsilon'}}(e,e'p)}{K\sigma_{ep}} \ , \tag{5.3}$$

where K is a kinematical factor and σ_{ep} is the off-shell electron-proton cross section, which is evaluated with the CC1 prescription of de Forest [233]. $S^\alpha_{\rm PWIA}$ is the reduced cross section within the plane-wave impulse approximation (PWIA) in the nonrelativistic limit. This limit is accomplished by nullifying all sources of FSI mechanisms and neglecting those contributions introduced by the presence of negative-energy components in the relativistic bound-state wave functions [66]. Further, $\sum_\alpha$ extends over all occupied shells α in the target nucleus. The phase-space volume in the missing momentum $\Delta^3 p_m$ is defined by the cut $|p_m| \leq 300$ MeV/c. Finally, the A-dependent factor c_A corrects in a phenomenological way for the effect of short-range mechanisms. It accounts for the fact that short-range correlations move a fraction of the single-particle strength to higher missing energies and momenta and, hence, beyond the ranges covered in $\sum_\alpha \int_{\Delta^3 p_m} d\vec{p}_m$ of Eq. (5.2). We introduce the c_A in the denominator of Eq. (5.2) because the data have undergone a similar rescaling. The adopted values for c_A are 0.9 (^{12}C) and 0.82 (^{56}Fe).

Transparencies have been calculated for the nuclei ^{12}C and ^{56}Fe at planar and constant $(\vec{q},\omega)$ kinematics compatible with the phase space covered in the experiments. For the optical potential, the EDAD1 parametrization of Ref. [46] was used.

In Fig. 5.1 the ROMEA and SOROMEA results are displayed as a function of the four-momentum transfer Q^2 and compared to the data. Not surprisingly, at high Q^2, the ROMEA and SOROMEA predictions practically coincide and the second-order eikonal effects grow with decreasing Q^2. At $Q^2 = 1.7$ (GeV/c)^2, the ROMEA and SOROMEA transparencies agree to 1%; while at $Q^2 = 0.3$ (GeV/c)^2, the difference has risen to 3% for ^{56}Fe and 5% for ^{12}C. The enhancement of the nuclear

transparency due to the second-order eikonal corrections is rather limited, even for values of the four-momentum transfer as low as $Q^2 = 0.2$ (GeV/c)^2. Both the ROMEA and the SOROMEA predictions slightly underestimate the measurements. The second-order corrections move the predictions somewhat closer to the $Q^2 = 0.34$ (GeV/c)^2 data point.

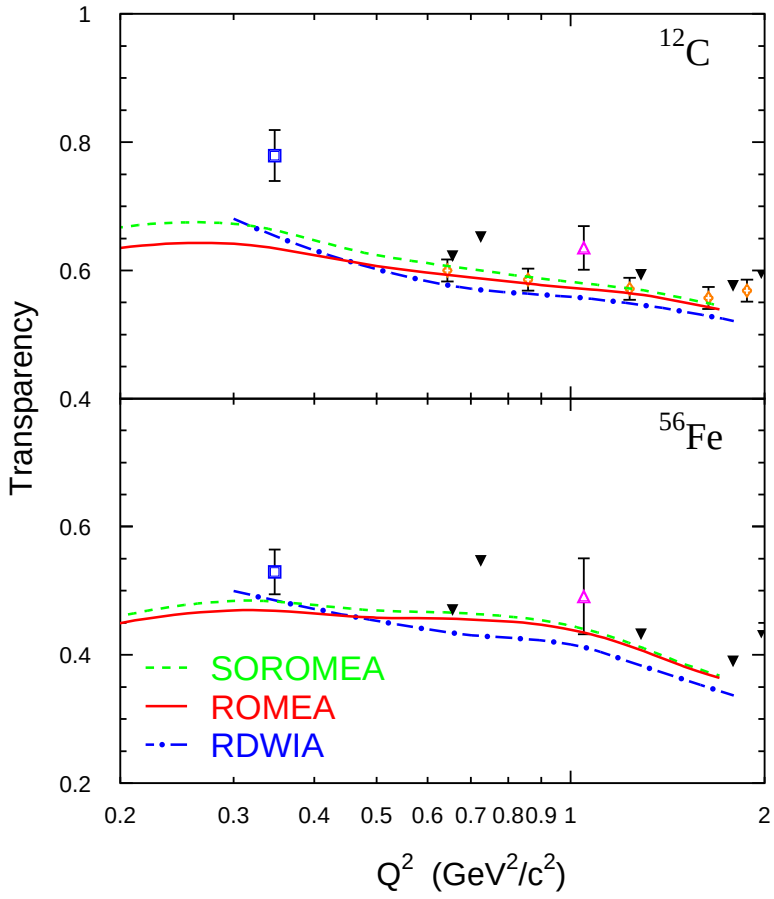

Figure 5.1 Nuclear transparencies versus Q^2 for $A(e, e'p)$ reactions in quasielastic kinematics. The SOROMEA (dashed lines) are compared to the ROMEA (solid lines) results. The RDWIA calculations of Ref. [87] are also shown (dot-dashed curves). The EDAD1 potential [46] has been employed in both the (SO)ROMEA and RDWIA formalisms. Data points are from Refs. [222] (open squares), [214, 215] (open triangles), [216, 218] (solid triangles), and [223] (open diamonds).

Further, Fig. 5.1 also displays the relativistic distorted-wave impulse approximation (RDWIA) results of Ref. [87]. The RDWIA framework was implemented by the Madrid-Sevilla group [234] and is similar to our (SO)ROMEA approach in that both models compute the effect of the FSI with the aid of proton-nucleus optical potentials; but the RDWIA model relies on a partial-wave expansion of the exact scattering wave function. In order to make the comparison with the (SO)ROMEA results as meaningful as possible, all the ingredients in the $A(e,e'p)$ calculations not related to the FSI, such as the bound-state wave functions and the current operator, were kept identical. Moreover, the same EDAD1 parametrization of the optical potential was used. For high Q^2, the RDWIA model predicts a few $\%$ more absorption than (SO)ROMEA, but the Q^2 dependence is quite similar down to $Q^2 \approx 0.7$ (GeV/c)^2. The low Q^2 dependence of the RDWIA transparencies is clearly steeper, even though the second-order corrections slightly improve the similarity in Q^2 dependence between the eikonal and the partial-wave models. The growing discrepancy between RDWIA and (SO)ROMEA with decreasing Q^2 could be due to the fact that the former does not adopt the EMA. On the whole, the SOROMEA transparency results are in slightly better agreement with the data than the RDWIA calculations, which systematically underestimate the data by roughly 5–10%.

In Fig. 5.2 the different model predictions of the attenuation for the individual shells in ^{12}C and ^{56}Fe are compared. These numbers are computed according to the definition of Eq. (5.2) without performing the sum over the states α. The different single-particle shells have very different spatial characteristics. Consequently, by investigating the attenuation for each individual shell in the target nucleus, the radial dependence of the FSI mechanisms can be studied. As expected, the calculations predict stronger attenuation for proton emission from a level with a larger fraction of its density in the nuclear interior. Furthermore, the SOROMEA approach predicts consistently less absorption than ROMEA for all shells. Finally, it should be noted that the discrepancy between RDWIA and (SO)ROMEA at low Q^2 is most evident for the $1s_{1/2}$ orbital. It is this same shell that almost entirely accounts for the strong rise of the ^{12}C RDWIA transparency with decreasing Q^2. For the ^{56}Fe case, the RDWIA and (SO)ROMEA predictions diverge most strongly for the $1p_{1/2}$, $2s_{1/2}$, and $1s_{1/2}$ shells.

To put the second-order eikonal effects into perspective, Fig. 5.3 shows the im-

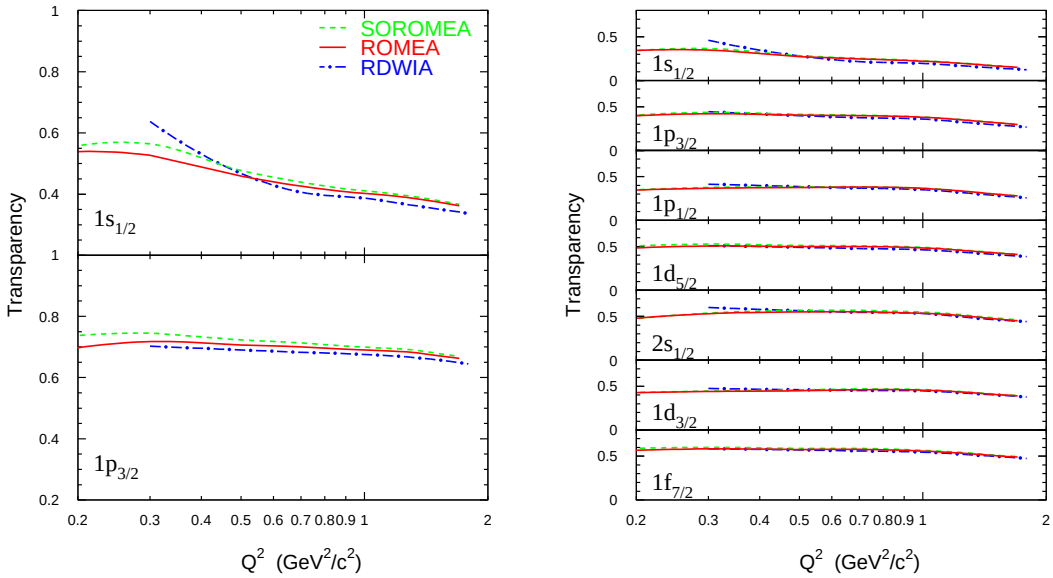

Figure 5.2 The Q^2 dependence of the computed nuclear transparency for the single-particle orbits as obtained in the SOROMEA, ROMEA, and RDWIA approaches with the EDAD1 optical potential of Ref. [46]. The left (right) panel shows the results for ^{12}C (^{56}Fe).

pact of the spin-orbit $V_{so}(\vec{b},z)\,\vec{\sigma}\cdot\vec{b}\times\vec{k}$ and Darwin $V_{so}\,(\vec{b},z)\,(-ikz)$ terms on the nuclear transparency. Especially the Darwin term is important, with its effect being about three times larger than the impact of the second-order eikonal effects. Even though the inclusion of the spin-orbit term partially undoes the reduction of the nuclear transparency due to the Darwin term, the global effect of spin-orbit and Darwin term is still substantial. Further, Fig. 5.3 also displays results for the EDAI parametrization of the optical potential. Clearly, both the predicted Q^2 dependence and the value of the transparency heavily depend on whether an A-dependent (EDAD1) or A-independent (EDAI) fit for the optical potentials is chosen.

Since the nuclear transparency is an integrated quantity, it may hide some of the subtleties present in the treatment of the FSI. Next, we put our second-order eikonal corrections to a more stringent test by focusing on quantities that are probably more sensitive to the details of the calculations.

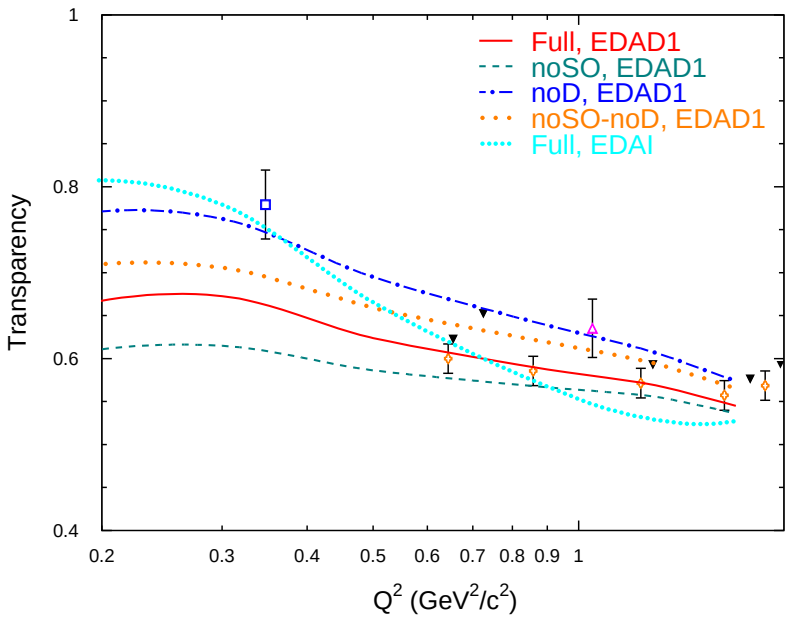

Figure 5.3 The impact of the spin-orbit and Darwin terms on the computed ^{12}C transparency and the sensitivity to the adopted choice for the parametrization of the optical potential. The solid curve is the full SOROMEA calculation with the EDAD1 optical potential. The effect of turning off the spin-orbit and Darwin terms is shown by the dashed and dot-dashed lines, respectively, while the long-dotted curve is obtained by switching off both terms. The short-dotted line displays the full SOROMEA result using the EDAI optical potential. The data are from Refs. [214–216, 218, 222, 223].

5.3 Induced Normal Polarization

An observable that is particularly well suited to study FSI effects is the induced normal polarization

$$P_n = \frac{d^5\sigma\,(\sigma_n =\uparrow) - d^5\sigma\,(\sigma_n =\downarrow)}{d^5\sigma\,(\sigma_n =\uparrow) + d^5\sigma\,(\sigma_n =\downarrow)}\,, \tag{5.4}$$

where σ_n denotes the spin orientation of the ejectile in the direction orthogonal to the reaction plane. Indeed, in the one-photon exchange approximation, P_n vanishes in the absence of FSI.

Fig. 5.4 shows the missing momentum dependence of the induced normal polarization for the kinematics of Ref. [235], corresponding with $Q^2 \approx 0.5$ (GeV/c)^2.

The calculations employed the energy-dependent A-independent EDAI potential of Ref. [46]. The ROMEA results are in line with the RDWIA calculations of the Madrid-Sevilla group [236] and the overall agreement with the data is excellent. The second-order eikonal corrections are most pronounced for the $1s_{1/2}$ level. For missing momenta $p_m > 125$ MeV/c, they reduce the magnitude of the P_n for the $1s_{1/2}$ state by roughly 20%, thereby resulting in a marginally better agreement with the highest p_m data point. For $1p_{3/2}$ knockout, on the other hand, the effect of the second-order eikonal corrections does not exceed the 5% range.

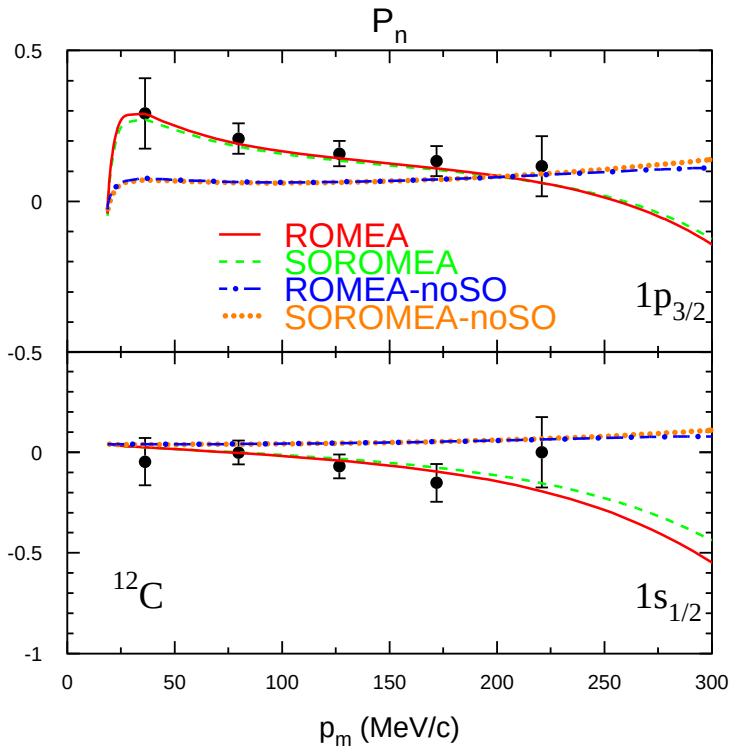

Figure 5.4 Induced normal polarization P_n for proton knockout from the $1p_{3/2}$ (upper panel) and $1s_{1/2}$ (lower panel) shell in the ^{12}C$(e, e'\vec{p})$ reaction. The kinematics is determined by beam energy $\epsilon = 579$ MeV, momentum transfer $q = 760$ MeV/c, energy transfer $\omega = 292$ MeV, and azimuthal angle $\phi = 180°$. The solid (dashed) curves represent ROMEA (SOROMEA) calculations. The dot-dashed (dotted) curves refer to predictions obtained within the ROMEA (SOROMEA) frameworks, with the spin-orbit term $V_{so}(\vec{b}, z)\, \vec{\sigma} \cdot \vec{b} \times \vec{k}$ turned off. The data are from Ref. [235].

The inclusion of the second-order eikonal effects is particularly visible at high missing momentum, a region where other competing mechanisms also become more prominent. The qualitative behavior of the meson-exchange and Δ-isobar currents, for instance, is alike [237]. At low missing momenta $p_m \leq 200$ MeV/c, the induced normal polarization P_n is relatively insensitive to the two-body currents; whereas at higher missing momenta, sizable contributions from the meson-exchange and isobar currents are predicted. The influence of the meson and isobar degrees of freedom is also stronger for knockout from the $1s_{1/2}$ shell than for $1p_{3/2}$ knockout.

In Fig. 5.4 also calculations without the spin-orbit part $V_{so}(\vec{b},z)\,\vec{\sigma}\cdot\vec{b}\times\vec{k}$ are shown. They illustrate that the spin-orbit distortion is the largest source of P_n. Hence, a correct inclusion of this term is essential. Moreover, P_n proves to be rather sensitive to the choice of optical potential [236].

5.4 Left-Right Asymmetry

Another $A(e,e'p)$ observable which has been the subject of many investigations is the left-right asymmetry

$$A_{LT} = \frac{d^5\sigma\,(\phi=0^\circ) - d^5\sigma\,(\phi=180^\circ)}{d^5\sigma\,(\phi=0^\circ) + d^5\sigma\,(\phi=180^\circ)}\,. \tag{5.5}$$

The subscript LT indicates that this quantity is closely related to the longitudinal-transverse response function. The experimental determination of A_{LT} is much less challenging than extracting an absolute cross section or an effective response function. From a theoretical vantage point, this ratio has the advantage of being independent of the spectroscopic factors. Furthermore, it is very well suited to scrutinize different ingredients that enter various model calculations. Indeed, many subtleties that remain concealed in other observables may become prominent in the A_{LT} asymmetry.

Fig. 5.5 presents our A_{LT} predictions for the removal of $1p$-shell protons in ^{16}O as a function of the missing momentum in the kinematics of Refs. [238,239]. The FSI shift the dip in A_{LT} which is located at $p_m \approx 400$ MeV/c in the relativistic PWIA (RPWIA), to lower values of the missing momentum. This shift is essential to describe the data at $p_m \approx 350$ MeV/c. The exact p_m location and height of the ripple,

however, are affected by many ingredients of the calculations, such as the current operator, bound-state wave function, and optical potential [239]. As can be inferred from Fig. 5.5, the second-order eikonal corrections affect the height, but not the p_m position of the ripple. For comparison reasons, we have chosen to only depict the results of our (SO)ROMEA calculations within the so-called noSV approximation. In this approximation, the dynamical enhancement of the lower component of the scattering wave (2.43) due to the $V_s - V_v$ term is omitted. As such, our calculations employ the same set of baseline options as the EMAf-noSV predictions by the Madrid-Sevilla group. The EMAf-noSV approach is an RDWIA calculation which adopts the EMA in combination with the noSV approximation. The second-order effect clearly increases the height of the oscillation in A_{LT} and brings the eikonal calculations in excellent agreement with the corresponding partial-wave prediction EMAf-noSV. Finally, the comparison with the full (SO)ROMEA and RDWIA calculations demonstrates that the inclusion of the dynamical enhancement is also an important aspect in the description of the A_{LT} data.

Next, we discuss some asymmetry results obtained for the ^{12}C nucleus by Dutta *et al.* [218]. Their $^{12}\mathrm{C}(e, e'p)$ experiment in quasiperpendicular kinematics was performed with the aim of extracting nuclear transparencies, thereby measuring reduced cross sections. The corresponding left-right asymmetry for reduced cross sections reads

$$a_{LT} = \frac{S\left(\phi = 0^\circ\right) - S\left(\phi = 180^\circ\right)}{S\left(\phi = 0^\circ\right) + S\left(\phi = 180^\circ\right)} \,, \tag{5.6}$$

with S defined by Eq. (5.3). Fig. 5.6 displays the data of Ref. [218] as well as our RPWIA, ROMEA, and SOROMEA calculations for the reduced asymmetry at three different Q^2 values. In accordance with the A_{LT} predictions, the inclusion of FSI is crucial to reliably reproduce the experimental asymmetry. Indeed, the FSI shift the $p_m \approx 400$ MeV/c dip in the RPWIA a_{LT} to lower missing momenta. As was the case for the ^{16}O asymmetry of Fig. 5.5, the second-order eikonal corrections yield a larger dip in the asymmetry. The net effect of the eikonal corrections, however, diminishes with rising Q^2. The calculations are in line with the RDWIA results of Ref. [240] and describe the $1p_{3/2}$ data reasonably well. For the $1s_{1/2}$ shell, on the other hand, the ROMEA calculations fail to describe the p_m distribution of the reduced asymmetry, in particular at the higher Q^2 values. Moreover, the second-order eikonal corrections seem to move the theoretical curves even further away

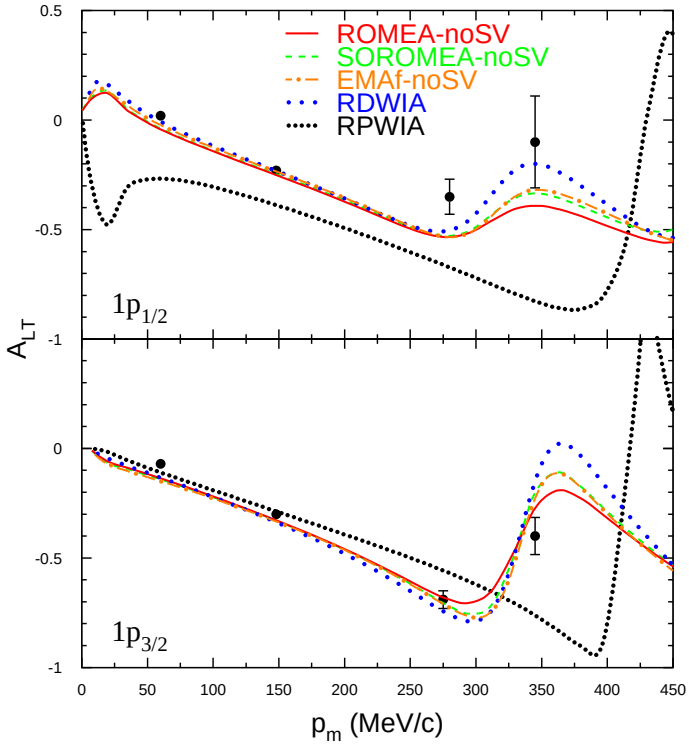

Figure 5.5 The left-right asymmetry A_{LT} for the ^{16}O$(e,e'p)$ experiment of [238]. The kinematics was $\epsilon = 2.442$ GeV, $q = 1$ GeV/c, and $\omega = 445$ MeV (i.e., $Q^2 = 0.8$ (GeV/c)^2). The solid (dashed) lines show the results of the ROMEA-noSV (SOROMEA-noSV) calculations, which differ from the full calculations in that the dynamical enhancement of the lower component of the scattering wave function is neglected. The dot-dashed curves present the results from an RDWIA calculation where the spinor distortions in the scattered wave are neglected, while the long-dotted curves display the full RDWIA predictions. All calculations use the EDAI version for the optical potentials [46]. The short-dotted curves represent the RPWIA results. The data points are from Ref. [238].

from the $1s_{1/2}$ data. The flattening of a_{LT} as Q^2 increases is not yet fully understood, but might indicate greater contamination by the multinucleon continuum.

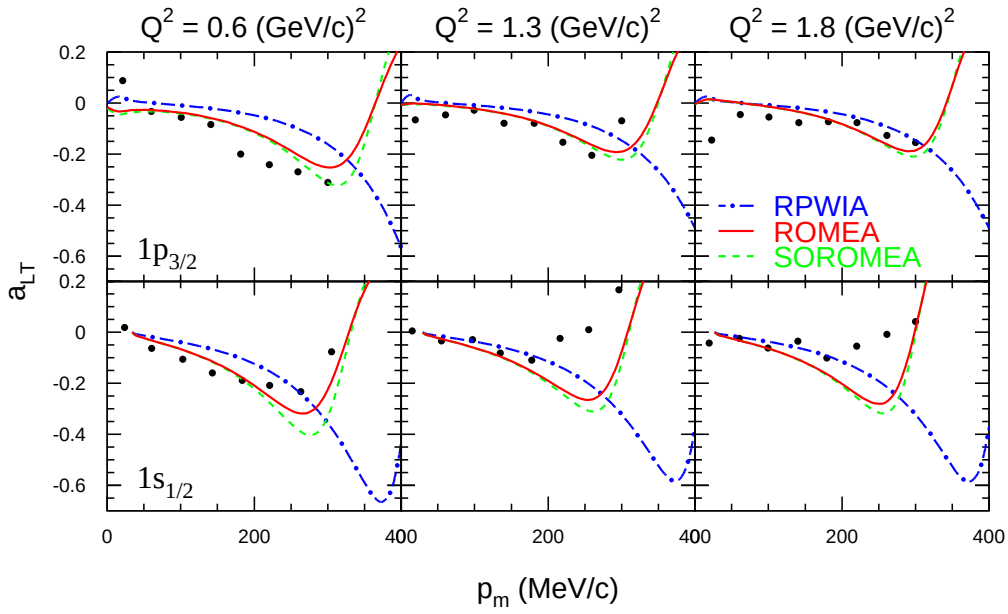

Figure 5.6 The left-right asymmetry for reduced cross sections for the ^{12}C$(e,e'p)$ experiment of [218] at $Q^2 = 0.6$, 1.3, and 1.8 (GeV/c)^2. The solid (dashed) curves refer to ROMEA (SOROMEA) calculations, using the EDAD1 optical potential [46]. The dot-dashed lines show the RPWIA predictions.

5.5 Differential Cross Section

In Fig. 5.7 ^{16}O$(e,e'p)$ cross-section results are displayed for the kinematics of Fig. 5.5. The spectroscopic factors, which normalize the calculations to the data, were determined by performing a χ^2 fit to the data and are summarized in Table 5.1. The RDWIA spectroscopic factors are 5–10% higher than the (SO)ROMEA ones. Both our (SO)ROMEA calculations and the RDWIA predictions of the Madrid-Sevilla group do a very good job of representing the data over the entire p_m range. For missing momenta $|p_m| \leq 250$ MeV/c, the (SO)ROMEA calculations are in excellent agreement with the RDWIA ones. As for the other observables, the impact of the second-order eikonal corrections on the computed differential cross section is no more than a few percent for p_m below the Fermi momentum, but grows to as much as 30% at higher missing momenta. The inclusion of the second-order effects

improves the agreement with the RDWIA calculations at these high missing momenta. Results for the effective response functions R_L, R_T, R_{TL}, and R_{TT} are not shown, but the effect of the second-order eikonal corrections is similar to the effect on the differential cross section.

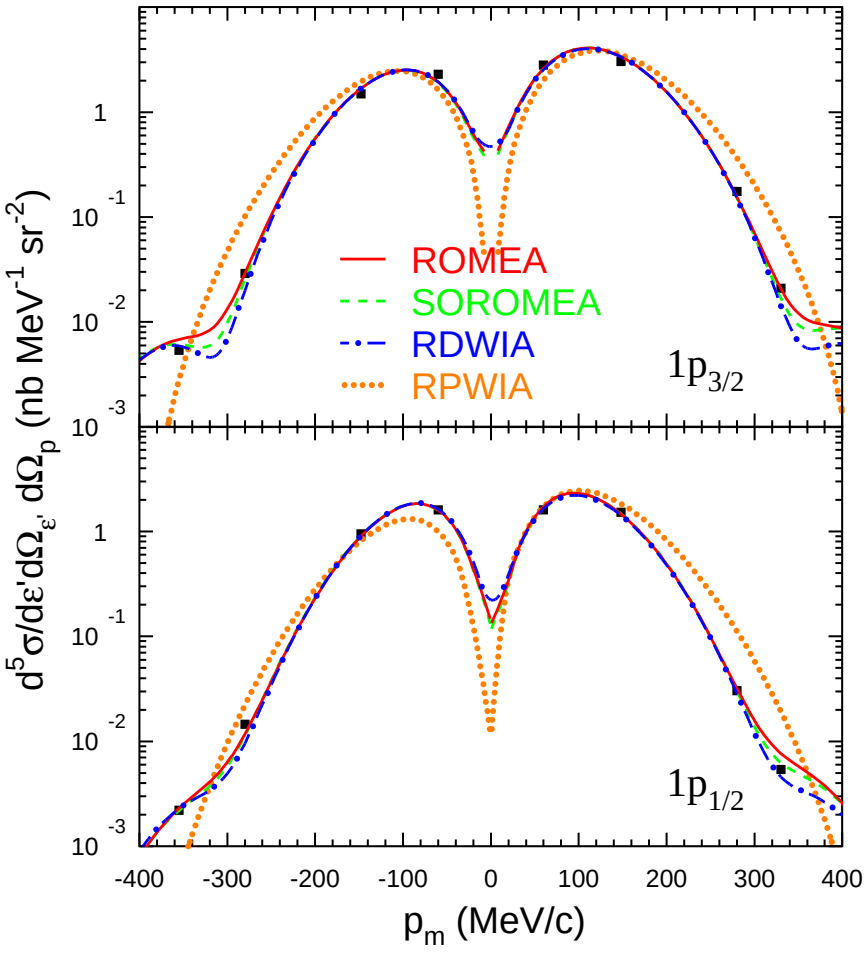

Figure 5.7 ^{16}O$(e,e'p)$ cross sections compared to ROMEA, SOROMEA, RDWIA, RPWIA calculations at the quasiperpendicular kinematics of Fig. 5.5. The calculations use the optical potential EDAI [46]. The data are from Ref. [238]. The following convention is adopted: positive (negative) p_m corresponds to $\phi = 180°$ ($\phi = 0°$).

Fig. 5.8 surveys the Q^2 dependence of the second-order eikonal effect on the

	RPWIA	ROMEA	SOROMEA	RDWIA
$1p_{3/2}$	0.55	0.84	0.83	0.92
$1p_{1/2}$	0.47	0.75	0.74	0.78

Table 5.1 The spectroscopic factors for the $^{16}\mathrm{O}(e,e'p)$ reaction of Ref. [238], as obtained with a χ^2 procedure.

$^{16}\mathrm{O}(e,e'p)$ differential cross section. The ratio of the SOROMEA to the ROMEA calculations is shown as a function of the missing momentum p_m for two Q^2 values. The $Q^2 = 0.8$ (GeV/c)^2 kinematics is as in Figs. 5.5 and 5.7, while the $Q^2 = 0.3$ (GeV/c)^2 kinematics corresponds to the experiment by Chinitz *et al.* [241]. For both Q^2 values, the differences between the SOROMEA and the ROMEA predictions are more prominent at higher missing momenta. On the whole, $Q^2 = 0.3$ (GeV/c)^2 leads to the strongest second-order effects; but even at this low Q^2 value, the effect is at most 15% for p_m below the Fermi momentum.

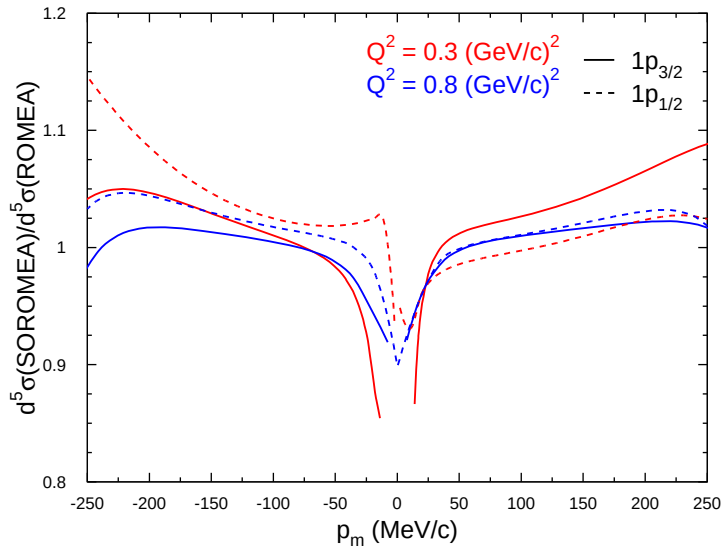

Figure 5.8 The SOROMEA/ROMEA differential cross-section ratio for the $^{16}\mathrm{O}(e,e'p)$ reaction in quasiperpendicular kinematics at two values of Q^2. The red (blue) curves refer to $Q^2 = 0.3$ (0.8) (GeV/c)^2.

Chapter 6

Conclusions and Outlook

In this work, we have outlined a relativistic and cross-section factorized framework to describe quasielastic $A(p,pN)$ reactions. The model relies on the impulse approximation and the bound-state wave functions are obtained from a mean-field approximation to the $\sigma-\omega$ model [38]. Relativity is accomodated in both the dynamics and the kinematics. To model the propagation of the nucleons through the nuclear medium, a relativistic framework based on the eikonal approximation [54, 55] has been developed. The eikonal approximation is a semiclassical method, which finds its origins in optics, and its applicability is restricted to small-angle scattering. This eikonal model provides a common framework to describe a variety of nuclear reactions and has been applied by our research group to $A(e,e'p)$ [56, 57, 59, 87, 88], $A(\nu,\nu'N)$, $A(\overline{\nu},\overline{\nu}'N)$, $A(\nu_l,l^-N)$, $A(\overline{\nu}_l,l^+N)$ [242, 243], and $A(\gamma,\pi N)$ [244] reactions. Here, however, the main focus is on $A(p,pN)$ reactions. With three nucleons subject to attenuation effects, this reaction provides an excellent testing ground for the relativistic eikonal approximation.

Our theoretical eikonal framework is very flexible as it can be used either in conjunction with relativistic optical potentials (ROMEA) or within a Glauber multiple-scattering approach (RMSGA), which are two substantially different techniques to deal with the IFSI. Thanks to the freedom of choice between these two techniques, our model is expected to be applicable at both intermediate and high incident energies.

The ROMEA framework is similar to the DWIA approach, in which most theoretical work on $A(p,pN)$ reactions was performed over the last number of decades,

in the sense that both of them incorporate IFSI in terms of optical potentials. These optical potentials are usually constructed by global fits to nucleon-nucleus elastic scattering data. However, whereas the DWIA typically adopts a partial-wave expansion of the exact solution to the scattering problem, the ROMEA framework relies on the eikonal approximation to calculate the scattering wave function. The eikonal approach is particularly convenient at higher energies, where approaches relying on partial-wave expansions become increasingly impractical.

For kinetic energies exceeding 1 GeV, the elementary nucleon-nucleon scattering cross sections become increasingly inelastic and diffractive, and a treatment of the IFSI that relies on an optical-potential approach can no longer be justified. In this high-energy region, the RMSGA framework, which is a multiple-scattering extension of the eikonal approximation, offers a valid and economical alternative. In such a Glauber approach, the effects of IFSI are calculated directly from the nucleon-nucleon scattering data through the introduction of a profile function. Thus, the major difference between both approaches is that the ROMEA framework describes the IFSI in terms of a nucleon-nucleus picture, whereas the RMSGA framework is essentially a nucleon-nucleon model. For kinetic energies above 1 GeV, the latter method is recommended; while the former is more suitable at lower energies.

In the calculations, the entire effect of the IFSI is accounted for by the IFSI factor. The properties of this function have been investigated for quasielastic proton scattering from ^{12}C, ^{16}O, and ^{40}Ca at an incident proton energy of 1 GeV, corresponding with the kinematics of the PNPI experiment of Ref. [114]. Not surprisingly, the strongest attenuation occurs in the nuclear interior, and heavier target nuclei are found to induce larger IFSI effects. Also, the surface-peaked character of the $A(p,pN)$ reaction was clearly established to be a consequence of the IFSI. In this experiment, as in many other $A(p,pN)$ reactions, one faces the situation in which one of the ejectiles is relatively slow. Consequently, the Glauber multiple-scattering approach is not applicable, even though the energies of the impinging proton and the other ejectile are sufficiently large. The ROMEA calculations, on the other hand, give rise to realistic IFSI factors, with the different types of optical-potential sets contained in Ref. [46] yielding comparable results.

Next, the cross-section calculations for the PNPI experiment have been com-

pared to the data. The RMSGA approach fails to give an adequate description of the data because of the low kinetic energy of the ejected nucleon, but the ROMEA calculations reproduce the shapes of the measured differential cross sections reasonably well. Moreover, comparison with the RPWIA predictions illustrates the twofold effect of the IFSI. Besides the attenuation of the RPWIA cross section, the IFSI also lead to a shift in the momentum distribution. The ROMEA model has also been used to calculate cross sections for the kinematics of other experiments: ^{40}Ca$(p, 2p)$ scattering at 460 MeV [115], ^{16}O$(p, 2p)$ and (p, pn) scattering at 505 and 200 MeV [8, 116], and ^{4}He$(p, 2p)$ scattering at 250 MeV [9]. A fair description of the data is obtained for the different kinematics, thereby providing support for the wide applicability range of our model.

The RMSGA approach, which was deemed unsuitable for the experiments discussed before, has been used to account for the IFSI in the study of $A(p, 2p)$ nuclear transparencies at high energies. To explain the oscillatory energy dependence of the nuclear transparency data [124–126], the Ralston-Pire model for the pp scattering amplitude [144] was implemented in our formalism. In their model, the free pp scattering amplitude consists of a small-sized quark-counting and a normal-sized Landshoff contribution. The interference between these two components results in oscillations in the free pp cross section. Inside the nuclear medium, the Landshoff component is absorbed via the regular Glauber mechanism, while the quark-counting component escapes with relatively small attenuation due to color transparency. Our $A(p, 2p)$ framework was adjusted to incorporate this so-called "nuclear filtering" phenomenon. To describe the phenomenon of CT in our model, we considered two different models: the quantum diffusion model of Farrar *et al.* [148] and the hadronic expansion model of Jennings and Miller [149].

To our knowledge, the detailed RMSGA calculations of the $A(p, 2p)$ nuclear transparency are the first of their kind. Unfortunately, the RMSGA procedure entails the numerical calculation of an involving multi-dimensional integral which tracks the effect of all collisions of the incoming and outgoing protons with the remaining nucleons in the target nucleus. Thereby, each of the target nucleons acts as a scattering center and is represented by its own relativistic wave function. To reduce the computational cost of the RMSGA calculations, some additional approximations were made, including replacing the individual wave functions of the spec-

tator nucleons by the average proton or neutron density of the residual nucleus. The nuclear transparency predictions with the full and the approximated RMSGA approach agree at the few percent level. Thus, to determine integrated quantities such as the nuclear transparency, a valid alternative for the computationally intensive RMSGA framework is available.

Our calculations were brought in qualitative agreement with the $A(p,2p)$ transparency data through the introduction of the nuclear filtering concept. The major conclusion of our study of the $A(p,2p)$ nuclear transparency is that CT is indispensable to elevate the predicted transparencies to the level observed by the experiments. The quantitative agreement with the data, however, can be much improved and several uncertainties still surround the research into $A(p,2p)$ nuclear transparencies.

Finally, we have studied the validity of the eikonal approximation for the description of the $A(e,e'p)$ reaction at lower energies. To this end, we have developed an extension of the ROMEA model which accounts for second-order eikonal corrections, dubbed SOROMEA. The $A(e,e'p)$ nuclear transparency calculations confirm the expected energy dependence of the second-order eikonal corrections: the effect increases with decreasing Q^2. However, even at $Q^2 \approx 0.2$ (GeV/c)^2, the effect of the second-order eikonal corrections on the $A(e,e'p)$ nuclear transparency is rather modest. Further, we have paid attention to the missing momentum dependence of several $A(e,e'p)$ observables like the induced normal polarization P_n, the left-right asymmetry A_{LT}, and the differential cross section. At low missing momenta, the difference between the ROMEA and SOROMEA predictions is observed to be negligible. In the high-p_m region, however, the second-order eikonal corrections are significant with effects up to the 30% level. Thereby, the calculations are brought in closer agreement with the data and/or the RDWIA calculations.

Overall, our numerical calculations show that the effect of the second-order eikonal corrections on $A(e,e'p)$ observables is rather limited for $Q^2 \geq 0.2$ (GeV/c)^2. Varying the adopted choice of optical potential, current operator, bound-state wave functions, ... leads to comparable effects.

To conclude, we would like to propose some possibilities for future work. To allow for the inclusion of spin dependence in the description of the IFSI, the existing $A(p,pN)$ model should be transformed into an amplitude factorized formalism.

Such a framework could then be used to calculate $A(p, pN)$ spin observables. The second-order extension of the eikonal framework might also prove useful in this context.

The study of the $A(p, 2p)$ nuclear transparency is another research area that is obviously still open for improvement. Here, a hybrid model that combines a partonic and a hadronic point of view might result in a better description of the data.

Appendix A

Notations and Conventions

A.1 Abbreviations

BNL	Brookhaven National Laboratory
c.m.	center of mass
CT	color transparency
EA	eikonal approximation
EFI	Enrico Fermi Institute
EMA	effective momentum approximation
FLFS	Farrar, Liu, Frankfurt, and Strikman model
FSI	final-state interactions
HHC	hadron helicity conservation
IA	impulse approximation
IFSI	initial- and final-state interactions
IPM	independent-particle model
ISI	initial-state interactions
JM	Jennings and Miller model
L	Landshoff
NCSE	nuclear color screening effect
NF	nuclear filtering
PLC	point-like configuration
PNPI	Petersburg Nuclear Physics Institute
pQCD	perturbative quantum chromodynamics
QC	quark-counting
QCD	quantum chromodynamics
QED	quantum electrodynamics
QHD	quantum hadrodynamics

(R)DWIA	(relativistic) distorted-wave impulse approximation
RMSGA	relativistic multiple-scattering Glauber approximation
RMSGA′	approximated RMSGA
ROMEA	relativistic optical model eikonal approximation
(R)PWIA	(relativistic) plane-wave impulse approximation
SOROMEA	second-order relativistic optical model eikonal approximation
SPVAT	scalar, pseudoscalar, vector, axial vector, tensor
SRC	short-range correlations
TRIUMF	TRI-University Meson Facility

A.2 Pauli Matrices

The spin operator is defined as

$$\vec{\sigma} = (\sigma_x, \sigma_y, \sigma_z) = \sigma^i \, \vec{e}_i \ , \tag{A.1}$$

where the Pauli matrices are given by

$$\sigma_x = \begin{pmatrix} 0 & 1 \\ 1 & 0 \end{pmatrix} \ , \qquad \sigma_y = \begin{pmatrix} 0 & -i \\ i & 0 \end{pmatrix} \ , \qquad \sigma_z = \begin{pmatrix} 1 & 0 \\ 0 & -1 \end{pmatrix} \ . \tag{A.2}$$

The isospin operator $\vec{\tau} = (\tau_1, \tau_2, \tau_3)$ has the same matrix representation.

A.3 Dirac Matrices

The Dirac or γ matrices are defined by the anticommutation relations

$$\{\gamma^\mu, \gamma^\nu\} = 2\, g^{\mu\nu} \ , \tag{A.3}$$

and, in the Dirac-Pauli representation, are given by

$$\gamma^0 = \begin{pmatrix} 1 & 0 \\ 0 & -1 \end{pmatrix} \ , \qquad \gamma^i = \begin{pmatrix} 0 & \sigma_i \\ -\sigma_i & 0 \end{pmatrix} \ . \tag{A.4}$$

Other commonly used matrices are β and $\vec{\alpha}$, defined as

$$\beta = \gamma^0 \ , \qquad \vec{\alpha} = \gamma^0 \, \vec{\gamma} \ . \tag{A.5}$$

Appendix B

Relativistic Bound-State Wave Functions

Traditionally, nuclear physics calculations relied on the nonrelativistic Schrödinger equation. In nonrelativistic many-body theory, nuclei are described as bound states of nucleons interacting via two- and three-body potentials. Although this approach has enjoyed many successes in describing the properties of nuclear matter, a relativistic treatment is preferable for several reasons. First, the mesonic degrees of freedom can be introduced at the start of the development of the model. Second, the principles of causality, retardation, and relativistic kinematics can be easily incorporated in a relativistic framework. Furthermore, the spin-orbit interaction needs to be inserted by hand in nonrelativistic theories, but emerges automatically in relativistic models.

Relativistic quantum field theories based on hadrons, known as quantum hadrodynamics (QHD), have been found to be very successful in describing the bulk and single-particle properties of nuclear matter and finite nuclei [38, 245–248]. The approach was originally introduced by Walecka roughly 30 years ago [36] and uses the nucleon (as a Dirac particle), the isoscalar-scalar σ, and the isoscalar-vector ω mesons as the relevant degrees of freedom. In this so-called $\sigma - \omega$ model, the Lagrangian density reads [37, 38]

$$\begin{aligned} \mathcal{L}_0 &= \bar{\psi}\,(i\not{\partial} - M_N)\,\psi + \frac{1}{2}\,(\partial_\mu\phi\,\partial^\mu\phi - m_s^2\,\phi^2) - \frac{1}{4}\,G_{\mu\nu}\,G^{\mu\nu} \\ &\quad + \frac{1}{2}\,m_v^2\,V_\mu V^\mu - g_v\,\bar{\psi}\gamma_\mu\psi V^\mu + g_s\,\bar{\psi}\psi\phi\,. \end{aligned} \tag{B.1}$$

The nucleons (ψ) interact with scalar fields (ϕ) through a Yukawa coupling $\overline{\psi}\psi\phi$ and with neutral vector fields (V_μ) that couple to the conserved baryon current $\overline{\psi}\gamma_\mu\psi$. Here, M_N, m_s, and m_v are the nucleon, scalar meson, and vector meson masses, respectively, g_s and g_v are the scalar and vector couplings to the nucleon, and $G^{\mu\nu} \equiv \partial^\mu V^\nu - \partial^\nu V^\mu$ is the vector meson field strength. The scalar (ϕ) and vector (V_μ) fields are associated with the σ and ω mesons. Solving the complete quantum field theory is far from trivial and to tackle the problem, the meson field operators are usually replaced by their classical expectation values or "mean fields". This constitutes the so-called Hartree approximation [36]. In infinite matter, this amounts to $\langle\phi\rangle \equiv \phi_0$ and $\langle V^\mu\rangle \equiv \delta^{\mu 0}\, V_0$. In a Hartree-Fock approach, the resulting mean-field problem can then be solved iteratively. The model can be extended to also include the isovector-vector ρ and the pseudo-scalar π mesons, as well as the coupling to the photon field [249].

In an attempt to include the principles of quantum chromodynamics (QCD), various QHD models have been developed. In particular, the constriant of chiral symmetry plays an important role in hadronic physics at low energies and, consequently, there is a long history of attempts to unite relativistic mean-field phenomenology based on hadrons with manifest chiral symmetry. An overview of the successes and failures of the different models is given in Refs. [247, 248]. Whereas in the original Walecka model (B.1) no attempt was made to reconcile the model with the spontaneously broken, approximate $SU(2)_L \times SU(2)_R$ chiral symmetry of hadronic interactions; in the model developed by Furnstahl *et al.* [193, 250, 251], a nonlinear realization of chiral symmetry is adopted. This chiral effective field theory includes all the underlying symmetries of QCD, such as Lorentz covariance, parity conservation, time-reversal and charge-conjugation invariance, isospin symmetry, unitarity, and gauge invariance. Moreover, it is based on a density-functional approach in which higher-order many-body corrections are treated approximately, which is equivalent to a Hartree calculation [251]. The results are calculated at one-baryon-loop order, which is corresponds with the Dirac-Hartree approximation [37].

The Furnstahl model leads to a static Dirac equation [38]

$$\hat{\mathcal{H}}\,\phi_\alpha\left(\vec{r},\vec{\sigma}\right) = E_\alpha\,\phi_\alpha\left(\vec{r},\vec{\sigma}\right)\ , \tag{B.2}$$

with eigenvalues E_α and eigenfunctions $\phi_\alpha\left(\vec{r},\vec{\sigma}\right)$, and where the single-particle

Dirac Hamiltonian is given by [193]

$$\begin{aligned}\hat{\mathcal{H}} &= -i\,\vec{\alpha}\cdot\vec{\nabla} + g_v\,V_0\,(\vec{r}) + \frac{1}{2}\,\tau_3\,g_\rho\,b_0\,(\vec{r}) + \beta\,(M_N - g_s\,\Phi_0\,(\vec{r})) \\ &\quad + \frac{1}{2}\,(1+\tau_3)\;e\,A_0\,(\vec{r}) - \frac{i}{2M_N}\,\beta\,\vec{\alpha}\cdot\left(f_\rho\,\frac{1}{2}\,\tau_3\,g_\rho\,\vec{\nabla}b_0\,(\vec{r}) + f_v\,g_v\,\vec{\nabla}V_0\,(\vec{r})\right) \\ &\quad + \frac{1}{2M_N^2}\,(\beta_s + \beta_v\,\tau_3)\;e\,\nabla^2 A_0\,(\vec{r}) - \frac{i}{2M_N}\,\lambda\,\beta\,e\,\vec{\alpha}\cdot\vec{\nabla}A_0\,(\vec{r})\;. \end{aligned} \tag{B.3}$$

Here, Φ_0, V_0, b_0, and A_0 refer to the σ, ω, ρ, and electromagnetic mean fields, respectively; and g_s, g_v, g_ρ, and e are the corresponding scalar, vector, rho, and electromagnetic couplings. The coupling between the ρ (ω) meson and the nucleon is denoted by f_ρ (f_v), while β_s (β_v) is the coupling for higher-order σN and $\sigma\sigma$ (ωN and $\omega\omega$) interactions. Furthermore, τ_3 is the third component of the isospin operator and $\lambda \equiv \frac{1}{2}\lambda_p\,(1+\tau_3) + \frac{1}{2}\lambda_n\,(1-\tau_3)$ is the anomalous magnetic moment, with $\lambda_p = 1.793$ and $\lambda_n = -1.913$. The pion field does not enter in the Hartree approximation, if one assumes that the nuclear ground state is spherically symmetric and a parity eigenstate [252].

For spherically symmetric potentials, the solutions $\phi_\alpha\,(\vec{r},\vec{\sigma})$ to a single-particle Dirac equation have the form [253]

$$\phi_\alpha\,(\vec{r},\vec{\sigma}) \equiv \phi_{n\kappa m}\,(\vec{r},\vec{\sigma}) = \left[\begin{array}{c} i\,\frac{G_{n\kappa}(r)}{r}\;\mathcal{Y}_{\kappa m}(\Omega,\vec{\sigma}) \\ -\frac{F_{n\kappa}(r)}{r}\;\mathcal{Y}_{-\kappa m}(\Omega,\vec{\sigma}) \end{array}\right]\,, \tag{B.4}$$

where n denotes the principal and κ and m the generalized angular momentum quantum numbers. The $\mathcal{Y}_{\pm\kappa m}$ are the spin spherical harmonics and determine the angular and spin parts of the wave function,

$$\begin{aligned}\mathcal{Y}_{\kappa m}(\Omega,\vec{\sigma}) &= \sum_{m_l m_s}\left\langle l m_l \frac{1}{2} m_s \mid jm\right\rangle Y_{lm_l}(\Omega)\,\chi_{\frac{1}{2}m_s}(\vec{\sigma})\,, \\ \mathcal{Y}_{-\kappa m}(\Omega,\vec{\sigma}) &= \sum_{m_l m_s}\left\langle \bar{l} m_l \frac{1}{2} m_s \mid jm\right\rangle Y_{\bar{l}m_l}(\Omega)\,\chi_{\frac{1}{2}m_s}(\vec{\sigma})\,, \end{aligned} \tag{B.5}$$

with

$$j = |\kappa| - \frac{1}{2}\;,\; l = \left\{\begin{array}{ll} \kappa, & \kappa > 0 \\ -(\kappa+1), & \kappa < 0 \end{array}\right.\;,\; \bar{l} = 2j - l = \left\{\begin{array}{ll} \kappa - 1, & \kappa > 0 \\ -\kappa, & \kappa < 0 \end{array}\right.\;. \tag{B.6}$$

The Dirac equation (B.2) (or the Lagrangian of Eq. (B.1) solved in the relativistic Hartree approximation) leads to a set of coupled equations for the different fields

Φ_0, V_0, b_0, A_0, $G_{n\kappa}$, and $F_{n\kappa}$. This set of equations is solved iteratively, starting from an educated guess of the meson potentials. The solutions depend on the nucleon and meson masses and coupling constants. In this work, all bound-state wave functions are computed using the W1 parametrization set of Furnstahl *et al.* [193].

In Fig. B.1, the charge density and form factor of ^{40}Ca are shown. The results obtained with the W1 parametrization of Ref. [193] are compared with the predictions of Ref. [37]. The theoretical results agree reasonably well with the data of Ref. [254], and the correspondence between the theoretical and experimental average binding energy per nucleon is also quite good. Even though an IPM description of the four-nucleon system appears rather questionable, the bound-state wave functions of the ^{4}He nucleus are also calculated in the Furnstahl model [193]. After all, at present, realistic relativistic ^{4}He wave functions are not available, and a mean-field approach is the only viable option. The W1 parametrization reproduces the low-momentum-transfer part of the ^{4}He charge form factor fairly well [221]. The discrepancy between the calculation and the data at high momentum transfer is caused by the two-body charge operator contributions [255].

The Fourier transform of the relativistic bound-nucleon wave function (B.4) is given by

$$\phi_\alpha\left(\vec{p}\right) = \int d\vec{r}\, e^{-i\vec{p}\cdot\vec{r}}\, \phi_\alpha\left(\vec{r}\right) = (-i)^l\,(2\pi)^{3/2} \begin{bmatrix} g_{n\kappa}(p)\, \mathcal{Y}_{\kappa m}(\Omega_p) \\ -S_\kappa\, f_{n\kappa}(p)\, \mathcal{Y}_{-\kappa m}(\Omega_p) \end{bmatrix} , \tag{B.7}$$

with $S_\kappa = \kappa/\left|\kappa\right|$. The radial functions $g_{n\kappa}$ and $f_{n\kappa}$ in momentum space are obtained from their counterparts in coordinate space:

$$g_{n\kappa}(p) = i\,\sqrt{\frac{2}{\pi}} \int_0^\infty r^2 dr\, \frac{G_{n\kappa}(r)}{r}\, j_l(pr)\ , \tag{B.8a}$$

$$f_{n\kappa}(p) = i\,\sqrt{\frac{2}{\pi}} \int_0^\infty r^2 dr\, \frac{F_{n\kappa}(r)}{r}\, j_{\bar{l}}(pr)\ , \tag{B.8b}$$

with $j_l(pr)$ the spherical Bessel function of the first kind.

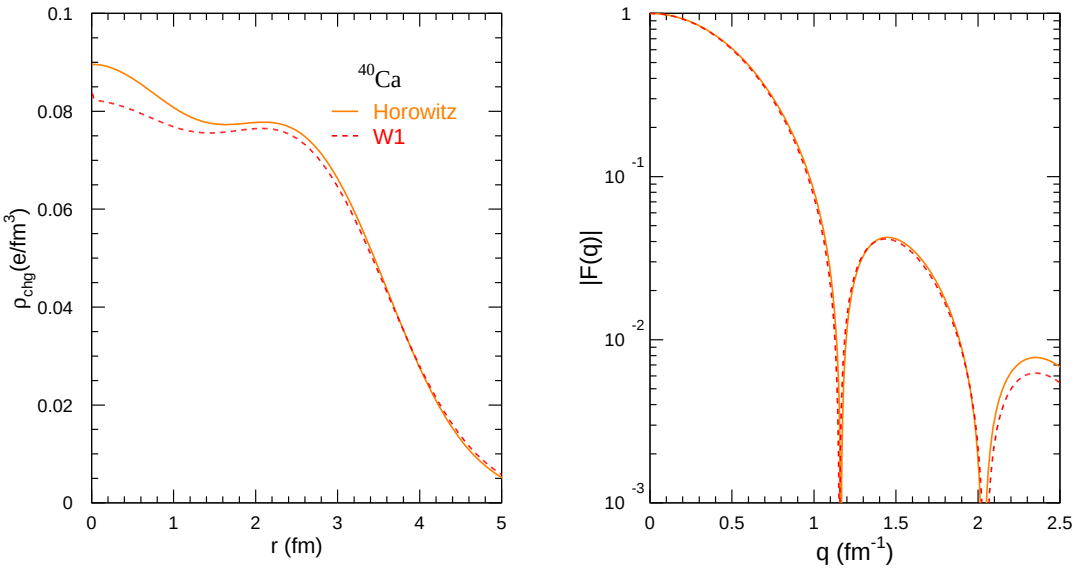

Figure B.1 The left (right) panel shows the charge density (form factor) of ^{40}Ca. The solid curve displays the prediction of Ref. [37]. The dashed curve is obtained with the W1 parametrization of Ref. [193].

Appendix C

Radial and Polar-Angle Contribution to the $A(p, pN)$ Cross Section

The differential $A(p, pN)$ cross section (2.40) is proportional to the distorted momentum distribution ρ^D of Eq. (2.38). When approximating the completeness relation (2.17) as

$$\sum_s u(\vec{p}_m, m_s)\, \bar{u}(\vec{p}_m, m_s) \approx 1 \ , \tag{C.1}$$

i.e., neglecting the negative-energy term as in Section 2.1.2, this amounts to

$$\left(\frac{d^5\sigma}{dE_{k1} d\Omega_1 d\Omega_2}\right)^D \propto \sum_m \overline{\phi^D_{\alpha_1}}\, \phi^D_{\alpha_1} \ . \tag{C.2}$$

Thus, with $D_r\,(r)$ defined as

$$D_r\,(r) \equiv \int d\Omega\, r^2\, e^{-i\vec{p}_m\cdot\vec{r}}\, \phi_{\alpha_1}\,(\vec{r})\ \widehat{\mathcal{S}}_{\rm IFSI}\,(\vec{r}) \ , \tag{C.3}$$

the function

$$\begin{aligned}
\delta_r\,(r_1) \ &\equiv \ \sum_m \frac{1}{\Delta R}\Bigg[\int_0^\infty dr\, \overline{D}_r\,(r) \int_0^\infty dr\, D_r\,(r) - \\
&\quad \Big(\int_0^{r_1} dr\, \overline{D}_r\,(r) + \int_{r_1+\Delta R}^\infty dr\, \overline{D}_r\,(r)\Big)\Big(\int_0^{r_1} dr\, D_r\,(r) + \int_{r_1+\Delta R}^\infty dr\, D_r\,(r)\Big)\Bigg] \\
&= \ \sum_m \big(\overline{D}_r\,(r_1)\ \phi^D_{\alpha_1} + \overline{\phi^D_{\alpha_1}}\, D_r\,(r_1)\big)
\end{aligned} \tag{C.4}$$

represents the contribution of an infinitesimal interval in r around r_1 (integrated over the entire (θ, ϕ) range) to the $A(p, pN)$ cross section. This procedure also enables us to estimate the average density seen through this reaction as

$$\langle \rho \rangle \equiv \frac{\int_0^\infty \rho\,(r)\ \delta_r\,(r)\ dr}{\int_0^\infty \delta_r\,(r)\ dr}\ . \tag{C.5}$$

In a similar fashion, the function

$$\delta_{r,\theta}\,(r_1, \theta_1) \equiv \sum_m \left(\overline{D}_{r,\theta}\,(r_1, \theta_1)\ \phi^D_{\alpha_1} + \overline{\phi^D_{\alpha_1}}\ D_{r,\theta}\,(r_1, \theta_1)\right)\ , \tag{C.6}$$

with

$$D_{r,\theta}\,(r, \theta) \equiv \int d\phi\ \sin\theta\, r^2\, e^{-i\vec{p}_m \cdot \vec{r}}\, \phi_{\alpha_1}\,(\vec{r})\ \widehat{\mathcal{S}}_{\mathrm{IFSI}}\,(\vec{r})\ , \tag{C.7}$$

is the cross-section contribution of an infinitesimal interval in r and θ around r_1 and θ_1.

Bibliography

[1] G. Jacob and T. A. J. Maris, "Quasi-Free Scattering and Nuclear Structure," Rev. Mod. Phys. **38,** 121 (1966).

[2] G. Jacob and T. A. J. Maris, "Quasi-Free Scattering and Nuclear Structure. II," Rev. Mod. Phys. **45,** 6 (1973).

[3] P. Kitching, W. J. McDonald, T. A. J. Maris, and C. A. Z. Vasconcellos, "Recent Developments in Quasi-Free Nucleon-Nucleon Scattering," Adv. Nucl. Phys. **15,** 43 (1985).

[4] N. S. Chant and P. G. Roos, "Distorted-wave impulse-approximation calculations for quasifree cluster knockout reactions," Phys. Rev. C **15,** 57 (1977).

[5] S. Kullander, F. Lemeilleur, P. U. Renberg, G. Landaud, J. Yonnet, B. Fagerström, A. Johansson, and G. Tibell, "$(p, 2p)$ reactions at 600 MeV and the distorted-wave impulse approximation," Nucl. Phys. A **173,** 357 (1971).

[6] R. K. Bhowmik, C. C. Chang, P. G. Roos, and H. D. Holmgren, "The ^{7}Li$(p, 2p)^5$He reaction at 100 MeV," Nucl. Phys. A **226,** 365 (1974).

[7] R. Bengtsson, T. Berggren, and C. Gustafsson, "DWIA analysis of quasifree proton-proton scattering in nuclei at intermediate energies," Phys. Rep. **41,** 191 (1978).

[8] P. Kitching, C. A. Miller, W. C. Olsen, D. A. Hutcheon, W. J. McDonald, and A. W. Stetz, "Quasi-free scattering of polarized protons," Nucl. Phys. A **340,** 423 (1980).

[9] W. T. H. van Oers *et al.*, "^{4}He$(p, 2p)^3$H reaction at intermediate energies," Phys. Rev. C **25,** 390 (1982).

[10] D. S. Carman *et al.*, "Quasifree inclusive and exclusive cross sections at 200 MeV," Phys. Lett. B **452,** 8 (1999).

[11] N. S. Chant and P. G. Roos, "Spin orbit effects in quasifree knockout reactions," Phys. Rev. C **27,** 1060 (1983).

[12] R. A. Arndt, I. I. Strakovsky, and R. L. Workman, "Nucleon-nucleon elastic scattering to 3 GeV," Phys. Rev. C **62,** 034005 (2000).

[13] Scattering Analysis Interactive Dial-in Program (SAID), http://gwdac.phys.gwu.edu/ .

[14] J. A. McNeil, L. Ray, and S. J. Wallace, "Impulse approximation NN amplitudes for proton-nucleus interactions," Phys. Rev. C **27,** 2123 (1983).

[15] J. A. McNeil, J. R. Shepard, and S. J. Wallace, "Impulse-Approximation Dirac Optical Potential," Phys. Rev. Lett. **50,** 1439 (1983).

[16] J. R. Shepard, J. A. McNeil, and S. J. Wallace, "Relativistic Impulse Approximation for p-Nucleus Elastic Scattering," Phys. Rev. Lett. **50,** 1443 (1983).

[17] C. J. Horowitz, "Relativistic Love-Franey model: Covariant representation of the NN interaction for N-nucleus scattering," Phys. Rev. C **31,** 1340 (1985).

[18] C. J. Horowitz and M. J. Iqbal, "Relativistic effects on spin observables in quasielastic proton scattering," Phys. Rev. C **33,** 2059 (1986).

[19] D. P. Murdock and C. J. Horowitz, "Microscopic relativistic description of proton-nucleus scattering," Phys. Rev. C **35,** 1442 (1987).

[20] C. J. Horowitz and D. P. Murdock, "Quasielastic proton-nucleus scattering in a relativistic plane-wave impulse approximation," Phys. Rev. C **37,** 2032 (1988).

[21] O. V. Maxwell, "Energy-dependent Lorentz covariant representation of the NN interaction," Nucl. Phys. A **600,** 509 (1996).

[22] O. V. Maxwell, "Lorentz covariant representation of the NN interaction at energies above 500 MeV," Nucl. Phys. A **638,** 747 (1998).

[23] O. V. Maxwell and E. D. Cooper, "Elastic unitarity and the K-matrix in a Lorentz covariant representation of the NN interaction," Nucl. Phys. A **656,** 231 (1999).

[24] E. D. Cooper and O. V. Maxwell, "The $(p, 2p)$ reaction in the Dirac impulse approximation," Nucl. Phys. A **493,** 468 (1989).

[25] O. V. Maxwell and E. D. Cooper, "Proton-induced nucleon knockout from ^{40}Ca in the Dirac impulse approximation," Nucl. Phys. A **513,** 584 (1990).

[26] O. V. Maxwell and E. D. Cooper, "Proton knockout from ^{16}O and relativistic recoil effects in the Dirac impulse approximation," Nucl. Phys. A **565,** 740 (1993).

[27] O. V. Maxwell and E. D. Cooper, "Proton knockout from ^{16}O at 504 MeV and limitations of the DWIA," Nucl. Phys. A **574,** 819 (1994).

[28] O. V. Maxwell and E. D. Cooper, "Interaction dependence in a relativistic DWIA description of proton knockout," Nucl. Phys. A **603,** 441 (1996).

[29] Y. Ikebata, "$(p, 2p)$ reaction in zero-range and finite-range relativistic distorted-wave impulse approximation," Phys. Rev. C **52,** 890 (1995).

[30] J. Mano and Y. Kudo, "A Self-Consistent Description of $(p, 2p)$ Reactions in a Relativistic Finite-Range DWIA Model," Prog. Theor. Phys. **100,** 91 (1998).

[31] C. A. Miller *et al.*, "Spin-dependent scattering of deeply bound nucleons," Phys. Rev. C **57,** 1756 (1998).

[32] R. Neveling, A. A. Cowley, G. F. Steyn, S. V. Förtsch, G. C. Hillhouse, J. Mano, and S. M. Wyngaardt, "Analyzing power and cross section distributions of the knockout reaction ^{208}Pb$(\vec{p}, 2p)^{207}$Tl at an incident energy of 202 MeV," Phys. Rev. C **66,** 034602 (2002).

[33] D. L. Adams and M. Bleszynski, "On the relevance of the Dirac equation to the scattering of medium-energy nucleons from nuclei," Phys. Lett. B **136,** 10 (1984).

[34] J. A. Tjon and S. J. Wallace, "General Lorentz-invariant representation of NN scattering amplitudes," Phys. Rev. C **32,** 1667 (1985).

[35] B. I. S. van der Ventel and G. C. Hillhouse, "Sensitivity of exclusive proton knockout spin observables to different Lorentz invariant representations of the NN interaction," Phys. Rev. C **69,** 024618 (2004).

[36] J. D. Walecka, "A theory of highly condensed matter," Ann. Phys. (N.Y.) **83,** 491 (1974).

[37] C. J. Horowitz and B. D. Serot, "Self-consistent hartree description of finite nuclei in a relativistic quantum field theory," Nucl. Phys. A **368,** 503 (1981).

[38] B. D. Serot and J. D. Walecka, "The Relativistic Nuclear Many Body Problem," Adv. Nucl. Phys. **16,** 1 (1986).

[39] D. F. Jackson and T. Berggren, "Partial wave analysis of the $(p, 2p)$ reaction," Nucl. Phys. **62,** 353 (1965).

[40] A. Nadasen, P. Schwandt, P. P. Singh, W. W. Jacobs, A. D. Bacher, P. T. Debevec, M. D. Kaitchuck, and J. T. Meek, "Elastic scattering of 80-180 MeV protons and the proton-nucleus optical potential," Phys. Rev. C **23,** 1023 (1981).

[41] P. Schwandt, H. O. Meyer, W. W. Jacobs, A. D. Bacher, S. E. Vigdor, M. D. Kaitchuck, and T. R. Donoghue, "Analyzing power of proton-nucleus elastic scattering between 80 and 180 MeV," Phys. Rev. C **26,** 55 (1982).

[42] D. G. Madland, Los Alamos National Laboratory Report LA-UR-87-3382, 1987 (unpublished) .

[43] E. D. Cooper, B. C. Clark, R. Kozack, S. Shim, S. Hama, J. I. Johansson, H. S. Sherif, R. L. Mercer, and B. D. Serot, "Global optical potentials for elastic p+^{40}Ca scattering using the Dirac equation," Phys. Rev. C **36,** 2170 (1987).

[44] E. D. Cooper, B. C. Clark, S. Hama, and R. L. Mercer, "Dirac-global fits to calcium elastic scattering data in the range 21-200 MeV," Phys. Lett. B **206,** 588 (1988).

[45] S. Hama, B. C. Clark, E. D. Cooper, H. S. Sherif, and R. L. Mercer, "Global Dirac optical potentials for elastic proton scattering from heavy nuclei," Phys. Rev. C **41,** 2737 (1990).

[46] E. D. Cooper, S. Hama, B. C. Clark, and R. L. Mercer, "Global Dirac phenomenology for proton-nucleus elastic scattering," Phys. Rev. C **47,** 297 (1993).

[47] L. Antonuk, P. Kitching, C. A. Miller, D. A. Hutcheon, W. J. McDonald, G. C. Neilson, and W. C. Olsen, "An investigation of the ^{40}Ca$(p, 2p)$ reaction with polarised protons," Nucl. Phys. A **370,** 389 (1981).

[48] C. Samanta, N. S. Chant, P. G. Roos, A. Nadasen, J. Wesick, and A. A. Cowley, "Tests of the factorized distorted wave impulse approximation for $(p, 2p)$ reactions," Phys. Rev. C **34,** 1610 (1986).

[49] A. A. Cowley, J. J. Lawrie, G. C. Hillhouse, D. M. Whittal, S. V. Förtsch, J. V. Pilcher, F. D. Smit, and P. G. Roos, "Quasifree knockout in ^{16}O$(p, 2p)^{15}$N at an incident energy of 151 MeV," Phys. Rev. C **44,** 329 (1991).

[50] A. A. Cowley, G. J. Arendse, J. A. Stander, and W. A. Richter, "Distortion in proton-knockout reactions," Phys. Lett. B **359,** 300 (1995).

[51] A. A. Cowley *et al.*, "Rescattering in knockout reactions as manifested in ^{40}Ca$(p, p'p'')$ at an incident energy of 392 MeV," Phys. Rev. C **57,** 3185 (1998).

[52] G. C. Hillhouse, J. Mano, A. A. Cowley, and R. Neveling, "Relativistic predictions of exclusive ^{208}Pb$(\vec{p}, 2p)^{207}$Tl analyzing powers at an incident energy of 202 MeV," Phys. Rev. C **67,** 064604 (2003).

[53] G. C. Hillhouse, J. Mano, S. M. Wyngaardt, B. I. S. van der Ventel, T. Noro, and K. Hatanaka, "Relativistic predictions of spin observables for exclusive proton knockout reactions," Phys. Rev. C **68,** 034608 (2003).

[54] G. P. McCauley and G. E. Brown, "Inelastic Scattering of High Energy Nucleons by Complex Nuclei I: Semi-Classical Formalism," Proc. Phys. Soc. London **71,** 893 (1958).

[55] C. J. Joachain, *Quantum Collision Theory* (Elsevier, Amsterdam, 1975).

[56] D. Debruyne, J. Ryckebusch, W. Van Nespen, and S. Janssen, "Relativistic eikonal approximation in high-energy $A(e,e'p)$ reactions," Phys. Rev. C **62,** 024611 (2000).

[57] D. Debruyne, J. Ryckebusch, S. Janssen, and T. Van Cauteren, "Bridging two ways of describing final-state interactions in $A(e,e'p)$ reactions," Phys. Lett. B **527,** 62 (2002).

[58] D. Debruyne and J. Ryckebusch, "$A(e,e'p)$ reactions at GeV energies," Nucl. Phys. A **699,** 65 (2002).

[59] J. Ryckebusch, D. Debruyne, P. Lava, S. Janssen, B. Van Overmeire, and T. Van Cauteren, "Relativistic formulation of Glauber theory for $A(e,e'p)$ reactions," Nucl. Phys. A **728,** 226 (2003).

[60] A. Sommerfeld and J. Runge, "Anwendung der Vektorrechnung auf die Grundlagen der geometrischen Optik," Ann. Physik **340,** 277 (1911).

[61] M. Born and E. Wolf, *Principles of Optics* (Pergamon Press, Oxford, 1980).

[62] R. J. Glauber and G. Matthiae, "High-energy scattering of protons by nuclei," Nucl. Phys. B **21,** 135 (1970).

[63] S. J. Wallace, "High-energy expansion for nuclear multiple scattering," Phys. Rev. C **12,** 179 (1975).

[64] D. R. Yennie, "Interaction of High-Energy Photons with Nuclei as a Test of Vector-Meson-Dominance," in *Hadronic Interactions of Electrons and Photons*, J. Cummings and D. Osborn, eds., (Academic Press, New York, 1971), p. 321.

[65] J. D. Bjorken and S. D. Drell, *Relativistic Quantum Mechanics* (McGraw-Hill, New York, 1964).

[66] J. A. Caballero, T. W. Donnelly, E. Moya de Guerra, and J. M. Udías, "Analysis of factorization in $(e,e'p)$ reactions: A survey of the relativistic plane wave impulse approximation," Nucl. Phys. A **632,** 323 (1998).

[67] I. Yaron, L. Frankfurt, E. Piasetzky, M. Sargsian, and M. Strikman, "Investigation of the high momentum components of the nuclear wave function using hard quasielastic $A(p,2p)X$ reactions," Phys. Rev. C **66,** 024601 (2002).

[68] G. D. Alkhazov, S. L. Belostotsky, and A. A. Voroboyov, "Scattering of 1 GeV protons on nuclei," Phys. Rep. **42,** 89 (1978).

[69] J. R. Vignote, M. C. Martínez, J. A. Caballero, E. Moya de Guerra, and J. M. Udías, "$A(\vec{e}, e'\vec{p})B$ responses: From bare nucleons to complex nuclei," Phys. Rev. C **70,** 044608 (2004).

[70] R. D. Amado, J. Piekarewicz, D. A. Sparrow, and J. A. McNeil, "Dirac-eikonal scattering amplitude," Phys. Rev. C **28,** 1663 (1983).

[71] R. J. Glauber, in *Lectures in Theoretical Physics*, W. E. Brittin and L. G. Bunham, eds., (Interscience, New York, 1959), Vol. 1, p. 315.

[72] W. R. Greenberg and G. A. Miller, "Color transparency and Dirac-based spin effects in $(e, e'p)$ reactions," Phys. Rev. C **49,** 2747 (1994).

[73] H. Ito, S. E. Koonin, and R. Seki, "Spin-polarization response functions in high-energy $(\vec{e}, e'\vec{p})$ reactions," Phys. Rev. C **56,** 3231 (1997).

[74] A. Bianconi and M. Radici, "A test of the eikonal approximation in high-energy $(e, e'p)$ scattering," Phys. Lett. B **363,** 24 (1995).

[75] A. Bianconi and M. Radici, "Angular distributions for knockout and scattering of protons in the eikonal approximation," Phys. Rev. C **54,** 3117 (1996).

[76] M. Radici, W. H. Dickhoff, and E. R. Stoddard, "Consistency of spectroscopic factors from $(e, e'p)$ reactions at different momentum transfers," Phys. Rev. C **66,** 014613 (2002).

[77] G. R. Satchler, *Direct Nuclear Reactions* (Oxford University Press, Oxford, 1983).

[78] J. J. Kelly, "Effects of spinor distortion and density-dependent form factors upon quasifree ^{16}O$(\vec{e}, e'\vec{p})$," Phys. Rev. C **60,** 044609 (1999).

[79] R. H. Bassel and C. Wilkin, "High-Energy Proton Scattering and the Structure of Light Nuclei," Phys. Rev. **174,** 1179 (1968).

[80] L. L. Frankfurt, E. Moniz, M. Sargsyan, and M. I. Strikman, "Correlation effects in nuclear transparency," Phys. Rev. C **51,** 3435 (1995).

[81] N. N. Nikolaev, A. Szcurek, J. Speth, J. Wambach, B. G. Zakharov, and V. R. Zoller, "Multiple-scattering effects in the transverse-momentum distributions from $(e, e'p)$ reactions," Nucl. Phys. A **582,** 665 (1995).

[82] S. Jeschonnek and T. W. Donnelly, "Spin-orbit final-state interaction in the framework of Glauber theory for $(e, e'p)$ reactions," Phys. Rev. C **59,** 2676 (1999).

[83] O. Benhar, N. Nikolaev, J. Speth, A. Usmani, and B. Zakharov, "Final state interactions in ^{4}He$(e, e'p)^3$H at large proton energy," Nucl. Phys. A **673,** 241 (2000).

[84] A. Kohama, K. Yazaki, and R. Seki, "Correlation and finite interaction-range effects in high-energy electron inclusive scattering," Nucl. Phys. A **662,** 175 (2000).

[85] C. Ciofi degli Atti, L. P. Kaptari, and D. Treleani, "Effects of the final state interaction in the electrodisintegration of the deuteron at intermediate and high energies," Phys. Rev. C **63,** 044601 (2001).

[86] M. Petraki, E. Mavrommatis, O. Benhar, J. W. Clark, A. Fabrocini, and S. Fantoni, "Final-state interactions in the response of nuclear matter," Phys. Rev. C **67,** 014605 (2003).

[87] P. Lava, M. C. Martínez, J. Ryckebusch, J. A. Caballero, and J. M. Udías, "Nuclear transparencies in relativistic $A(e, e'p)$ models," Phys. Lett. B **595,** 177 (2004).

[88] P. Lava, J. Ryckebusch, B. Van Overmeire, and S. Strauch, "Polarization transfer in ^{4}He$(\vec{e}, e'\vec{p})$ and ^{16}O$(\vec{e}, e'\vec{p})$ in a relativistic Glauber model," Phys. Rev. C **71,** 014605 (2005).

[89] C. Lechanoine-LeLuc and F. Lehar, "Nucleon-nucleon elastic scattering and total cross sections," Rev. Mod. Phys. **65,** 47 (1993).

[90] S. J. Wallace, "High-Energy Proton Scattering," Adv. Nucl. Phys. **12,** 135 (1981).

[91] A. D. Krisch, "The Spin of the Proton," Scientific American **240,** 58 (1979).

[92] F. Bauer *et al.*, "Measurement of Spin Correlation Parameters A_{NN}, A_{SS}, and A_{SL} at 2.1 GeV in Proton-Proton Elastic Scattering," Phys. Rev. Lett. **90,** 142301 (2003).

[93] K. O. Eyser, R. Machleidt, W. Scobel, and the EDDA Collaboration, "Modelling nucleon-nucleon scattering above 1 GeV," Eur. Phys. J. A **22,** 105 (2004).

[94] K. Hagiwara *et al.*, "Review of Particle Physics," Phys. Rev. D **66,** 010001 (2002).

[95] Particle Data Group, http://pdg.lbl.gov .

[96] A. Dobrovolsky *et al.*, "Small angle pp scattering at energies from 650 to 1000 MeV," Nucl. Phys. B **214,** 1 (1983).

[97] B. Silverman *et al.*, "Differential cross sections and analyzing powers for small angle neutron-proton elastic scattering between 378 and 1135 MeV," Nucl. Phys. A **499,** 763 (1989).

[98] R. E. Hendrick and B. Lautrup, "Real parts of the forward elastic $\pi^{\pm}p$, $K^{\pm}p$, $\bar{p}p$, and pp scattering amplitudes from 1 to 200 GeV/c," Phys. Rev. D **11,** 529 (1975).

[99] A. A. Carter and D. V. Bugg, "The real part of the proton-neutron forward scattering amplitude," Phys. Lett. **20,** 203 (1966).

[100] C. J. Joachain and C. Quigg, "Multiple scattering expansions in several particele dynamics," Rev. Mod. Phys. **46,** 279 (1974).

[101] S. J. Wallace, "Eikonal Expansion," Phys. Rev. Lett. **27,** 622 (1971).

[102] S. J. Wallace, "Eikonal expansion," Ann. Phys. (N.Y.) **78,** 190 (1973).

[103] S. J. Wallace, "High-Energy Expansions of Scattering Amplitudes," Phys. Rev. D **8,** 1846 (1973).

[104] S. J. Wallace and J. A. McNeil, "Relativistic eikonal expansion," Phys. Rev. D **16,** 3565 (1977).

[105] S. J. Wallace and J. L. Friar, "Approximate Dirac scattering amplitudes: Eikonal expansion," Phys. Rev. C **29,** 956 (1984).

[106] D. Waxman, C. Wilkin, J.-F. Germond, and R. J. Lombard, "Eikonal corrections for spin-orbit potentials," Phys. Rev. C **24,** 578 (1981).

[107] G. Fäldt, A. Ingemarsson, and J. Mahalanabis, "Numerical investigation of non-eikonal corrections to the Glauber model at intermediate energies," Phys. Rev. C **46,** 1974 (1992).

[108] F. Carstoiu and R. J. Lombard, "Eikonal expansion for total cross sections of heavy ion reactions," Phys. Rev. C **48,** 830 (1993).

[109] M. H. Cha and Y. J. Kim, "Higher-order corrections to the eikonal phase shifts for heavy-ion elastic collision," Phys. Rev. C **51,** 212 (1995).

[110] J. S. Al-Khalili, J. A. Tostevin, and J. M. Brooke, "Beyond the eikonal model for few-body systems," Phys. Rev. C **55,** R1018 (1997).

[111] C. E. Aguiar, F. Zardi, and A. Vitturi, "Low-energy extensions of the eikonal approximation to heavy-ion scattering," Phys. Rev. C **56,** 1511 (1997).

[112] J. A. Tjon and S. J. Wallace, "Coulomb corrections in quasielastic scattering based on the eikonal expansion for electron wave functions," Phys. Rev. C **74,** 064602 (2006).

[113] A. Baker, "Second-Order Eikonal Approximation for Potential Scattering," Phys. Rev. D **6,** 3462 (1972).

[114] S. L. Belostotsky *et al.*, "Quasielastic proton scattering at 1.0 GeV," In *Proceedings of the International Symposium on Modern Developments in Nuclear Physics*, p. 191 (Novosibirsk, 1987).

[115] H. Tyrén, S. Kullander, O. Sundberg, R. Ramachandran, P. Isacsson, and T. Berggren, "Quasi-free proton-proton scattering in light nuclei at 460 MeV," Nucl. Phys. **79,** 321 (1966).

[116] W. J. McDonald *et al.*, "Quasi-free nucleon scattering on ^{16}O," Nucl. Phys. A **456,** 577 (1986).

[117] B. Van Overmeire, W. Cosyn, P. Lava, and J. Ryckebusch, "Relativistic eikonal description of $A(p, pN)$ reactions," Phys. Rev. C **73,** 064603 (2006).

[118] K. Hatanaka *et al.*, "Exclusive Measurement of Proton Quasifree Scattering and Density Dependence of the Nucleon-Nucleon Interaction," Phys. Rev. Lett. **78,** 1014 (1997).

[119] L. R. B. Elton and O. Sundberg, "Nuclear structure information from high-energy $(p, 2p)$ experiments," Nucl. Phys. A **187,** 314 (1972).

[120] V. Pandharipande, I. Sick, and P. K. A. deWitt Huberts, "Independent particle motion and correlations in fermion systems," Rev. Mod. Phys. **69,** 981 (1997).

[121] G. J. Kramer, Ph.D. thesis, University of Amsterdam, 1990.

[122] A. H. Mueller, "Topics in high energy perturbative QCD including interactions with nuclear matter," In *Proceedings of the XVII Rencontre de Moriond, Les Arcs, France*, J. Tran Thanh Van, ed., p. 13 (Editions Frontières, Gif-sur-Yvette, 1982).

[123] S. J. Brodsky, "Breakdown of QCD factorization theorems for inclusive reactions," In *Proceedings of the XIII International Symposium on Multiparticle Dynamics, Volendam, The Netherlands*, E. W. Kittel, W. Metzger, and A. Stergiou, eds., p. 963 (World Scientific, Singapore, 1982).

[124] A. Carroll *et al.*, "Nuclear Transparency to Large-Angle pp Elastic Scattering," Phys. Rev. Lett. **61,** 1698 (1988).

[125] I. Mardor *et al.*, "Nuclear Transparency in Large Momentum Transfer Quasielastic Scattering," Phys. Rev. Lett. **81,** 5085 (1998).

[126] A. Leksanov *et al.*, "Energy Dependence of Nuclear Transparency in $C(p, 2p)$ Scattering," Phys. Rev. Lett. **87,** 212301 (2001).

[127] A. W. Hendry, "Evidence for coherent effects in large-angle hadron-hadron scattering," Phys. Rev. D **10,** 2300 (1974).

[128] D. P. Owen, F. C. Peterson, J. Orear, A. L. Read, D. G. Ryan, D. H. White, A. Ashmore, C. J. S. Damerell, W. R. Frisken, and R. Rubinstein, "High-Energy

Elastic Scattering of $\pi^{\pm}$, K^{-}, and p^{-} on Hydrogen at c.m. Angles from 22° to 180°," Phys. Rev. **181,** 1794 (1969).

[129] K. A. Jenkins, L. E. Price, R. Klem, R. J. Miller, P. Schreiner, H. Courant, Y. I. Makdisi, M. L. Marshak, E. A. Peterson, and K. Ruddick, "Measurement of the Energy Dependence of Elastic πp and pp Scattering at Large Angles," Phys. Rev. Lett. **40,** 425 (1978).

[130] K. A. Jenkins, L. E. Price, R. Klem, R. J. Miller, P. Schreiner, H. Courant, Y. I. Makdisi, M. L. Marshak, E. A. Peterson, and K. Ruddick, "Fluctuations in Large-Angle $\pi^{\pm}p$ Elastic Scattering," Phys. Rev. Lett. **40,** 429 (1978).

[131] K. A. Jenkins, L. E. Price, R. Klem, R. J. Miller, P. Schreiner, M. L. Marshak, E. A. Peterson, and K. Ruddick, "Measurement of wide-angle elastic scattering of pions and protons off protons," Phys. Rev. D **21,** 2445 (1980).

[132] C. Baglin *et al.*, "An experimental study of large-angle elastic scattering of charged mesons and antiprotons on protons at 20 and 30 GeV/c incident momenta," Nucl. Phys. B **216,** 1 (1983).

[133] J. Blazey, Ph.D. thesis, University of Minnesota, 1986.

[134] P. Jain, B. Kundu, and J. P. Ralston, "Oscillating color transparency in $\pi A \to \pi p(A-1)$ and $\gamma A \to \pi N(A-1)$," Phys. Rev. D **65,** 094027 (2002).

[135] L. Y. Zhu *et al.*, "Cross-Section Measurement of Charged-Pion Photoproduction from Hydrogen and Deuterium," Phys. Rev. Lett. **91,** 022003 (2003).

[136] L. Y. Zhu *et al.*, "Cross section measurements of charged pion photoproduction in hydrogen and deuterium from 1.1 to 5.5 GeV," Phys. Rev. C **71,** 044603 (2005).

[137] R. L. Anderson, D. B. Gustavson, D. M. Ritson, G. A. Weitsch, H. J. Halpern, R. Prepost, D. H. Tompkins, and D. E. Wisner, "Measurements of exclusive photoproduction processes at large values of t and u from 4 to 7.5 GeV," Phys. Rev. D **14,** 679 (1976).

[138] J. Napolitano *et al.*, "Measurement of the Differential Cross Section for the reaction ^{2}H(γ, p)n at High Photon Energies and $\theta_{\mathrm{c.m.}} = 90°$," Phys. Rev. Lett. **61,** 2530 (1988).

[139] S. J. Freedman *et al.*, "Two-body disintegration of the deuteron with 0.8-1.8 GeV photons," Phys. Rev. C **48,** 1864 (1993).

[140] J. E. Belz *et al.*, "Two-Body Photodisintegration of the Deuteron up to 2.8 GeV," Phys. Rev. Lett. **74,** 646 (1995).

[141] C. Bochna *et al.*, "Measurements of Deuteron Photodisintegration up to 4.0 GeV," Phys. Rev. Lett. **81,** 4576 (1998).

[142] E. C. Schulte *et al.*, "Measurement of the High Energy Two-Body Deuteron Photodisintegration Differential Cross Section," Phys. Rev. Lett. **87,** 102302 (2001).

[143] L. L. Frankfurt, G. A. Miller, M. M. Sargsian, and M. I. Strikman, "QCD Rescattering and High Energy Two-Body Photodisintegration of the Deuteron," Phys. Rev. Lett. **84,** 3045 (2000).

[144] J. P. Ralston and B. Pire, "Fluctuating Proton Size and Oscillating Color Transparency," Phys. Rev. Lett. **61,** 1823 (1988).

[145] S. J. Brodsky and G. F. de Teramond, "Spin Correlations, QCD Color Transparency, and Heavy-Quark Thresholds in Proton-Proton Scattering," Phys. Rev. Lett. **60,** 1924 (1988).

[146] J. P. Ralston and B. Pire, "Quantum color transparency," Phys. Rev. Lett. **65,** 2343 (1990).

[147] P. Jain, B. Pire, and J. P. Ralston, "Quantum color transparency and nuclear filtering," Phys. Rep. **271,** 67 (1996).

[148] G. R. Farrar, H. Liu, L. L. Frankfurt, and M. I. Strikman, "Transparency in Nuclear Quasiexclusive Processes with Large Momentum Transfer," Phys. Rev. Lett. **61,** 686 (1988).

[149] B. K. Jennings and G. A. Miller, "Energy dependence of color transparency," Phys. Rev. D **44,** 692 (1991).

[150] B. Van Overmeire and J. Ryckebusch, "A relativistic framework to determine the nuclear transparency from $A(p, 2p)$ reactions," Phys. Lett. B **644,** 304 (2007).

[151] S. C. Pieper and R. B. Wiringa, "Quantum Monte Carlo Calculations of Light Nuclei," Ann. Rev. Nucl. Part. Sci. **51,** 53 (2001).

[152] P. Jain and J. P. Ralston, "Exclusive Hadronic Processes and Color Transparency," Pramana **57,** 433 (2001).

[153] H. Gao, "Exclusive processes at Jefferson Lab," Pramana **61,** 837 (2003).

[154] C. G. White *et al.*, "Comparison of 20 exclusive reactions at large t," Phys. Rev. D **49,** 58 (1994).

[155] S. J. Brodsky and G. R. Farrar, "Scaling Laws at Large Transverse Momentum," Phys. Rev. Lett. **31,** 1153 (1973).

[156] S. J. Brodsky and G. R. Farrar, "Scaling laws for large-momentum-transfer processes," Phys. Rev. D **11,** 1309 (1975).

[157] V. A. Matveev, R. M. Muradian, and A. N. Tavkhelidze, "Automodellism in the large-angle elastic scattering and structure of hadrons," Lett. Nuovo Cimento **7,** 719 (1973).

[158] G. P. Lepage and S. J. Brodsky, "Exclusive processes in perturbative quantum chromodynamics," Phys. Rev. D **22,** 2157 (1980).

[159] D. Sivers, S. J. Brodsky, and R. Blankenbecler, "Large transverse momentum processes," Phys. Rep. **23,** 1 (1976).

[160] G. C. Blazey *et al.*, "Hard Scattering with Exclusive Reactions: $\pi^- p$ Elastic Scattering and ρ-Meson Production," Phys. Rev. Lett. **55,** 1820 (1985).

[161] B. R. Baller *et al.*, "Comparison of exclusive reactions at large t," Phys. Rev. Lett. **60,** 1118 (1988).

[162] S. J. Brodsky and G. P. Lepage, "Helicity selection rules and tests of gluon spin in exclusive quantum-chromodynamic processes," Phys. Rev. D **24,** 2848 (1981).

[163] K. Wijesooriya *et al.*, "Polarization Measurements in High-Energy Deuteron Photodisintegration," Phys. Rev. Lett. **86,** 2975 (2001).

[164] K. Wijesooriya *et al.*, "Polarization measurements in neutral pion photoproduction," Phys. Rev. C **66,** 034614 (2002).

[165] D. Abbott *et al.*, "Measurement of Tensor Polarization in Elastic Electron-Deuteron Scattering at Large Momentum Transfer," Phys. Rev. Lett. **84,** 5053 (2000).

[166] F. Adamian *et al.*, "Measurement of the cross-section asymmetry of deuteron photodisintegration process by linearly polarized photons in the energy range $E_\gamma = 0.8$–1.6 GeV," Eur. Phys. J. A **8,** 423 (2000).

[167] T. Gousset, B. Pire, and J. P. Ralston, "Hadron helicity violation in exclusive processes: Quantitative calculations in leading order QCD," Phys. Rev. D **53,** 1202 (1996).

[168] J. P. Ralston and P. Jain, "QCD Form Factors and Hadron Helicity Non-Conservation," Phys. Rev. D **69,** 053008 (2004).

[169] D. G. Crabb *et al.*, "Spin Dependence of High-$P_\perp^2$ Elastic $p-p$ Scattering," Phys. Rev. Lett. **41,** 1257 (1978).

[170] E. A. Crosbie *et al.*, "Energy dependence of spin-spin effects in $p-p$ elastic scattering at $90^\circ_{\mathrm{c.m.}}$," Phys. Rev. D **23,** 600 (1981).

[171] S. L. Linn *et al.*, "Measurements of spin parameters in $p-p$ elastic scattering at 6 GeV/c," Phys. Rev. D **26,** 550 (1982).

[172] T. S. Bhatia *et al.*, "Spin Correlation for pp Elastic Scattering at $\theta_{\mathrm{c.m.}} = \pi/2$ in the Energy Region of Dibaryon Resonances," Phys. Rev. Lett. **49,** 1135 (1982).

[173] G. R. Court *et al.*, "Energy Dependence of Spin Effects in $p_\uparrow + p_\uparrow \to p + p$," Phys. Rev. Lett. **57,** 507 (1986).

[174] N. Isgur and C. H. Llewellyn Smith, "Asymptotic Q^2 for Exclusive Processes in Quantum Chromodynamics," Phys. Rev. Lett. **52,** 1080 (1984).

[175] A. V. Radyushkin, "Sum Rules And Exclusive Processes In QCD," Acta Phys. Polon. B **15,** 403 (1984).

[176] A. P. Bakulev and A. V. Radyushkin, "Nonlocal condensates and QCD sum rules for the pion form-factor," Phys. Lett. B **271,** 223 (1991).

[177] G. Sterman and P. Stoler, "Hadronic Form Factors and Perturbative QCD," Ann. Rev. Nucl. Part. Sci. **47,** 193 (1997).

[178] B. Pire and J. P. Ralston, "Fixed angle elastic scattering and the chromo-Coulomb phase shift," Phys. Lett. B **117,** 233 (1982).

[179] P. V. Landshoff and J. C. Polkinghorne, "Models for hadronic and leptonic processes at high energy," Phys. Rep. **5,** 1 (1972).

[180] P. V. Landshoff, "Model for elastic scattering at wide angle," Phys. Rev. D **10,** 1024 (1974).

[181] P. V. Landshoff and D. J. Pritchard, "Higher Order QCD Corrections to Exclusive Processes: the Multiple Scattering Mechanism," Z. Phys. C **6,** 69 (1980).

[182] J. C. Polkinghorne, "Quark-Quark Interactions and High Energy Processes," Phys. Lett. B **49,** 277 (1974).

[183] V. V. Sudakov, "Vertex parts at very high energies in quantum electrodynamics," Sov. Phys. JETP **3,** 65 (1956).

[184] A. H. Mueller, "Perturbative QCD at high energies," Phys. Rep. **73,** 237 (1981).

[185] J. Botts and G. Sterman, "Sudakov effects in hadron-hadron elastic scattering," Phys. Lett. B **224,** 201 (1989).

[186] J. Botts and G. Sterman, "Sudakov effects in hadron-hadron elastic scattering: J. Botts and G. Sterman, Phys. Lett. B 224 (1989) 201," Phys. Lett. B **227,** 501(E) (1989).

[187] J. P. Ralston and B. Pire, "Oscillatory Scaling Violations and the Quantum Chromodynamic Coulomb Phase," Phys. Rev. Lett. **49,** 1605 (1982).

[188] A. Sen, "Asymptotic behavior of the fixed-angle on-shell quark scattering amplitudes in non-Abelian gauge theories," Phys. Rev. D **28,** 860 (1983).

[189] G. B. West and D. R. Yennie, "Coulomb Interference in High-Energy Scattering," Phys. Rev. **172,** 1413 (1968).

[190] V. Franco, "Coulomb-Nuclear Interference," Phys. Rev. D **7,** 215 (1973).

[191] D. Zwanziger, "Reduction Formulas for Charged Particles and Coherent States in Quantum Electrodynamics," Phys. Rev. D **7,** 1082 (1973).

[192] L. L. Frankfurt, E. Piasetsky, M. M. Sargsyan, and M. I. Strikman, "Probing short-range nucleon correlations in high-energy hard quasielastic pd reactions," Phys. Rev. C **51,** 890 (1995).

[193] R. J. Furnstahl, B. D. Serot, and H.-B. Tang, "A chiral effective lagrangian for nuclei," Nucl. Phys. A **615,** 441 (1997).

[194] L. L. Frankfurt and M. I. Strikman, "High-energy phenomena, short-range nuclear structure and QCD," Phys. Rep. **76,** 215 (1981).

[195] L. L. Frankfurt and M. I. Strikman, "Color Screening and Color Transparency in Hard Nuclear Processes," Prog. Part. Nucl. Phys. **27,** 135 (1991).

[196] L. L. Frankfurt, W. R. Greenberg, G. A. Miller, and M. I. Strikman, "Sum rule description of color transparency," Phys. Rev. C **46,** 2547 (1992).

[197] L. L. Frankfurt, G. A. Miller, and M. I. Strikman, "The Geometrical Color Optics Of Coherent High Energy Processes," Annu. Rev. Nucl. Part. Sci. **44,** 501 (1994).

[198] F. E. Low, "Model of the bare Pomeron," Phys. Rev. D **12,** 163 (1975).

[199] S. Nussinov, "Colored-Quark Version of Some Hadronic Puzzles," Phys. Rev. Lett. **34,** 1286 (1975).

[200] J. F. Gunion and D. E. Soper, "Quark-counting and hadron-size effects for total cross sections," Phys. Rev. D **15,** 2617 (1977).

[201] S. J. Brodsky and A. H. Mueller, "Using nuclei to probe hadronization in QCD," Phys. Lett. B **206,** 685 (1988).

[202] L. Frankfurt, G. A. Miller, and M. Strikman, "Color transparency phenomenon and nuclear physics," Comm. Nucl. Part. Phys. **21,** 1 (1992).

[203] L. L. Frankfurt and M. I. Strikman, "Hard nuclear processes and microscopic nuclear structure," Phys. Rep. **160,** 235 (1988).

[204] B. K. Jennings and G. A. Miller, "Realistic Hadronic Matrix Element Approach to Color Transparency," Phys. Rev. Lett. **69,** 3619 (1992).

[205] L. L. Frankfurt and M. I. Strikman, "Point-like configurations in hadrons and nuclei and deep inelastic reactions with leptons: EMC and EMC-like effects," Nucl. Phys. B **250,** 143 (1985).

[206] I. Mardor, Ph.D. thesis, Tel-Aviv University, 1997.

[207] J. Aclander *et al.*, "Nuclear transparency in $90^{\circ}_{\rm c.m.}$ quasielastic $A(p,2p)$ reactions," Phys. Rev. C **70,** 015208 (2004).

[208] C. Ciofi degli Atti and S. Simula, "Realistic model of the nucleon spectral function in few- and many-nucleon systems," Phys. Rev. C **53,** 1689 (1996).

[209] T.-S. H. Lee and G. A. Miller, "Color transparency and high-energy $(p,2p)$ nuclear reactions," Phys. Rev. C **45,** 1863 (1992).

[210] B. K. Jennings and G. A. Miller, "Color transparency and non-perturbative contributions to high energy (p,pp) reactions," Phys. Lett. B **274,** 442 (1992).

[211] S. Frankel, W. Frati, and N. R. Walet, "Extracting nuclear transparency from $p,2p-A$ and $e,e'p-A$ cross sections," Nucl. Phys. A **580,** 595 (1994).

[212] B. K. Jennings and G. A. Miller, "Color transparency in (p,pp) reactions," Phys. Lett. B **318,** 7 (1993).

[213] P. Jain and J. P. Ralston, "Systematic analysis method for color transparency experiments," Phys. Rev. D **48,** 1104 (1993).

[214] N. C. R. Makins *et al.*, "Momentum transfer dependence of nuclear transparency from the $^{12}C(e,e'p)$ reaction," Phys. Rev. Lett. **72,** 1986 (1994).

[215] T. G. O'Neill *et al.*, "A-dependence of nuclear transparency in quasielastic $A(e,e'p)$ at high Q^2," Phys. Lett. B **351,** 87 (1995).

[216] D. Abbott *et al.*, "Quasifree $(e,e'p)$ Reactions and Proton Propagation in Nuclei," Phys. Rev. Lett. **80,** 5072 (1998).

[217] K. Garrow *et al.*, "Nuclear transparency from quasielastic $A(e,e'p)$ reactions up to $Q^2 = 8.1\,(GeV/c)^2$," Phys. Rev. C **66,** 044613 (2002).

[218] D. Dutta *et al.*, "Quasielastic $(e,e'p)$ reaction on ^{12}C, ^{56}Fe, and ^{197}Au," Phys. Rev. C **68,** 064603 (2003).

[219] N. N. Nikolaev, A. Szczurek, J. Speth, J. Wambach, B. G. Zakharov, and V. R. Zoller, "Theoretical interpretation of the NE18 experiment on nuclear transparency in $A(e,e'p)$ scattering," Phys. Rev. C **50,** R1296 (1994).

[220] L. L. Frankfurt, M. I. Strikman, and M. B. Zhalov, "Pitfalls in looking for color transparency at intermediate energies," Phys. Rev. C. **50,** 2189 (1994).

[221] P. Lava, Ph.D. thesis, Ghent University, 2006.

[222] G. Garino *et al.*, "Proton propagation in nuclei studied in the $(e,e'p)$ reaction," Phys. Rev. C **45,** 780 (1992).

[223] D. Rohe *et al.*, "Nuclear transparency from quasielastic ^{12}C$(e,e'p)$," Phys. Rev. C **72,** 054602 (2005).

[224] S. Heppelmann, "Color transparency and nuclear filtering," Nucl. Phys. B Proc. Suppl. **12,** 159 (1990).

[225] J. Botts and G. Sterman, "Hard elastic scattering in QCD: Leading behavior," Nucl. Phys. B **325,** 62 (1989).

[226] J. Botts, "The multiple scattering contribution to fixed-angle elastic hadron-hadron scattering," Nucl. Phys. B **353,** 20 (1991).

[227] J. Botts, J.-W. Qiu, and G. Sterman, "Elastic amplitudes and power corrections in QCD," Nucl. Phys. A **527,** 577 (1991).

[228] D. Dutta and H. Gao, "Generalized counting rule and oscillatory scaling," Phys. Rev. C **71,** 032201(R) (2005).

[229] J-PARC home page, http://j-parc.jp/index-e.html .

[230] S. Kumano, "Hadron Physics at J-PARC," hep-ph/0608105 .

[231] A. Ivanilov, private communication.

[232] J. J. Kelly, "Nucleon Knockout by Intermediate Energy Electrons," Adv. Nucl. Phys. **23,** 75 (1996).

[233] T. de Forest, "Off-shell electron-nucleon cross sections: The impulse approximation," Nucl. Phys. A **392,** 232 (1983).

[234] J. M. Udías, P. Sarriguren, E. Moya de Guerra, E. Garrido, and J. A. Caballero, "Spectroscopic factors in ^{40}Ca and ^{208}Pb from $(e, e'p)$: Fully relativistic analysis," Phys. Rev. C **48,** 2731 (1993).

[235] R. J. Woo *et al.*, "Measurement of the Induced Proton Polarization P_n in the $^{12}\mathrm{C}(e, e'\vec{p})$ Reaction," Phys. Rev. Lett. **80,** 456 (1998).

[236] J. M. Udías and J. R. Vignote, "Relativistic nuclear structure effects in $(e, e'\vec{p})$," Phys. Rev. C **62,** 034302 (2000).

[237] J. Ryckebusch, D. Debruyne, W. Van Nespen, and S. Janssen, "Meson and isobar degrees of freedom in $A(\vec{e}, e'\vec{p})$ reactions at $0.2 \leq Q^2 \leq 0.8$ (GeV/c)^2," Phys. Rev. C **60,** 034604 (1999).

[238] J. Gao *et al.*, "Dynamical Relativistic Effects in Quasielastic $1p$-Shell Proton Knockout from ^{16}O," Phys. Rev. Lett. **84,** 3265 (2000).

[239] K. G. Fissum *et al.*, "Dynamics of the quasielastic $^{16}\mathrm{O}(e, e'p)$ reaction at $Q^2 \approx 0.8$ (GeV/c)^2," Phys. Rev. C **70,** 034606 (2004).

[240] J. J. Kelly, "Influence of the Dirac sea on proton electromagnetic knockout," Phys. Rev. C **72,** 014602 (2005).

[241] L. Chinitz *et al.*, "Separation of the Interference Response Function R_{LT} in the ^{16}O$(e, e'p)^{15}$N Reaction," Phys. Rev. Lett. **67,** 568 (1991).

[242] M. C. Martínez, P. Lava, N. Jachowicz, J. Ryckebusch, K. Vantournhout, and J. M. Udías, "Relativistic models for quasielastic neutrino scattering," Phys. Rev. C **73,** 024607 (2006).

[243] P. Lava, N. Jachowicz, M. C. Martínez, and J. Ryckebusch, "Nucleon helicity asymmetries in quasielastic neutrino-nucleus interactions," Phys. Rev. C **73,** 064605 (2006).

[244] W. Cosyn, M. C. Martínez, J. Ryckebusch, and B. Van Overmeire, "Nuclear transparencies from photoinduced pion production," Phys. Rev. C **74,** 062201(R) (2006).

[245] B. D. Serot, "Quantum hadrodynamics," Rep. Prog. Phys. **55,** 1855 (1992).

[246] P. Ring, "Relativistic mean field theory in finite nuclei," Prog. Part. Nucl. Phys. **37,** 193 (1996).

[247] B. D. Serot and J. D. Walecka, "Recent Progress in Quantum Hadrodynamics," Int. J. Mod. Phys. E **6,** 515 (1997).

[248] R. J. Furnstahl and B. D. Serot, "Quantum Hadrodynamics: Evolution and Revolution," Comm. Nucl. Part. Phys. **2,** A23 (2000).

[249] B. D. Serot, "A relativistic nuclear field theory with π and ρ mesons," Phys. Lett. B **86,** 146 (1979).

[250] R. J. Furnstahl, H.-B. Tang, and B. D. Serot, "Vacuum contributions in a chiral effective Lagrangian for nuclei," Phys. Rev. C **52,** 1368 (1995).

[251] R. J. Furnstahl, B. D. Serot, and H.-B. Tang, "Analysis of chiral mean-field models for nuclei," Nucl. Phys. A **598,** 539 (1996).

[252] L. D. Miller and A. E. S. Green, "Relativistic Self-Consistent Meson Field Theory of Spherical Nuclei," Phys. Rev. C **5,** 241 (1972).

[253] J. D. Walecka, *Electron Scattering for Nuclear and Nucleon Structure* (Cambridge University Press, Cambridge, 2001).

[254] H. De Vries, C. W. De Jager, and C. De Vries, "Nuclear charge-density-distribution parameters from elastic electron scattering," At. Data Nucl. Data Tables **36,** 495 (1987).

[255] J. Carlson and R. Schiavilla, "Structure and dynamics of few-nucleon systems," Rev. Mod. Phys. **70,** 743 (1998).

Nederlandstalige samenvatting

1 Inleiding

De ontdekking van de atoomkern door Rutherford in het begin van de 20ste eeuw luidde de geboorte in van de kernfysica. De interesse in dit deelgebied van de fysica vloeit voort uit het feit dat de kern een dicht veeldeeltjessysteem van protonen en neutronen is. Als zodanig levert de kern ons een uniek microscopisch kader om de verschillende fundamentele krachten (de sterke, de elektromagnetische en de zwakke wiselwerking) te onderzoeken. Bovendien bestaat meer dan 99.9% van de massa in het universum uit nucleaire materie. Bijgevolg speelt de kernfysica een cruciale rol in het doorgronden van onze wereld, van het infinitesimale tot het astronomische.

Om informatie te bekomen over de kernstructuur en -dynamica zijn verstrooiingsprocessen aan kernen zeer geschikt. Leptonische probes interageren slechts zwak met de kern en kunnen het ganse nucleaire volume aftasten. Hadronische verstrooiing daarentegen brengt grotere werkzame doorsnedes met zich mee en heeft dus een groot ontdekkingspotentieel, terwijl leptonische reacties eerder gebruikt worden voor precisie-experimenten. Door de sterke interactie met de trefkern is de theoretische modellering van hadronische verstrooiing echter veel uitdagender en tasten hadronische probes slechts het oppervlak van de kern grondig af. Het grootste deel van dit werk is gewijd aan hadron-geïnduceerde verstrooiing, meer bepaald aan exclusieve proton-kern reacties in het quasi-elastisch gebied. In dit gebied verwacht men dat het projectiel de uitstoot van één enkel nucleon teweeg brengt. Dit nucleon wordt samen met het verstrooide proton gedetecteerd.

2 Theoretisch model voor $A(p, pN)$ reacties

De modellering van deze exclusieve proton-geïnduceerde $A(p, pN)$ processen valt uiteen in drie deelproblemen:

- de beschrijving van de harde verstrooiing die de uitstoot van een gebonden nucleon veroorzaakt,
- de beschrijving van de structuur van de doelwit- en restkern,
- de behandeling van de zachte initiële- en finale-toestandsinteracties (IFSI) die het inkomend en de twee uitgaande nucleonen aangaan met het kernmedium.

Wat de behandeling van de harde verstrooiing betreft bestaan er twee verschillende methodes. In ons model werd uitgegaan van de zogenaamde werkzame-doorsnede-gefactoriseerde benadering waarbij de vrije NN werkzame doorsnede als een evenredigheidsfactor optreedt in de differentiële $A(p, pN)$ werkzame doorsnede. Deze techniek faalt echter wanneer in de beschrijving van de IFSI een spinafhankelijkheid in rekening wordt gebracht. In dat geval biedt de ontkoppeling van de harde NN verstrooiing en de nucleaire dynamica op amplitudeniveau een alternatief.

Voor de beschrijving van de kernstructuur hebben we een beroep gedaan op het schillenmodel. Hierin veronderstelt men dat de nucleonen onafhankelijk van elkaar bewegen in een gemiddeld-veldpotentiaal die de sterke interactie met het omringend kernmedium beschrijft (onafhankelijk-deeltjesmodel). De initiële- en finale-toestandsgolffuncties nemen dan ook de Slater-determinantvorm aan waarbij de relativistische gebonden-toestand één-deeltjesgolffuncties bepaald worden in de Hartreebenadering van het $\sigma - \omega$ model.

Het resterende ingrediënt in $A(p, pN)$ modellen betreft de propagatie van het invallend, het verstrooid en het uitgestoten nucleon doorheen de kern en hun interacties met de nucleonen in de restkern. De interpretatie van alle quasi-elastische nucleon-uitstootreacties hangt zeer sterk af van de beschikbaarheid van realistische modellen voor de beschrijving van deze IFSI effecten. Met drie nucleonen onderhevig aan IFSI is dit zeker het geval voor $A(p, pN)$ reacties en de verschillende methodes om IFSI te behandelen worden dan ook uitvoerig besproken. In

de meeste theoretische $A(p, pN)$ studies worden de IFSI effecten berekend binnen de context van de verstoorde-golf impulsbenadering (DWIA). Hierin worden de verstrooiingsgolffuncties bepaald door middel van partiële-golfontwikkelingen van de exacte oplossingen en worden de IFSI in rekening gebracht met behulp van nucleon-kern optische potentialen. Parametrisaties voor deze optische potentialen worden niet bepaald uit theoretische overwegingen, maar steunen op empirische gegevens van elastische nucleon-kern verstrooiingsprocessen. Bij nucleon kinetische energieën hoger dan 1 GeV worden deze DWIA modellen problematisch omwille van drie redenen. Ten eerste worden de partiële-golfexpansies alsmaar moeilijker te hanteren bij hogere energieën vermits het aantal partiële golven dat nodig is om convergentie te bereiken, steeds groter wordt. Daarnaast zijn globale parametrisaties van de optische potentialen gewoonlijk beperkt tot kinetische energieën lager dan 1 GeV. Ten derde lijken optische-potentiaalmodellen ook onnatuurlijk voor de modellering van de IFSI bij hoge-energieverstrooiing wegens het sterk inelastisch, absorberend en diffractief karakter van de onderliggende elementaire nucleon-nucleon interactie.

Een alternatieve beschrijving van de IFSI wordt geleverd door de eikonale benadering. Deze benadering vindt haar oorsprong in de optica en behoort tot de groep van semi-klassieke benaderingstechnieken die nuttig worden wanneer de de Broglie golflengte van het deeltje zeer klein is in vergelijking met de dracht van de potentiaal waaraan het deeltje onderhevig is. Daarnaast wordt verondersteld dat de sterkte van de potentiaal veel kleiner is dan de energie van het deeltje. Het gebruik van de eikonale methode is gerechtvaardigd voor botsingen over kleine hoeken en bijgevolg staat deze techniek ook bekend als de kleine-hoekbenadering.

In deze thesis werd een relativistisch $A(p, pN)$ formalisme gebaseerd op de eikonale benadering uitgewerkt. Hierbij werden spineffecten in de IFSI verwaarloosd om factorisatie op het niveau van de werkzame doorsnede toe te laten. Ons eikonaal model is zeer flexibel aangezien het zowel in combinatie met relativistische optische potentialen (ROMEA) als in een Glauber veelvoudige-verstrooiingsaanpak (RMSGA) kan gebruikt worden. De keuzemogelijkheid tussen deze twee verschillende technieken om de IFSI te behandelen laat ons toe om $A(p, pN)$ reacties te beschrijven in een groot energiegebied.

Net als in de talloze DWIA modellen worden in het ROMEA formalisme de IFSI effecten geïmplementeerd in termen van optische potentialen. Het ROMEA formalisme steunt evenwel niet op een partiële-golfontwikkeling, maar op de eikonale benadering om de verstrooiingsgolffunctie te berekenen. Hierdoor is het ROMEA formalisme beter geschikt om verstrooiing bij hogere energieën te beschrijven.

Bij kinetische energieën hoger dan 1 GeV kan de ROMEA aanpak niet langer gewettigd worden omwille van de eerder vermelde nadelen van optische potentialen. In dit hoge-energiegebied biedt Glaubertheorie soelaas. Deze theorie is een veeldeeltjesveralgemening van de eikonale benadering en herstelt de link met de fundamentele nucleon-nucleon verstrooiing via de introductie van een profielfunctie. Verder postuleert ons RMSGA model lineaire banen en bevroren toeschouwernucleonen. Het belangrijkste verschil tussen de ROMEA en RMSGA modellen is dus dat het ROMEA model de IFSI ziet als nucleon-kern interacties, terwijl het RMSGA model uitgaat van een nucleon-nucleon beeld.

3 Numerieke resultaten: de IFSI factor en $A(p, pN)$ differentiële werkzame doorsnedes

In onze code zit het volledige effect van de IFSI vervat in de zogenaamde IFSI factor. De eigenschappen van deze functie werden onderzocht voor quasi-elastische protonverstrooiing aan ^{12}C, ^{16}O en ^{40}Ca bij een inkomende protonenergie van 1 GeV. Dit komt overeen met de kinematiek van het PNPI experiment uitgevoerd door S. L. Belostotsky e.a. Zoals verwacht is de attenuatie het sterkst in het inwendige van de kern en brengen zwaardere trefkernen grotere IFSI effecten met zich mee. Verder blijken $A(p, pN)$ reacties zich hoofdzakelijk af te spelen aan het oppervlak van de trefkern ten gevolge van het sterk attenuerend karakter van de IFSI. In dit experiment, net als in vele andere $A(p, pN)$ reacties, is het uitgestoten nucleon vrij traag. Bijgevolg is de Glauber veelvoudige-verstrooiingstheorie niet bruikbaar. De ROMEA berekeningen daarentegen geven aanleiding tot realistische IFSI factoren waarbij de verschillende parametrisaties voor de optische potentialen vergelijkbare resultaten opleveren.

Vervolgens werden de voorspellingen voor de werkzame doorsnedes vergeleken met de PNPI data. De ROMEA berekeningen reproduceren de vormen van de gemeten differentiële werkzame doorsnedes vrij goed. Verder illustreert een vergelij-

king met de vlakke-golfresultaten het tweevoudig effect van de IFSI. De IFSI zorgen niet alleen voor een attenuatie van de vlakke-golf werkzame doorsnede, maar veroorzaken ook een shift in de impulsdistributie.

De ROMEA code werd ook gebruikt om werkzame doorsnedes te berekenen voor de kinematieken van andere experimenten: ^{40}Ca$(p, 2p)$ verstrooiing bij een kinetische energie van 460 MeV voor het invallend proton, ^{16}O$(p, 2p)$ en (p, pn) verstrooiing bij 505 en 200 MeV, en ^{4}He$(p, 2p)$ verstrooiing bij 250 MeV. Onze ROMEA resultaten geven een goede beschrijving van de data voor de verschillende kinematieken, waarmee aangetoond wordt dat ons model in een ruim energiegebied toepasbaar is.

4 Nucleaire transparantie in $A(p, 2p)$ reacties

De RMSGA aanpak, die ongepast bleek voor de beschrijving van de experimentele werkzame doorsnedes bij lagere energieën, werd wel gebruikt om de IFSI in rekening te brengen bij de studie van de $A(p, 2p)$ nucleaire transparantie in het GeV-energiegebied. De nucleaire transparantie is een maat voor de waarschijnlijkheid dat de inkomende en uitgaande protonen doorheen de kern propageren zonder met de toeschouwernucleonen te interageren en is zeer geschikt in de zoektocht naar kleurtransparantie. Dit fenomeen zorgt voor een anomaal grote transmissiewaarschijnlijkheid van de protonen doorheen het nucleaire medium doordat de protonen naar een klein kleurloos object fluctueren. Voor de implementatie van kleurtransparantie in onze code werden twee modellen gebruikt: het kwantum-diffusiemodel van Farrar e.a. en het hadronische expansiemodel van Jennings en Miller. Kleurtransparantie leidt tot een nucleaire transparantie die stijgt met toenemende energie van het inkomend proton.

De nucleaire-transparantiedata vertonen echter een oscillerende energie-afhankelijkheid. Om dit te verklaren werd het Ralston-Pire model voor de pp verstrooiingsamplitude gebruikt. Volgens dit model bestaat de vrije pp verstrooiingsamplitude uit een quark-counting component die een klein object voorstelt en een Landshoff component van normale grootte. De interferentie tussen deze twee componenten verklaart de oscillaties in de vrije pp werkzame doorsnede. In het nucleaire medium wordt de Landshoff term geabsorbeerd via het standaard Glaubermechanisme, terwijl de quark-counting term relatief weinig geattenueerd wordt door

het fenomeen van kleurtransparantie. Dit zogenaamde nucleaire-filteringconcept werd in ons $A(p, 2p)$ model ingebouwd.

Voor zover ons bekend zijn de gedetailleerde RMSGA berekeningen van de $A(p, 2p)$ nucleaire transparantie de eerste van hun soort. De RMSGA procedure vereist de numerieke evaluatie van een ingewikkelde multidimensionale integraal die het effect van de botsingen van de inkomende en uitgaande protonen met alle toeschouwernucleonen bepaalt. Hierbij treedt elk toeschouwernucleon op als verstrooiingscentrum en wordt het voorgesteld door de corresponderende relativistische gebonden-toestand golffunctie. Om de benodigde computertijd te verminderen werden enkele bijkomende benaderingen ingevoerd. Zo werden de individuele golffuncties van de toeschouwernucleonen vervangen door de gemiddelde proton- of neutrondichtheid van de restkern. De nucleaire transparanties berekend met de volledige en de benaderde RMSGA methode zijn bijna identiek. Bijgevolg vormt de benaderde RMSGA aanpak een volwaardig alternatief voor het computationeel langdradige, volledige RMSGA model; althans voor de berekening van geïntegreerde grootheden zoals de nucleaire transparantie.

Onze berekeningen reproduceren de energie-afhankelijkheid van de nucleaire-transparantiedata kwalitatief dankzij de introductie van het concept van nucleaire filtering. De belangrijkste conclusie van onze studie van de $A(p, 2p)$ nucleaire transparantie is dat kleurtransparantie onontbeerlijk is om onze theoretische voorspellingen te verhogen tot de waardes geobserveerd in de experimenten. De kwantitatieve overeenkomst met de data kan echter nog veel verbeterd worden. Het onderzoek naar de $A(p, 2p)$ nucleaire transparantie blijft dan ook brandend actueel.

5 Tweede-orde eikonale correcties in $A(e, e'p)$ reacties

Ten slotte hebben we de geldigheid van de eikonale benadering bij lagere energieën onderzocht. Hiertoe hebben we een uitbreiding van het ROMEA model ontwikkeld (SOROMEA genaamd) die tweede-orde eikonale correcties in rekening brengt. De ROMEA verstrooiingsgolffunctie is immers slechts geldig tot eerste orde in $1/k$, met k de impuls van het deeltje, en is dus vooral geschikt voor hoge-energieverstrooiing.

Bij dit onderzoek naar de tweede-orde eikonale correcties hebben we ons beperkt

tot $A(e,e'p)$ observabelen. De berekeningen van de $A(e,e'p)$ nucleaire transparantie bevestigen de verwachte energie-afhankelijkheid van de tweede-orde eikonale correcties: het effect neemt toe met dalende vier-impulstransfer Q^2. De impact van de tweede-orde eikonale correcties op de $A(e,e'p)$ nucleaire transparantie is evenwel zeer beperkt, zelfs bij $Q^2 \approx 0.2$ (GeV/c)^2. Vervolgens hebben we de "missing momentum" afhankelijkheid van enkele echt exclusieve $A(e,e'p)$ observabelen, zoals de geïnduceerde normale polarisatie P_n, de links-rechts asymmetrie A_{LT} en de differentiële werkzame doorsnede, onderzocht. Deze grootheden zijn naar verwachting gevoeliger voor details in de berekeningen. Bij lage waarden van het "missing momentum" is het verschil tussen de ROMEA en SOROMEA voorspellingen verwaarloosbaar klein. In het gebied van hoge "missing momentum" zijn de tweede-orde eikonale correcties echter significant en loopt het effect op tot 30%. Hierdoor bekomen we een betere overeenkomst met de data en/of de relativistische DWIA berekeningen van de Madrid-Sevilla groep.

Onze numerieke berekeningen tonen aan dat het effect van de tweede-orde eikonale correcties op $A(e,e'p)$ grootheden over het algemeen vrij beperkt is voor $Q^2 \geq 0.2$ (GeV/c)^2. Daarenboven leidt een verandering in de keuze voor de optische potentiaal, de stroomoperator of de gebonden-toestand golffuncties tot vergelijkbare effecten.

6 Besluit

We hebben een eikonaal formalisme ontwikkeld voor de modellering van de IFSI in $A(p,pN)$ reacties. Bij lage energieën is het ROMEA model, dat de IFSI effecten implementeert door middel van nucleon-kern optische potentialen, aan te raden; terwijl bij kinetische energieën hoger dan 1 GeV het RMSGA formalisme de beste keuze is. Het ROMEA model leverde voortreffelijk werk in het reproduceren van de experimentele differentiële werkzame doorsnedes bij verschillende kinematieken, terwijl het RMSGA formalisme gebruikt werd om de $A(p,2p)$ nucleaire transparantie te bestuderen.

Om spineffecten te kunnen includeren dient een $A(p,pN)$ formalisme ontwikkeld te worden dat gefactoriseerd is op amplitudeniveau. Behalve spineffecten kan eveneens het effect van de tweede-orde eikonale correcties op $A(p,pN)$ observabelen in de toekomst nader bekeken worden. Ten slotte verdient ook de $A(p,2p)$

nucleaire transparantie bijkomend onderzoek.